Springer Theses
Recognizing Outstanding Ph.D. Research

Jiahang Shao

Investigations on rf Breakdown Phenomenon in High Gradient Accelerating Structures

Springer

Springer Theses

Recognizing Outstanding Ph.D. Research

Aims and Scope

The series “Springer Theses” brings together a selection of the very best Ph.D. theses from around the world and across the physical sciences. Nominated and endorsed by two recognized specialists, each published volume has been selected for its scientific excellence and the high impact of its contents for the pertinent field of research. For greater accessibility to non-specialists, the published versions include an extended introduction, as well as a foreword by the student’s supervisor explaining the special relevance of the work for the field. As a whole, the series will provide a valuable resource both for newcomers to the research fields described, and for other scientists seeking detailed background information on special questions. Finally, it provides an accredited documentation of the valuable contributions made by today’s younger generation of scientists.

Theses are accepted into the series by invited nomination only and must fulfill all of the following criteria

- They must be written in good English.
- The topic should fall within the confines of Chemistry, Physics, Earth Sciences, Engineering and related interdisciplinary fields such as Materials, Nanoscience, Chemical Engineering, Complex Systems and Biophysics.
- The work reported in the thesis must represent a significant scientific advance.
- If the thesis includes previously published material, permission to reproduce this must be gained from the respective copyright holder.
- They must have been examined and passed during the 12 months prior to nomination.
- Each thesis should include a foreword by the supervisor outlining the significance of its content.
- The theses should have a clearly defined structure including an introduction accessible to scientists not expert in that particular field.

More information about this series at http://www.springer.com/series/8790

Jiahang Shao

Investigations on rf Breakdown Phenomenon in High Gradient Accelerating Structures

Doctoral Thesis accepted by
the Tsinghua University, Beijing, China

Springer

Author
Dr. Jiahang Shao
Department of Engineering Physics
Tsinghua University
Beijing
China

Supervisor
Prof. Huaibi Chen
Department of Engineering Physics
Tsinghua University
Beijing
China

ISSN 2190-5053 ISSN 2190-5061 (electronic)
Springer Theses
ISBN 978-981-10-7925-2 ISBN 978-981-10-7926-9 (eBook)
https://doi.org/10.1007/978-981-10-7926-9

Library of Congress Control Number: 2017963014

© Springer Nature Singapore Pte Ltd. 2018
This work is subject to copyright. All rights are reserved by the Publisher, whether the whole or part of the material is concerned, specifically the rights of translation, reprinting, reuse of illustrations, recitation, broadcasting, reproduction on microfilms or in any other physical way, and transmission or information storage and retrieval, electronic adaptation, computer software, or by similar or dissimilar methodology now known or hereafter developed.
The use of general descriptive names, registered names, trademarks, service marks, etc. in this publication does not imply, even in the absence of a specific statement, that such names are exempt from the relevant protective laws and regulations and therefore free for general use.
The publisher, the authors and the editors are safe to assume that the advice and information in this book are believed to be true and accurate at the date of publication. Neither the publisher nor the authors or the editors give a warranty, express or implied, with respect to the material contained herein or for any errors or omissions that may have been made. The publisher remains neutral with regard to jurisdictional claims in published maps and institutional affiliations.

Printed on acid-free paper

This Springer imprint is published by Springer Nature
The registered company is Springer Nature Singapore Pte Ltd.
The registered company address is: 152 Beach Road, #21-01/04 Gateway East, Singapore 189721, Singapore

To my loving parents
and my beautiful wife

Supervisor's Foreword

The rf breakdown phenomenon is one of the main limitations to achieve high gradient accelerating structure, a key component for various applications. Although it has been studied over decades, the nature of rf breakdown has not been well understood, which is mainly caused by the uncertainty of its occurrence in terms of location and moment. In this thesis, Dr. Jiahang Shao has introduced novel methods to controllably study rf breakdown and its precursor, field emission, with high-intensity laser, pin-shaped cathodes, and a high-resolution in-situ imaging system. The experimental research leads to exciting discoveries of rf breakdown and field emission in high gradient accelerating structures, such as the evolution of power flow between cavities after breakdown, the dependence of field emission on stored energy, the discrete distribution of field emitters on surface, the overlapping of most strong emission areas and rf breakdown spots. The work greatly expands the understanding of rf breakdown and field emission, which will in turn benefit research into particle accelerators, electron sources, and high gradient rf devices in general.

Beijing, China
April 2017

Prof. Huaibi Chen

Preface

Recently, there is a pressing need for high gradient accelerating structures in compact electron-positron colliders, X-ray-free electron lasers, and compact medical/industrial accelerators. Radio-frequency (rf) breakdown phenomenon is one of the main limitations to achieve high gradient structures, which often leads to problems including surface damage, cavity detuning, incorrect phase shift, low energy gain, and beam loss, etc.

The rf breakdown is an extremely complicated physical phenomenon. It is usually believed to be triggered by field emission, followed by plasma formation, explosive emission, surface melting, and eventually avalanche. The rf breakdown rate is determined by various physical parameters including electric field, magnetic field, pulse length, and modified Poynting vector, etc. As both the location and the moment of rf breakdown occurrence are random, the conventional method to study rf breakdown is to test an accelerating structure for a long period in order to perform statistical research. However, thorough understanding of rf breakdown is limited by the extremely long experiment period and difficulties to separate the physical parameters. To more controllably investigate the rf breakdown phenomenon in high gradient accelerating structures, the thesis has proposed and applied several novel methods, including controlling the location with high-intensity laser and pin-shaped cathode, and locating field emitters with in-situ high-resolution imaging.

High-intensity laser has been adopted to trigger rf breakdown in an S-band 1.6-cell photocathode rf gun, which occurs at controllable location and moment with high rf breakdown rate. The time evolution of electron emission at the nanosecond scale after the onset of breakdown has been observed and analyzed. Two types of rf breakdown, named single-breakdown and multiple-breakdown, have been observed experimentally. In-depth analysis with an equivalent circuit model reveals that multiple-breakdown can be triggered by the power flow between cells after the initial explosive electron emission, which implies standing-wave structures with separated cells may be more favorable for high gradient accelerators.

Pin cathodes have been applied for the field emission and rf breakdown study in an L-band high gradient single-cell photocathode rf gun. Pin-shaped cathodes could significantly increase the electric field on the tip so as to control the field emission and rf breakdown location. During rf conditioning, the macroscopic electric field on the cathode has achieved 700 MV/m. The evolution of emission parameters has been monitored, which suggests that there is a threshold of electric field on the copper cathode before rf breakdown. By adjusting the longitudinal cathode position, the stored energy in the gun can be varied while maintaining the same electric field on the tip. A strong correlation between field emission current and stored energy has been observed in the high power test. Mechanisms such as capture ratio dependence, background emission, secondary electron yield, beam loading effect, space charge effect have been ruled out. The experiment results support the hypothesis of HOMs excitation by emission current and imply that under certain circumstances, a localized field emission may be significantly altered by the global parameters in a system.

In addition, the in-situ high-resolution field emission imaging has been developed in the same L-band photocathode rf gun. A novel method to achieve high-resolution imaging has been proposed by using solenoids and collimator to select electrons emitted from certain phases. Approximately 100 μm has been successfully obtained in the experiment, and separated strong field emission areas have been observed. The field enhancement factor of each individual emission area has been measured, and the variation among the surface is remarkably trivial comparing to field emission current. The results have been analyzed with a new model of emitter distribution which indicates strong field emission observed in the experiment is a result of large emission area rather than high field enhancement factor. By comparing the field emission map and the rf breakdown locations, $\sim 75\%$ of the strong field emission areas are revealed to overlap with rf breakdown spots.

These works greatly expand the existing understanding of rf breakdown and field emission, which would in turn benefit research into electron sources, particle accelerators, and high gradient rf devices in general.

Lemont, USA
May 2017

Dr. Jiahang Shao
Argonne National Laboratory

Acknowledgements

The last five years as a Ph.D. candidate is a great experience that I will always remember. I appreciate everyone who has helped me both in work and life.

First, I owe my deepest gratitude to my supervisor at Tsinghua University, Prof. Huaibi Chen. He guided me from electronic engineering into a brand new territory, particle accelerator, especially high gradient accelerating structures. He has supported me not only by providing research suggestions and supervision, but also by encouraging me to always aim higher both in my academic career and in private life. During my study of the complicated and intriguing rf breakdown and field emission phenomenon, he always had my back and helped me to overcome difficulties.

I would like to express my sincere appreciation to my supervisor at Argonne National Laboratory, Prof. Wei Gai. He has so many brilliant ideas toward the physics underlying rf breakdown. The unique setup introduced in my thesis, the in-situ high-resolution field emission imaging system, was built based on his innovation. He has also offered me the opportunity to continue my research as a postdoctoral appointee at Argonne Wakefield Accelerator facility.

I am deeply grateful to Dr. Faya Wang at SLAC National Accelerator Laboratory, who has funded me during my two-year visit at Argonne. He invented the method to control the location of rf breakdown as well as field emission with pin-shaped cathodes. He also provided a great number of valuable suggestions toward my thesis work. Through frequent talks and discussions, I have learned a great deal from him.

I would like to thank my teachers in the Department of Engineering Physics at Tsinghua University, including Prof. Dechun Tong, Prof. Chuanxiang Tang, Prof. Wenhui Huang, Prof. Shuxin Zheng, Prof. Jiaru Shi, Prof. Yingchao Du, and Prof. Lixin Yan for their inspiring courses on accelerator physics and selfless help during the laser-trigger rf breakdown experiment. I am grateful to Prof. Jiaru Shi especially for the discussion over high gradient accelerating structures and his advice on my preparation for conference talks.

I would like to thank my colleagues at Argonne and Euclid, including Dr. Conde Manoel, Dr. John Power, Dr. Chunguang Jing, Dr. Wanming Liu, Dr. Eric Wisniewski, Dr. Sergey Antipov, Dr. Sergey Baryshev, Dr. Gwanghui Ha, Charles Whiteford, and Scott Doran for their assistance in building up the beam line and helping me during my two-year visit at AWA. I owe my especial gratitude to Dr. Chunguang Jing for participating in all the high power tests and carefully revising my papers, and Dr. Sergey Baryshev for his advanced surface analysis. I really enjoy my time at AWA.

I also want to thank Dr. Zenghai Li and Dr. Liling Xiao at SLAC for the Omega3P electromagnet simulation, and Dr. Juwen Wang at SLAC for discussion over accelerating structures. I would also like to thank Dr. Klaus Flöttmann at DESY for the ASTRA dynamics simulation.

I am grateful to my dear classmates, Dr. Jiaqi Qiu, Dr. Hao Zha, Dr. Houjun Qian, Dr. Haisheng Xu, Dr. Chen Li, Dr. Yawei Yang, Dr. Dan Wang, Dr. Jin Yang, Dr. Zhe Zhang, Dr. Zhen Zhang, Cunkui Gong, Qiang Gao, Xiaowei Wu, Ping Wang, at Tsinghua for their help with my thesis, not to mention the laughters and joy they have brought into my life. My years as a Ph.D. candidate at the Accelerator Laboratory of Tsinghua University are very unforgettable and rewarding.

I would like to express my appreciation to the machining shop of the Accelerator Laboratory of Tsinghua University for providing the flat and the new shaped cathode, and SLAC machining shop for providing the pins.

I would like to appreciate the fundings supporting the researches of my thesis, including National Natural Science Foundation of China under Grant No. 11135004, U.S. Department of Energy Early Career Research Program under Contract Code LAB 11-572, and U.S. Department of Energy Office of Science under Contract No. DE-AC02-06CH11357.

At last, I would like to express my deepest love and appreciation for my family. My parents are my mentors and my friends. They have always supported me in my life regardless of all the possible twists and turns and encouraged me to pursue my dream with no restriction or hesitation. My wonderful wife has brought me so much happiness since the very first day that we met. She also spent a lot of time helping me revise this thesis. It is lovely to see her sitting in front of her desk, trying to make sense of all the bewildering physics methodology. I love them!

Contents

Chapter 1
Introduction

Abstract Particle accelerator, in which charged particles are propelled by electromagnetic field, is a powerful tool for fundamental and applied researches in various subjects. Since its birth nearly one century ago, multiple types of accelerators with different principles have been successfully developed and over 30,000 units are now in operation worldwide. For electron accelerators, the most common type applies the radio-frequency linear accelerating structure. The accelerating gradient, defined as the energy gain of particles traveling per unit length, is an essential parameter to determine the performance of an rf linear accelerating structure. Driven by the recent requirement of next generation electron-positron collider with a collision energy of TeV scale, extensive researches are being conducted to push the accelerating gradient over 100 MV/m, nearly threefold higher than that obtained with state-of-art technology. Such high accelerating gradient will also benefit other applications including free electron lasers (FEL), photocathode rf guns, and industrial/medical accelerators. However, its realization is mainly limited by rf breakdown, an extremely complicated phenomenon which includes various coupled physical procedures. rf breakdown is generally considered to be triggered by field emission from surface exposed to high electric field. This chapter introduces the application of high gradient rf linear accelerating structure, the rf breakdown phenomenon, and field emission.

1.1 Application of High Gradient Accelerating Structures

Increasing the accelerating gradient can effectively reduce the length of accelerator structures and increase beam energy in limited space. Thus, high gradient accelerating structures are highly desired in board applications from high energy machines such as TeV electron-positron collider and compact X-ray FEL, to medium energy facilities for scientific R&D, and to low energy accelerators for industrial and medical purposes.

J. Shao, *Investigations on rf Breakdown Phenomenon in High Gradient Accelerating Structures*, Springer Theses, https://doi.org/10.1007/978-981-10-7926-9_1

1.1.1 Compact Electron-Positron Collider

Research on particle interactions at the TeV scale is considered to hold the answers to many of the key open questions in particle physics, which include the mechanism of electroweak symmetry breaking, the verification of new symmetries, the understanding of Dark Matter, the searches for a wealth of other possible phenomena beyond the Standard Model [1, 2]. As a necessary complement of the current circular collider, the Large Hadron Collider (LHC), the next generation collider is proposed to be a linear type with electron-position collision to improve the accuracy [3]. There are two candidates under study worldwide, the International Linear Collider (ILC) [2] and the Compact Linear Collider (CLIC) [1].

The two projects differ from each other significantly in many aspects. For the ILC project, the main accelerator section will apply L-band 1.3 GHz superconducting technology with an average accelerating gradient of 32 MV/m [2]. Meanwhile, X-band 11.994 GHz normal conducting technology is the key for the main acceleration section of the CLIC project [1]. The nominal accelerating gradient is 100 MV/m so that particles can obtain a 3 TeV collision energy within 48 km acceleration. The CLIC project adopts the Two-Beam Acceleration (TBA) scheme, as illustrated in Fig. 1.1. The high current drive beam will be accelerated to 2.38 GeV by L-band accelerators. Then, the beam power will be extracted by X-band decelerator and transfer to X-band accelerator section to accelerate the main beam.

Figure 1.2 shows the baseline design of the X-band high gradient accelerating structure for the CLIC project. The traveling-wave structure operates in TM_{010} $2\pi/3$ mode. Each unit is about 250 mm long, with 26 regular cells and two compact couplers [4]. Higher order modes excited by the beam are damped by absorber installed

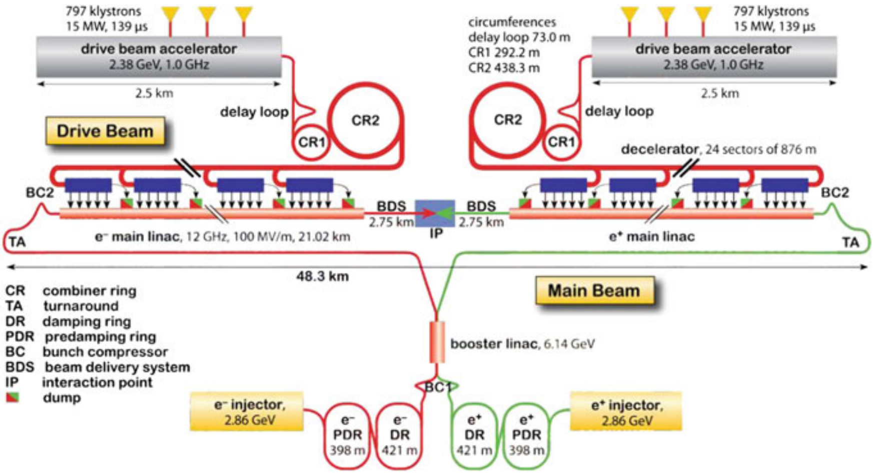

Fig. 1.1 Schematic of the CLIC project at the European Organization for Nuclear Research (CERN) [2]

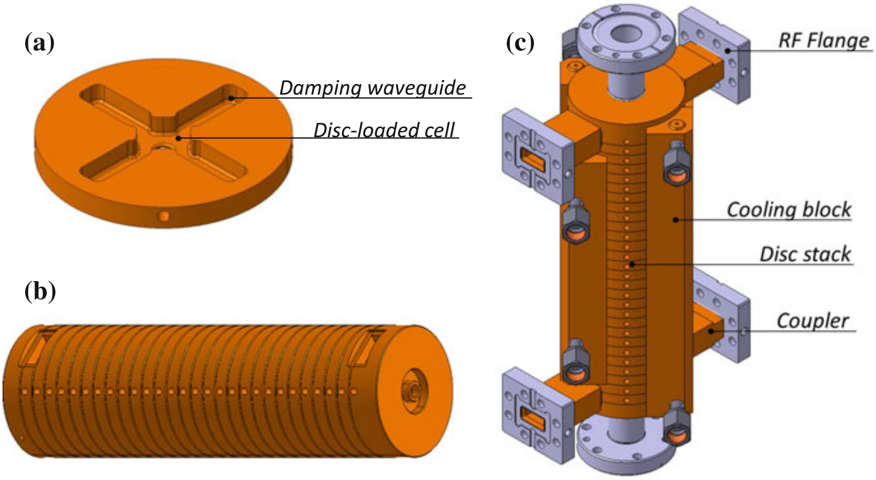

Fig. 1.2 CLIC-G waveguide damping structure [11]. **a** Disc-loaded accelerating cell with damping waveguides; **b** Cell stack for bonding; **c** Fully assembly

inside the four waveguides around the cell to minimize their interaction with following bunchlets [5]. Other alternative designs, including chock-mode damping [6, 7], detuned damping [8], iris slot structure [9], and two-halves structure [10], are also being studied.

1.1.2 *Compact Light Source*

Accelerator-based light sources are powerful tools in scientific research for various subjects, including life and biology science, material science, information science, environment science, etc. [12]. The latest generation of light source is the Free Electron Laser (FEL), which can provide light with high coherence, high brightness and continuously variable wavelength [13]. Recently, there is an increasing demand of X-ray FELs which can generate light with 0.01–10 nm wavelength and detect matter interaction at femtosecond scale. The main parameters of X-ray FEL facilities using normal conducting accelerating technology are listed in Table 1.1.

The first X-ray FEL ever built is the Linac Coherent Light Source (LCLS) at SLAC National Accelerator Laboratory. It is based on the existing SLAC 3 km S-band accelerator. The gradient is only 15 MV/m and the main acceleration section is 2 km long [14]. To achieve compact structure and low cost, later newly-built X-ray FELs broadly adopt S-band or C-band technology with accelerating gradient of 25–45 MV/m [13, 15–21]. For example, the SPring-8 Angstrom Compact free electron LAser (SACLA) project in Japan uses C-band accelerators with 30 MV/m gradient to limit the main acceleration section to 300 m. Together with in-vacuum compact

Table 1.1 Parameters of X-ray FELs with normal conducting acceleration technology

Name	Country	Energy (GeV)	Wavelength (nm)	Band[a]	Gradient (MV/m)	Status[b]
LCLS [14]	America	15	0.12	S	15	O
FERMI@ELETTRA [13, 15]	Italy	1.2	10	S	25	O
SACLA [16, 17]	Japan	8.5	0.06	C	35	O
SwissFEL [18]	Switzerland	5.8	0.1	C	26	C
SXFEL [19, 20]	China	0.84	8.8	C	40	C
PAL-FEL [21]	Korea	10	0.1	S	27	C
CLIC-FEL [22]	Switzerland	6	0.1	X	65	D
Xband-FEL [23, 24]	America	6–7	0.15	X	70	D
ZFEL [25]	Netherlands	2.1	0.8	X	100	D

[a] S-band: 2856 MHz, 2998 MHz; C-band: 5712 MHz; X-band: 11,424 MHz, 11,992 MHz
[b] *O* In operation; *C* Under construction; *D* Under design

undulators, 0.06 nm laser wavelength has been successfully generated with 8.5 GeV electron energy. The total length of the whole facility is only 700 m [16, 17].

Thanks to the advanced X-band technology developed by the CLIC project and early Next Linear Collider (NLC) project [26], several X-ray FELs under design propose to apply X-band accelerating structures with gradient of 60–100 MV/m. The main acceleration section will be suppressed to only 100 m, one order of magnitude shorter than LCLS [22, 23, 25].

In addition to big machines like X-ray FELs, several small-scale light sources also show great interest in high gradient technology due to their limited space [27, 28]. For instance, in the undergoing upgrade of the Tsinghua Thomson scattering X-ray source (TTX), the original S-band accelerating structure (3 m, 15 MV/m) will be replaced by two high gradient structures (one S-band, 1.5 m, 30 MV/m; one X-band, 1.2 m, 75 MV/m) to obtain higher beam energy and lower X-ray wavelength [28].

1.1.3 Photocathode rf Gun

The electron beam quality in FEL facility is mainly determined by initial acceleration in injector section, especially in photocathode rf gun where electrons are emitted by photoemission effect. Space charge effect from the high charge density near the cathode will decrease the following photoemission current and degrade the transverse emittance, both leading to reduction of the FEL brightness. To suppress space charge effect by relativistic effect, electrons need to be accelerated rapidly after photoemission which requires high gradient [29, 30].

Driven by the next generation FELs that can fit into current laboratories and compact gamma-ray Compton sources, high gradient X-band photocathode rf guns

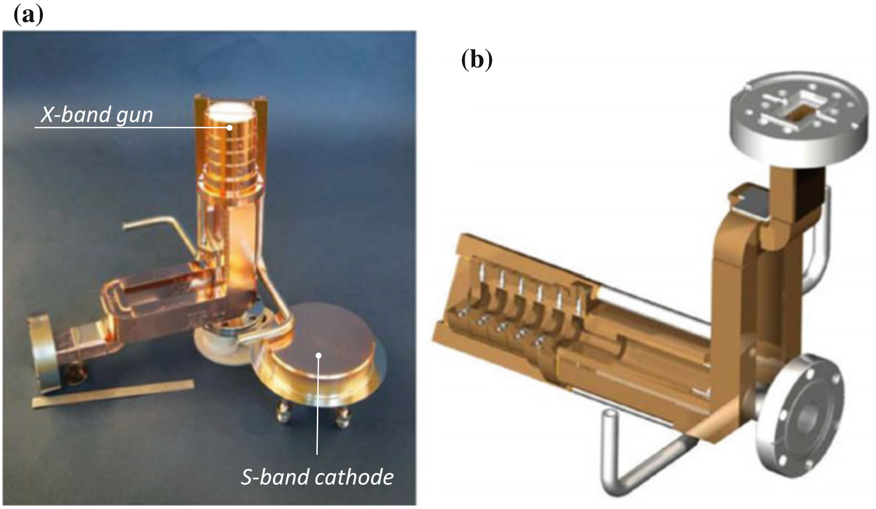

Fig. 1.3 Mark-1 type 5.6-cell X-band photocathode rf gun developed by SLAC/LLNL [30]. **a** The X-band gun, an S-band gun cathode is also displayed for dimension comparison; **b** CAD model of the gun

are under development with a peak cathode field of 200 MV/m, nearly twice of the widely-applied S-band 1.6-cell ones, as shown in Fig. 1.3. By using high gradient X-band instead of S-band photocathode rf guns, tenfold improvement of brightness is demonstrated in simulation by reducing both the bunch length by a factor of three to four and the transverse emittance by a factor of about two [30, 31].

1.1.4 Industry/Medical Accelerator

In addition to scientific researches, rf linear accelerators are broadly adopted in industrial and medical applications, such as isotopes production, irradiation, non-destructive inspections, sterilization, radiotherapy, etc. With more compact dimensions, the potential application of high gradient accelerating structures in these areas can be foreseen.

For instance, hadron radiotherapy is more effective than electron radiotherapy for specific cancers and over 70 facilities worldwide are now practicing the former technology [32]. Currently, most machines apply cyclotron or synchrotron to accelerate proton or carbon ions into several treatment areas. As the areas required by the machines are large (over 3000 m^2), a new hospital usually has to be built with high cost (130 to 150 million euro) which hampers the development of hadron radiotherapy [33]. To reduce the cost and footprint, a machine with single treatment area which can fit into existing hospitals has been studied by the TUrning LInac for

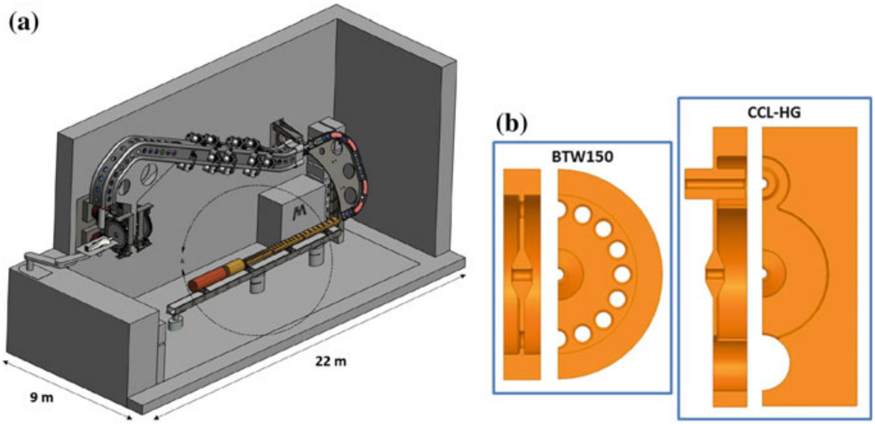

Fig. 1.4 The TULIP project [32]. **a** The layout; **b** Two candidates of the S-band high gradient accelerating structure

Proton therapy (TULIP) project in Italy [32]. This proposed machine adopts S-band accelerating structure in the main acceleration section to boost the proton energy from 70 to 230 MeV. The target gradient as high as 40 MV/m and compact design significantly reduce the footprint of the machine to only 22 m × 9 m, as shown in Fig. 1.4.

1.2 rf Breakdown

Although high gradient accelerating structures are demanded in various applications, they may not be easily achieved by simply feeding arbitrarily high rf power. The state-of-art gradient of X-band multi-cell and single-cell structures under development for the CLIC project is 120 MV/m (252 ns rf pulse length) [34] and 160 MV/m (160 ns rf pulse length) [35], respectively. These values are obtained in several prototypes with extensive effort. It's still under study whether the gradient of 100 MV/m is repeatable or not for over one hundred thousand accelerating structures requested in the CLIC project.

One of the main limitation to achieve high gradient accelerating structures is the rf breakdown phenomenon which influence both the accelerating structure and the accelerated beam. According to experimental and theoretical research, the rf breakdown rate (BDR) increases exponentially with the accelerating gradient. Therefore, reducing BDR while maintaining high gradient is a critical problem yet to be solved for the normal-conducting rf linear accelerator community. This section briefly introduces the phenomenon, the damage, and the research status of rf breakdown phenomenon.

1.2.1 Phenomenon

rf breakdown is an extremely complicated phenomenon whose mechanisms have not been fully understood over decades of research. It is generally believed that rf breakdown is triggered by strong localized field emission on the surface exposed to very high electric field [36–38]. Under certain circumstances, the local electric field at the field emitter reaches the level of 10 GV/m which leads to an emission current density of $10^{11}\,\mathrm{A/m^2}$. The resulted Joule heating could melt or even vaporize the emitter in several to tens of nanoseconds. Then the metal gas could be ionized by the emission current. The generated ions would form a sheath near the surface or hit back onto the surface which would in turn enhance the field emission and finally lead to explosive electron emission (EEE). The explosive electron emission would further modify the surface condition by melting and creating droplets as well as craters, leading to a continuous increase in emission current and eventually an avalanche. In this process, the stored energy inside the rf structure would be absorbed by the emission current until it can no longer sustain the avalanche [36]. The whole process of rf breakdown from field emission to avalanche is shown in Fig. 1.5.

When rf breakdown occurs, many abnormal phenomena could be observed experimentally, such as strong emission current from the structure, blocked transmitted rf power, high reflection, etc., as illustrated in Fig. 1.6 [36, 39]. Taking the X-band high gradient structure studied in the CLIC project for example, the breakdown current is derived to be higher than 1 kA [40]. Besides, rf breakdown is often accompanied by deterioration of vacuum, generation of light, sound, and X-ray, etc. [36, 39–42]. Such phenomena are viewed as criteria of rf breakdown to be used in the interlock system for structure protection experimentally [36, 40, 42].

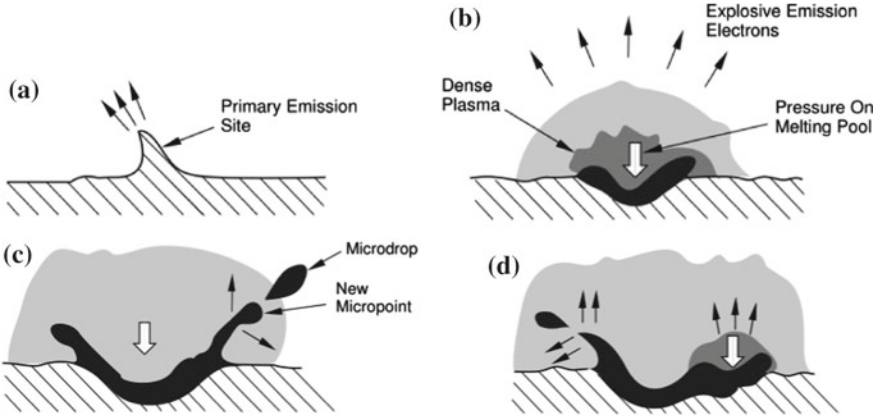

Fig. 1.5 The rf breakdown process [36]. **a** Localized field emission; **b** Field emission melts or vaporizes the emitter which forms plasma that leads to explosive electron emission; **c** Explosive electron emission results droplets and craters on the surface; **d** Avalanche in which more emitters are formed

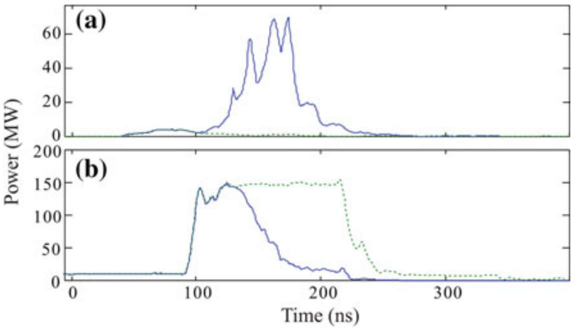

Fig. 1.6 Reflected and transmitted rf power of a traveling-wave structure [39]. The green dashed line and the blue solid line denotes the pulses without and with rf breakdown, respectively. **a** reflected power; **b** transmitted power

1.2.2 Impact

In newly-built accelerating structures, the designed gradient could not be achieved by increasing the input rf power rapidly [36, 43]. Instead, it has to go through a slow procedure called rf conditioning in which the input power and the pulse length are gradually raised. Although rf breakdown might help to remove contaminations or defects on the surface during this period, the BDR in a fully conditioned structure during normal operation must be minimized because rf breakdown is harmful to both the accelerated beam and the accelerating structure [43].

1.2.2.1 Accelerated Beam

When rf breakdown occurs, transmitted power is absorbed by the rf breakdown current which reduces the energy gain of the accelerated beam. Besides, rf breakdown current could also excite HOMs of the structure which will introduce transverse kick to the beam, resulting in deterioration of beam quality or even loss of the beam [44–46].

Recently, statistical study of the influence of rf breakdown on beam has been carried out at the CTF3 test facility of the CLIC project, as illustrated in Fig. 1.7 [46]. Caused by rf breakdown, the average loss in energy gain and the average transverse kick are measured to be ∼1 J and 0.16 mrad, respectively. If an rf breakdown occurred at the front end of the CLIC main acceleration section, the transverse kick at the interaction point would be 4 μrad which is one order of magnitude higher than the nominal value. This could severely effect the brightness of the collider [46].

1.2.2.2 Accelerating Structure

rf breakdown can lead to damage on the surface, as illustrated in Fig. 1.8 [39]. Such damage could detune the structure resonant frequency and change the phase advance between cells which is critical to synchronize with the beam. Figure 1.9 shows the

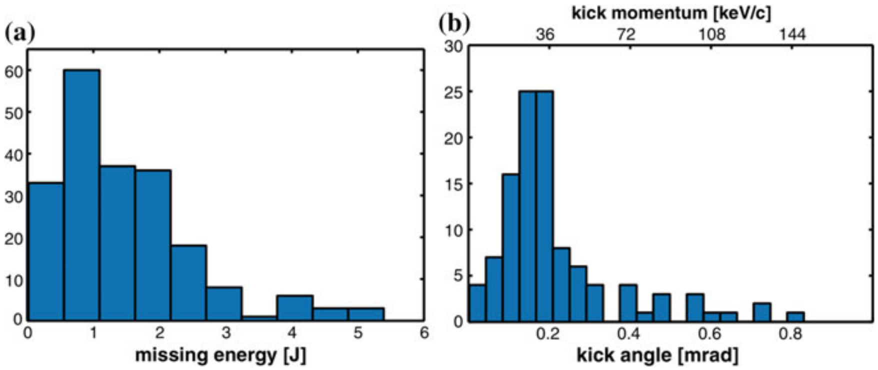

Fig. 1.7 Statistical study of the influence of rf breakdown on beam at the CTF3 test facility [46]. **a** Loss of energy gain; **b** Transverse kick

Fig. 1.8 Cross-section of the iris of an 30 GHz traveling-wave structure after several rf breakdowns [39]. The white dashed line denotes its original profile

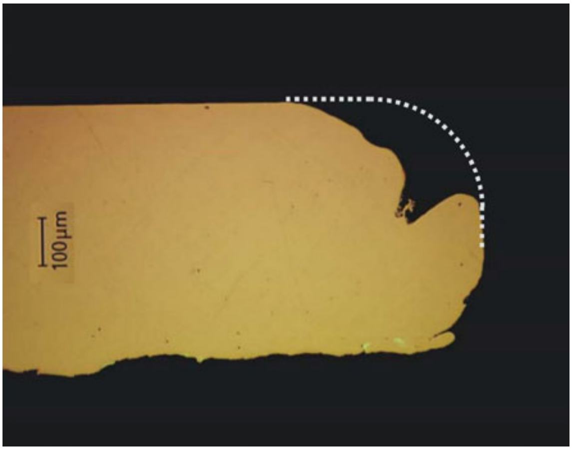

Fig. 1.9 The phase advance between cells in an X-band structure before (red) and after (blue) high power test [39]

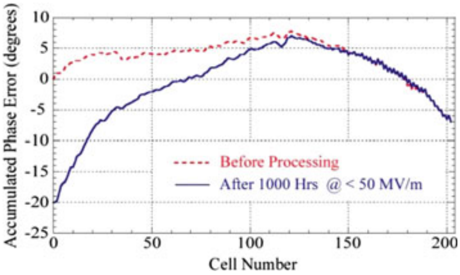

phase advance between cells in an X-band structure before and after a 1000-h high power test period. Massive rf breakdowns occurring in the first cell have changed the phase advance by ∼20° [39, 47]. These problems result in higher reflected rf power, lower accelerating efficiency, and shorter lifetime of the structure.

1.2.3 *Research Status*

Because of the influence of rf breakdown on both the accelerated beam and the accelerating structure, there are strict requirement of the rf breakdown rate in facilities with high gradient accelerating structures. In the CLIC project, the BDR in the 30 km main acceleration section is limited to 3×10^{-7} /pulse/m which corresponds to 1 % brightness loss [1]. In the SACLA FEL, the BDR is required to be lower than 2×10^{-7} /pulse/m, or one in 20 min with machine repetition of 30 Hz, to ensure the user time loss is less than 5 % [17].

Reducing the rf breakdown rate while increasing the gradient requires a thorough understanding of the rf breakdown phenomenon. Over the last few decades, both theoretical and experimental study have been intensively carried out by different research groups around the world. The researches mainly focus on the dependence of rf breakdown/BDR on physical parameters, the occurrence location of rf breakdown, and the structure behavior during rf conditioning.

1.2.3.1 rf Breakdown Dependence

A better understanding of the dependence of BDR on physical parameters could guide the optimization of high gradient structure [3, 42, 48–52]. The physical parameters which have been statistically studied include frequency, electric field, pulse heating, rf power, modified Poynting vector, etc. As rf breakdown occurs randomly both spatially within the structure and temporally within the rf pulse, long high power test period up to thousands of hours is usually required in order to accumulate sufficient data for the statistic analysis.

Operating frequency

In early studies, structures with higher frequency were believed to have higher rf breakdown threshold or lower BDR [36, 53]. However, in a recent study with exactly scaled structures operating from 21 to 39 GHz, correlation between the maximum achievable gradient and the operating frequency was not observed experimentally [54]. To date, most statistic researches focus on X-band structures operating at 11∼12 GHz.

Electric field

A lot of experiments have demonstrated the extreme sensitivity of rf breakdown rate on the accelerating gradient and the surface electric field. An empirical formula has been summarized as [55–58]

$$BDR \propto E^{30} \tag{1.1}$$

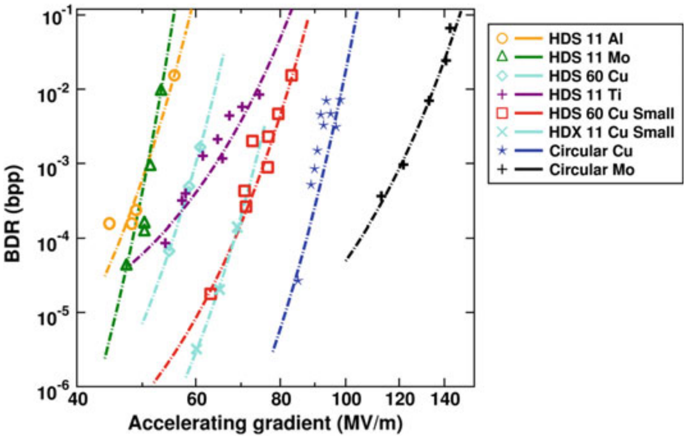

Fig. 1.10 The rf breakdown rate as a function of the accelerating gradient for various structures. The points and lines denote experimental results and the fitting based on the defect model, respectively [60]

The mechanism of such sensitive dependence is still under study and there are various hypotheses. One hypothesis attributes the phenomenon to highly unstable surface condition under extremely high electric field. Practical surface in accelerating structures has many imperfect features including defects, contaminations, particles, protrusions, grain boundaries, etc. which could significantly enhance the local electric field by a factor of 100 to 10 GV/m [36]. Such high electric field force exceeds the tensile strength of copper [39]. Besides, strong field emission under high electric field would also contribute to the instability of the surface [59]. Under this circumstance, any tiny changes in the surface field would dramatically influence the surface condition and the rf breakdown rate. Recently, a research group in the University of Helsinki has applied molecular dynamics technology into simulating the evolution of surface defects under strong electric field. Their results show reasonable agreement with the experimental observation, as illustrated in Fig. 1.10 [60].

Pulse length

In the statistic study, an empirical formula describing the dependence of BDR on pulse length has been summarized as [57, 58]

$$BDR \propto \tau^5 \tag{1.2}$$

Besides, high power test results also show massive rf breakdowns occurring on the surface of the input coupler where the magnetic field was strong [61]. Currently, it is generally accepted that the effect of pulse length and magnetic field on BDR is in the form of pulse heating, which could lead to metal fatigue and changes in local grain

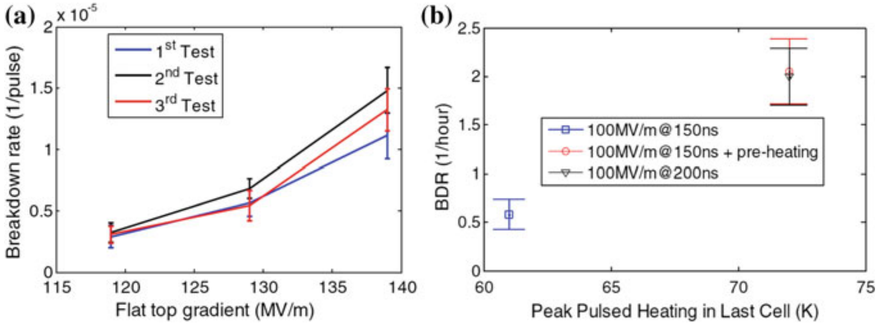

Fig. 1.11 Experiment results using pre-pulse to heat the accelerating structure [63]. **a** BDR as a function of the accelerating gradient with the same pulse heating; **b** BDR as a function of pulse heating

boundary [61, 62]. Pulse heating is defined as the localized surface temperature rise by Joule heating from the surface current within one rf pulse and can be calculated as [3, 62]

$$\triangle T = \frac{1}{\sigma\delta} H_s^2 \sqrt{\frac{\tau}{\pi c_\varepsilon \rho k}} \tag{1.3}$$

where, σ is the conductivity, δ is the skin depth, H_s is the surface magnetic field, c_ε is the specific heat capacity, ρ is the density, k is the thermal conductivity.

Recently, researchers at SLAC used an rf compressor to generate a small pre-pulse prior to the main pulse to separately study the effect of pulse heating and electric field on the rf breakdown rate [63]. Results in Fig. 1.11a show that with the same pulse heating, there was only a fourfold difference in BDR when the gradient increased from 119 to 139 MV/m, which was remarkably lower than the factor of 105 predicted by Eq. 1.1. Results in Fig. 1.11b show that with the same pulse heating, similar BDR could be obtained even with different pulse lengths which was contrary to Eq. 1.3. This experiment strongly supports the conclusion of BDR dependence on the pulse heating.

Power and modified Poynting vector

Besides electric field and pulse heating, earlier statistic studies also showed dependence of BDR on the rf power. For example, researchers at SLAC have observed that the entrance of an accelerating structure, where the rf power was the highest, experienced more rf breakdowns than other cells [61]. Researchers at CERN have also proposed a hypothesis of BDR dependence on the rf power density normalized by the iris radius [64].

In a recent study, researchers at CERN have developed a new factor named the modified Poynting vector S_c based on a model in which rf power supports local field emission and Joule heating to melt an emitter and to trigger rf breakdown. The modified Poynting vector can be expressed as

$$S_c = \mathrm{Re}(\overline{\mathrm{S}}) + \frac{1}{6}\mathrm{Im}(\overline{\mathrm{S}}) \tag{1.4}$$

where $\overline{S} = E \times H$ is the Poynting vector, its real and imaginary part denote the active and reactive power flow inside an rf structure, respectively. The coefficient 1/6 is adjusted to best match the experimental results obtained in massive structures.

Figure 1.12 shows the achievable physical parameters for various fully rf conditioned structures. An ideal parameter to describe the rf breakdown limitation will present a horizontal line. Compared with accelerating gradient, surface electric field, and rf power or its density among structures, the variation of the modified Poynting vector is smaller which validates the model [58].

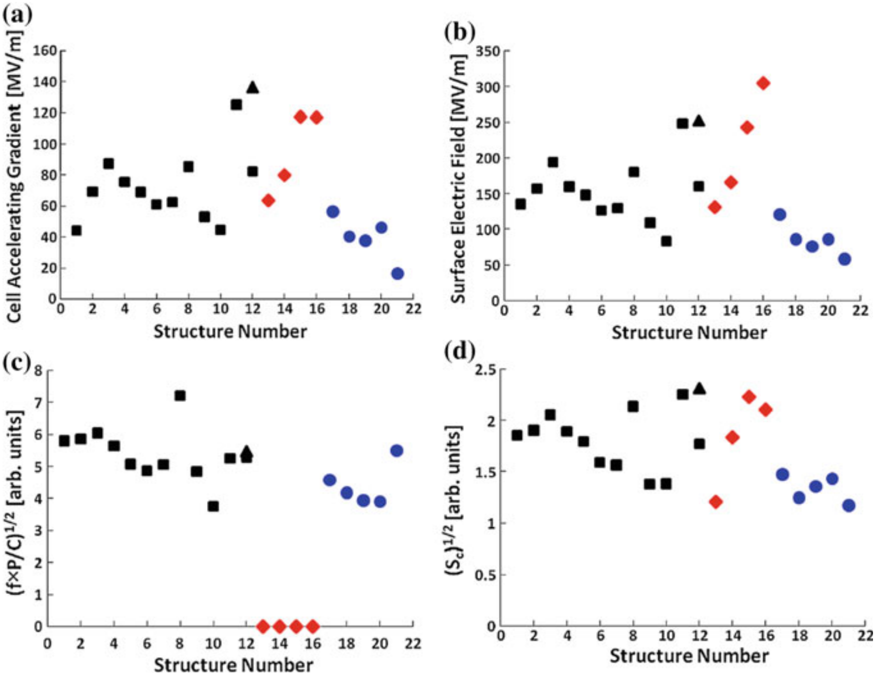

Fig. 1.12 The maximum achievable parameters in different structures [58]. The black squares, the red diamonds, and the blue circles denote X-band traveling-wave structures, X-band standing-wave structures and 30 GHz traveling-wave structures. **a** Accelerating gradient; **b** Surface electric field; **c** Root of rf power density; **d** Root of the modified Poynting vector

Future study

Although intensive researches have been performed to study the dependence of rf breakdown limitation and BDR for decades, there is not a single theory well-established to match all dependence observed in experiment and precisely predict the structure limitation [65]. The difficulty lies in the extreme complexity of rf breakdown, and the fact that many physical parameters, such as the electric field, the pulse heating, and the modified Poynting vector, are usually coupled with each other in conventional rf structures. Several novel rf structures, such as the multi-mode cavity [66, 67] and the multi-frequency cavity [68, 69], have been proposed for future test to study these parameters separately.

1.2.3.2 rf Breakdown Location

Apart from the rf breakdown dependence, several researches also focus on the location of rf breakdown, leading to the development of several in-situ methods [70–75]. In these researches, the rf breakdown location is defined as the location of the initial explosive electron emission.

Observing rf breakdown location is important for the high gradient accelerating structure study in two aspects. First, physical parameters including the electric field, the pulse heating, and the modified Poynting vector usually vary along the structure. Therefore, more precise dependence of rf breakdown or BDR on these parameters which could better guide the structure optimization can be estimated by determination of rf breakdown location. Second, the rf breakdown phenomenon is also related to localized surface condition and may be triggered by strong field emission from defects. By comparing the rf breakdown location and the ex-situ surface condition, more clear relationship between them could be established which could lead to more explicit fabrication and cleaning procedures.

Longitudinal location

In traveling-wave structures, the time delay between the rising edge of incident power and that of reflected power or falling edge of transmitted power is roughly proportional to the distance traveled by the rf pulse from the start of the structure to the location where the rf breakdown occurred, as illustrated in Fig. 1.13. Therefore, this delay can be used to locate the rf breakdown location with a resolution of one to two cells [70, 71].

In standing-wave structures, rf breakdown occurring on the iris generates plasma which would block the coupling between cells. Therefore, several longitudinal space harmonics could be excited, represented by beating pattern in the rf pickup signal. rf breakdown location with a resolution of one cell can be derived from the beating pattern, as illustrated in Fig. 1.14 [72].

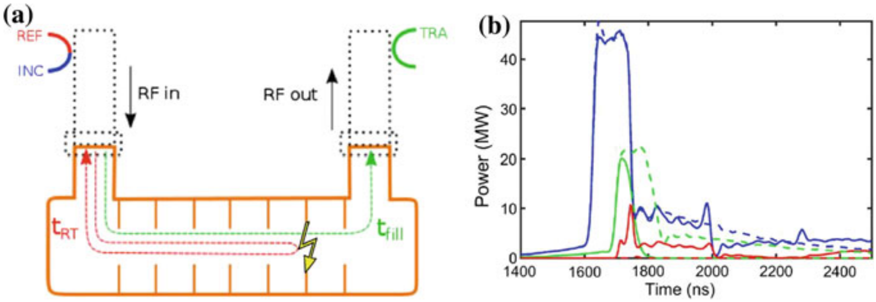

Fig. 1.13 Determination of the longitudinal rf breakdown location in traveling-wave structures by time delay between the rising edge of incident power and that of reflected power or falling edge of transmitted power [71]. **a** The model of power transmission and reflection; **b** Typical waveforms of incident power (blue), reflected power (red), and transmitted power (green) for normal operation (dashed) and rf breakdown event (solid)

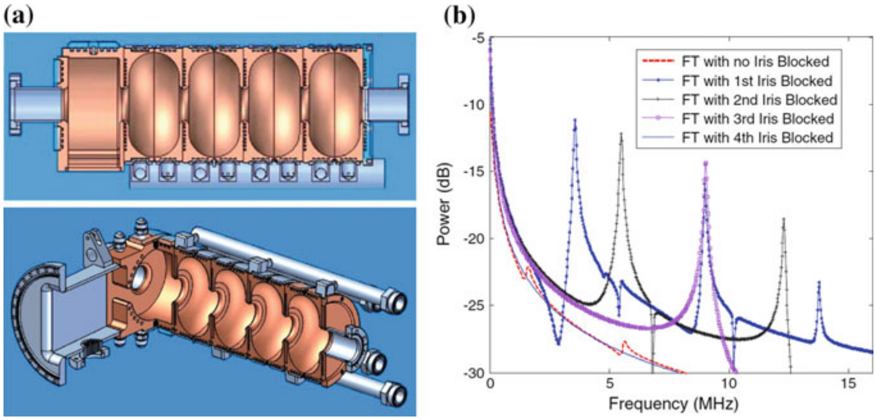

Fig. 1.14 Determination of the longitudinal rf breakdown location in standing-wave structures by beating pattern [72]. **a** The model of the structure under study; **b** Predicted spectrum of rf pickup signal with different rf breakdown location

Apart from rf signals, rf breakdown location can also be determined by acoustic sensors detecting mechanical vibration along the structure caused by rf breakdown [73, 74].

Transverse location

Compared with the longitudinal location of rf breakdown, the transverse one is more difficult to be observed. Recently in the High Energy Accelerator Research Organization of Japan (KEK), researchers have determined the transverse location by observing flash accompanying the rf breakdown, as shown in Fig. 1.15 [75]. The location resolution from the images is derived to be at the order of millimeter to centimeter.

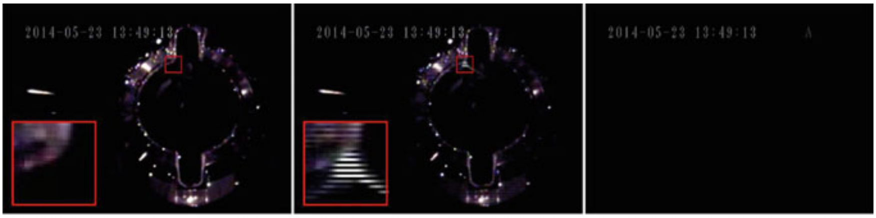

(a) 1 frame (1/30 s) before this cavity breakdown.

(b) At the moment of this cavity breakdown.

(c) 1 frame (1/30 s) after this cavity breakdown.

Fig. 1.15 Determination the rf breakdown transverse location by observing the accompanying flash [75]

Limitation

Currently, the resolution in rf breakdown location study is lower than millimeter. However, field emission and explosive electron emission are localized phenomena with dimensions smaller than micrometer, as is revealed by ex-situ surface examination with advanced tools such as Scanning Electron Microscopy (SEM) and White Light Interferometer (WLI) [36, 76]. Thus, higher resolution with novel method is to be obtained in future studies.

1.2.3.3 rf Conditioning Behavior

rf conditioning is important for accelerating structures to achieve high gradient and several most recent researches have analyzed rf breakdown behavior within this period [43, 71, 77].

Researchers from CERN have compared the conditioning history of several X-band accelerating structures for the CLIC projects and samples with dc test stand. The results show that the conditioning progresses with the number of rf pulses but not with the number of breakdowns [43]. By examining the distribution of number of pulses between breakdowns during the rf conditioning period, they have also distinguished two types of rf breakdown events, named primary breakdown and follow-up breakdown, as illustrated in Fig. 1.16. The former one may occur randomly and independently at some point on the high-field surface, and the latter one may occur as a direct result of a previous breakdown [71]. Researchers from Tsinghua University have confirmed the two types with more detailed analysis of the distribution of rf breakdown location and moment [77]. These works expand the understanding of the physical mechanism behind conditioning which may lead to a decrease in conditioning time [43].

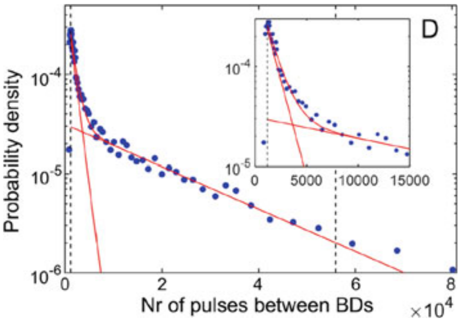

Fig. 1.16 Distribution of number of pulses between breakdowns and two-exponential fit. The fit with smaller slope on the right and the one with higher slope on the left indicate the primary breakdown and the follow-up breakdown, respectively [71]

1.3 Field Emission

In researches of rf breakdown in high gradient accelerating structures, field emission is generally viewed as the trigger of rf breakdown and has been studied intensively [36–38]. Recently, field emission has also attracted research interest among the cathode community due to its low thermal emittance, high current density, and simplicity [78–82]. This section introduces the basis of field emission and focuses on its research progress in high gradient accelerating structures.

1.3.1 Phenomenon

In metal, electrons can tunnel through the surface barrier when an external electric field is applied [36, 83–86]. In one-dimensional model of a prefect surface with no protrusions or defects, the surface barrier is modified by the external electric field as [36]

$$V(z) = \begin{cases} -W_{\mathrm{a}} & , \quad z < 0 \\ -eE_0 z - e^2/4\pi\varepsilon_0 z & , \quad z > 0 \end{cases} \tag{1.5}$$

where $-W_{\mathrm{a}}$ is the potential energy of the electron inside the metal, $-e^2/4\pi\varepsilon_0 z$ is the contribution of the image charge, e is the charge of an electron, and ε_0 is the vacuum permittivity, as illustrated in Fig. 1.17.

The dependence of field emission current on the applied external field at low temperature (T$\leq$ 300 K) can be described by the Fowler-Nordheim (F-N) equation. By solving the one-dimensional Schrodinger equation with the barrier in Eq. 1.5, the F-N equation can be derived as [36]

$$I_{\mathrm{F}} = A_{\mathrm{e}} \frac{1.54 \times 10^{-6} E_0^2}{\phi t^2(s)} \exp[-\frac{6.83 \times 10^9 \phi^{1.5} v(s)}{E_0}] \tag{1.6}$$

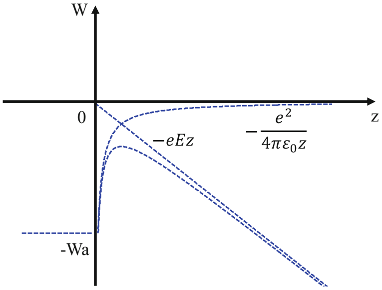

Fig. 1.17 Modified surface barrier with external electric field [36]

where I_F is the field emission current in A; E is the electric field amplitude in V/m; A_e is the effective emission area in m^2; ϕ is the work function in eV; $t(s)$ is tabulated dimensionless elliptic function, s and $v(s)$ can be expressed as [36, 84]

$$s = 3.79 \times 10^{-5} E_0^{0.5}/\phi \tag{1.7}$$

$$v(s) = 0.956 - 1.062 s^2 \tag{1.8}$$

Taking Eqs. 1.7 and 1.8 into Eq. 1.6, and with $t(s) \approx 1$, the F-N equation can be simplified as [36]

$$I_F = A_e \frac{1.54 \times 10^{-6} \times 10^{4.52\phi^{-0.5}} E_0^2}{\phi} \exp[-\frac{6.53 \times 10^9 \phi^{1.5}}{E_0}] \tag{1.9}$$

On practical surface, features like defects, contaminations, particles, protrusions, grain boundaries, etc. will enhance the local electric field. The field enhancement factor β is defined as

$$\beta = \frac{E_{\mathrm{local}}}{E_0} \tag{1.10}$$

After taking local field enhancement into consideration, Eq. 1.9 is expressed as [36]

$$I_F = A_e \frac{1.54 \times 10^{-6} \times 10^{4.52\phi^{-0.5}} (\beta E_0)^2}{\phi} \exp(-\frac{6.53 \times 10^9 \phi^{1.5}}{\beta E_0}) \tag{1.11}$$

Equations 1.6, 1.9 and 1.11 are derived for surface exposed to dc field. In rf case, the surface field varies with time as $E(t) = E_0 sin(\omega t)$ where ω is the rf frequency. By integrating Eq. 1.11, the average field emission current over one rf period $\overline{I_F}$ can be express as [36]

$$\overline{I_F} = A_e \frac{5.7 \times 10^{-12} \times 10^{4.52\phi^{-0.5}} (\beta E_0)^{2.5}}{\phi^{1.75}} \exp(-\frac{6.53 \times 10^9 \phi^{1.5}}{\beta E_0}) \tag{1.12}$$

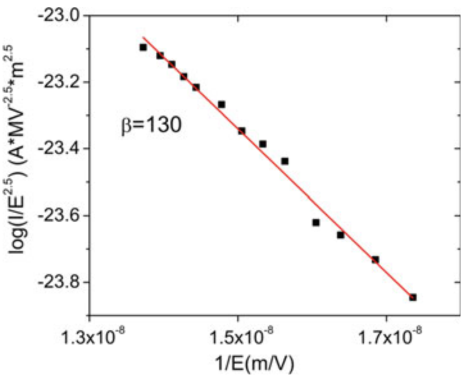

Fig. 1.18 Typical experiment results (red line) and fitting (black dots) in the F-N coordinate [87]

Equation 1.12 is the common format of the F-N equation applied in the study of high gradient accelerating structures. In high power test, the average emission current $\overline{I_{\mathrm{F}}}$ is monitored while the macroscopic electric field E_0 is being adjusted by the input rf power. By linear fitting the data in the F-N coordinate (x-axis of $1/E_0$ and y-axis of $\lg(I_F/E_0^{2.5})$), β can be derived from the slope as [36]

$$\frac{d(\lg(I_F/E_0^{2.5}))}{d(1/E_0)} = -\frac{2.84 \times 10^9 \phi^{1.5}}{\beta} \tag{1.13}$$

And A_{e} can be derived from the intercept of the y-axis afterwards. Figure 1.18 shows a typical measurement and fitting results.

1.3.2 Research Status

The researches of field emission in the high gradient accelerating structure community mainly focus on the emission parameters (β and A_{e}) measurement and their relationship with the practical surface condition. Several works also aim to locate field emitters on the surface.

1.3.2.1 Emission Parameters

When the work function ϕ is treated as a constant, the emission current under certain macroscopic electric field E_0 is determined by emission parameters β and A_{e} which are therefore considered to reflect the surface condition of accelerating structures. However, a large discrepancy exists between properties of the emission area obtained through direct observation using advanced surface analysis tools and those indirectly obtained from fitting the experimental data to the F-N equation [36, 87].

Field enhancement factor is generally believed to be caused by features like defects, contaminations, particles, protrusions, grain boundaries, etc. For a cylinder type emitter, the field enhancement factor can be approximately calculated as the ratio of its height and radius [36]. In high power test, the field enhancement factor is usually measured to be a high value from tens to hundreds [58, 87, 89, 90]. According to the enhancement model [36], such high β is likely to result from features with very high aspect ratio. However, these features are not likely to exist on surfaces fabricated by advanced machining with precision of micrometer and surface roughness of nanometer. In a research performed on an S-band photocathode rf gun at Tsinghua University, β over 30 has been measured on the cathode in the high power test even though the ex-situ surface analysis with WLI showed β of only 1.2 ± 0.2 [87].

Besides, the effective emission area is usually fitted to be a low value at the order of square nanometer which is unphysical since Joule heating by the high current density would immediately melt the emitter which means stable emission should not have been observed [87].

There are various hypothetical explanations for the contradictions. Researchers from Tsinghua University have proposed that field emission might be dominated by areas with abnormally low work function. After varying the work function, fitting the experiment data with the F-N fitting could result in more reasonable emission parameters, as illustrated in Fig. 1.19 [87]. A research group from University of Helsinki has performed molecular dynamics with a void under surface. Their results suggest dynamic evolution of surface condition under high electric field would increase the field enhancement factor in high power tests [60, 88]. Researchers from SLAC have performed theoretical and simulation study of HOMs excited by the emission current. Under some circumstances, HOMs should be considered together with the fundamental mode when calculating the applied electric field [91].

Besides, there are also studies focusing on the F-N equation itself. Researchers from U.S. Naval Research Laboratory (NRL) have studied the Joule heating

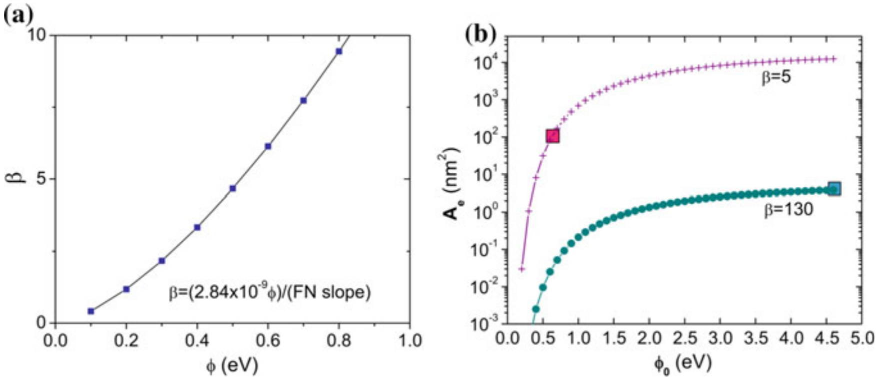

Fig. 1.19 F-N equation fitting results as a function of work function [87]. **a** Field enhancement factor β; **b** Effective emission area A_e

and Nottingham effect by the strong emission current and pointed out the conventional F-N equation should be modified correspondingly [92]. Several other groups have extended the studied of field emission from one-dimensional model to three-dimensional ones and also proposed modifications of the current F-N equation [93–96].

1.3.2.2 Emission Location

To solve the discrepancy issue as well as to answer other questions surrounding field emission, it's necessary to observe the field emitter in-situ with high resolution.

In dc studies, the common method to obtain field emitter mapping is to scan a pin-shaped anode along the cathode with a resolution better than micrometer, as illustrated in Fig. 1.20 [97–99]. Together with advanced surface analysis tools, these studies have revealed strong field emission from features like contaminations, scratches, grain boundaries, etc. on the surface [99].

However, field emission imaging with high resolution in rf case is more difficult due to the complicated dynamics of emission electrons. In high gradient accelerating structure studies, field emission is also known as the dark current referring to its unknown emitter location. So far, several groups have tried to locate field emitter

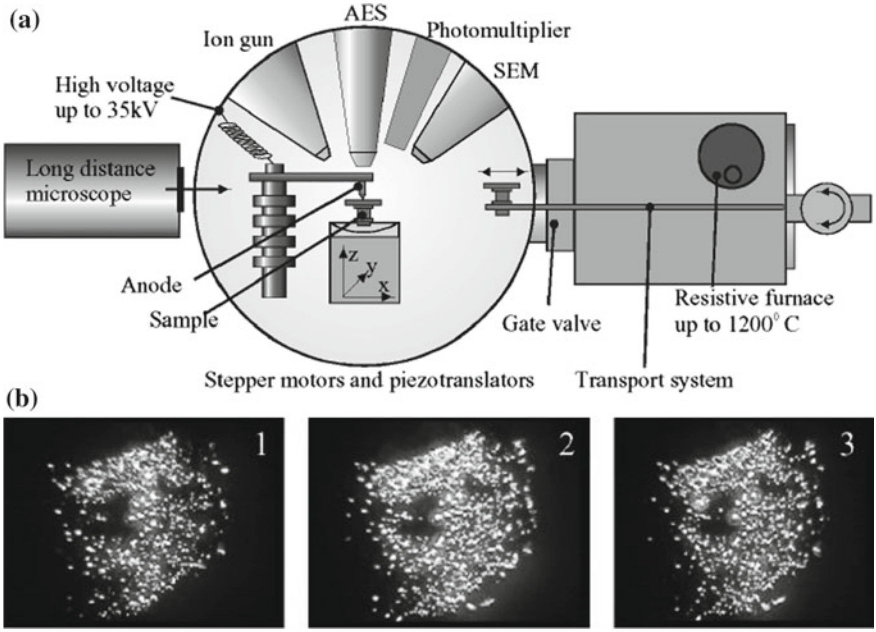

Fig. 1.20 Scheme of the field emission scanning microscope (**a**) and several field emission images of carbon nanotubes (**b**)

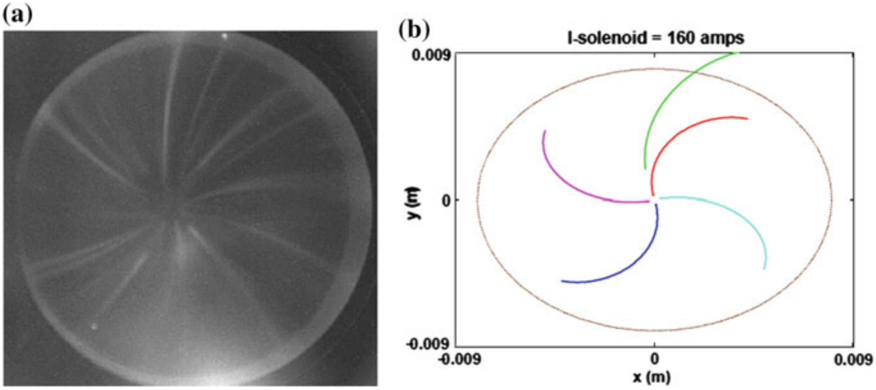

Fig. 1.21 Field emission pattern of an S-band photocathode rf gun at SLAC [101]. **a** In-situ observation; **b** Dynamics simulation of five emitters on the cathode

on the surface by comparing the field emission pattern captured downstream of the structures with dynamics simulation [100–102]. Figure 1.21 shows an example of the field emission pattern of an S-band photocathode rf gun in experiment and with simulation. It's difficult to evaluate the resolution of these methods as the images of different emitters may overlap with each other.

1.4 Main Content and Innovation

Recently, the Accelerator Laboratory of Tsinghua University has intensively participated in the high gradient accelerating structure R&D with collaborators around the world, including the development of S-band high gradient photocathode rf gun [29], the development of X-band Chock-mode damping accelerating structure [3, 6, 7], the research of the CLIC T24 prototype structure [28, 77], the study of W-band two-halves PETS/accelerating structure [103], the design of X-band pulse compressor for klystron-based CLIC [104], etc. Supported by the project 'Physics and key technology research in X-band high gradient accelerating structures' funded by National Natural Science Foundation of China, this thesis has conducted in-depth research on field emission and rf breakdown in collaboration with Dr. Faya Wang from SLAC, the Argonne Wakefield Accelerator facility (AWA) at Argonne National Laboratory (ANL), and the Euclid Techlabs LLC.

This research is driven by the difficulties to locate rf breakdown sites and field emitters in rf structures. To solve these problems, this research has proposed and applied several novel methods, including controlling the location with high intensity laser and pin-shaped cathode, and locating field emitters with in-situ high resolution imaging. The structure of this thesis is shown in Fig. 1.22.

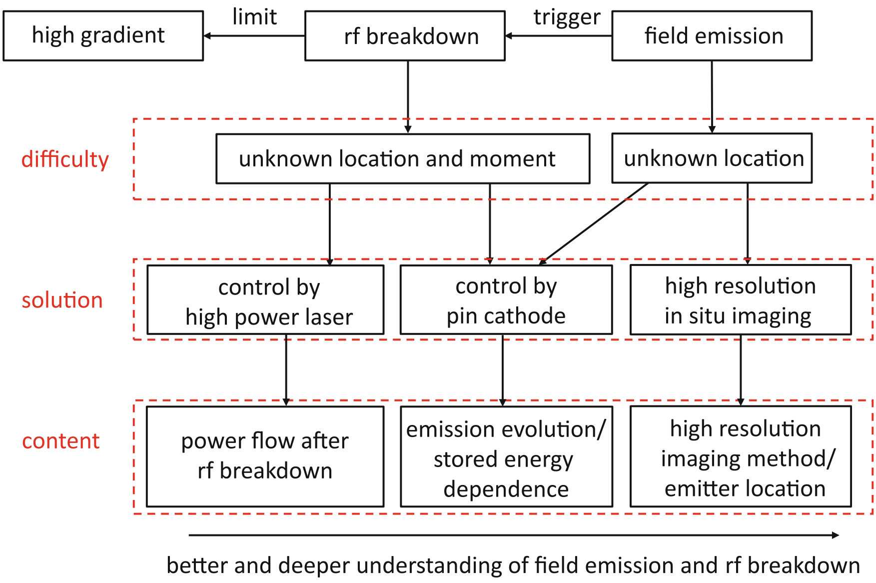

Fig. 1.22 The structure of the thesis

Chapter 2 introduces the rf breakdown study with high intensity laser in an S-band 1.6 cell photocathode rf gun at the Accelerator Laboratory of Tsinghua University. The location and moment of rf breakdown have been precisely controlled by the incident high intensity laser on the cathode. Two types of rf breakdown, named single-breakdown and multiple-breakdown, have been observed experimentally. The multiple-breakdown events, in which more than two explosive emission current pulses could be detected within one rf pulse, was dominant in spontaneous rf breakdowns without laser trigger. Meanwhile, single-breakdown dominated when the high intensity laser was introduced. An equivalent circuit model has been developed to study the evolution of power flow between the two cells after rf breakdown. The physical mechanism of multiple-breakdown has been revealed with detailed analysis using the circuit model. A new accelerating structure to limit multiple-breakdown has been proposed accordingly.

Chapter 3 presents the field emission and rf breakdown study with pin cathode in an L-band high gradient single cell photocathode rf gun at AWA. Pin cathodes from SLAC could significantly increase the electric field on the tip so as to control the field emission and rf breakdown location. During rf conditioning, the macroscopic electric field on the cathode has achieved 700 MV/m. The evolution of emission parameters has been monitored, which suggests that there is a threshold of electric field on the copper cathode before rf breakdown. By adjusting the longitudinal cathode position, the stored energy in the gun can be varied while maintaining the same electric field on the tip. A strong correlation between field emission current and stored energy has been observed in the high power test. Mechanisms such as capture ratio dependence, background emission, secondary electron yield, beam loading effect, space charge effect have been ruled out. The experiment results support the hypothesis of HOMs excitation by emission current and implies that under certain circumstances, a localized field emission may be significantly altered by the global parameters in a system.

Chapter 4 introduces the in-situ high resolution field emission imaging in the same L-band photocathode rf gun. A novel method to achieve high resolution imaging has been proposed by using solenoids and collimator to select electrons emitted from certain phases. $\sim$100 μm has been successfully obtained in the experiment and separated strong field emission areas have been observed. The field enhancement factor of each individual emission area has been measured and the variation among the surface is remarkably trivial comparing to field emission current. A new field emitter model has been established accordingly to study the mechanism. rf breakdown spots have been found on the surface in the ex-situ SEM observation. By comparing the field emission map and the SEM images, $\sim$75 % of the strong field emission areas are revealed to overlap with rf breakdown spots. This work greatly expands the existing understanding of field emission, which would in turn benefit research into electron sources, particle accelerators, and high gradient rf devices in general.

At last, Chap. 5 summarizes the researches presented in the thesis and proposes a list of work to be conducted in future study.

The innovation of the thesis includes:

1. Control the rf breakdown location and moment by high intensity laser. Reproduce and analyze the power flow after rf breakdown by an equivalent circuit model with rf breakdown current. Reveal the physical mechanism of multiple-breakdown within one rf pulse.

2. Control the field emission and rf breakdown location by pin-shaped cathode. Observe the field emission parameters evolution during rf conditioning with macroscopic electric field up to 700 MV/m. Discover the dependence of field emission current on stored energy with the same electric field.

3. Propose and preform the in-situ field emission imaging with a resolution of $\sim$100 μm. Measure field enhancement factor of individual emitters and develop a new model of field emitter distribution. Observe the overlapping of most strong field emission areas and rf breakdown spots.

References

1. CLIC conceptual design report (2012) Technical report, CERN
2. The International Linear Collider technical design report (2013) Technical report, ILC
3. Zha H (2013) Design and experiment of CLIC Choke-mode accelerating structure. Ph.D. thesis, Tsinghua University
4. Zha H, Grudiev A (2016) Design and optimization of Compact Linear Collider main linac accelerating structure. Phys Rev Accel Beams 19:111003
5. Zha H, Latina A, Grudiev A et al (2016) Beam-based measurements of long-range transverse wakefields in the Compact Linear Collider main-linac accelerating structure. Phys Rev Accel Beams 19:011001

6. Zha H, Shi J, Chen H et al (2012) Choke-mode damped structure design for the Compact Linear Collider main linac. Phys Rev ST Accel Beams 15:122003
7. Zha H, Jing C, Qiu J et al (2016) Beam-induced wakefield observation in X-band choke-mode cavities. Phys Rev Accel Beams 19:081001
8. Khan V (2011) A damped and detuned accelerating structure for the main linacs of the compact linear collider. Ph.D. thesis, The University of Manchester
9. Jones R (2009) Wakefield suppression in high gradient linacs for lepton linear colliders. Phys Rev ST Accel Beams 12:104801
10. Zha H, Grudiev A (2017) Design of the Compact Linear Collider main linac accelerating structure made from two halves. Phys Rev Accel Beams 20:042001
11. Solodko A (2017) CLIC test and prototype structure production. In: Proceedings of HG2017, Valencia, Spain
12. Fang W (2012) C-band high-gradient accelerating structure for compact X-ray free electron lasers. Ph.D. thesis, Shanghai Institute of Applied Physics, CAS
13. Allaria E, Callegari C, Cocco D et al (2010) The FERMI@Elettra free-electron-laser source for coherent x-ray physics: Photon properties, beam transport system and applications New J Phys 12:075002
14. Emma P, Akre R, Arthur J et al (2010) First lasing and operation of an ångstrom-wavelength free-electron laser. Nat Photon 4:641–647
15. Fermi@Elettra conceptual design report (2007) Technical report, Sincrotrone Trieste S.C.p.A
16. Tanaka H, Aoyagi H, Asaka T et al (2012) A compact X-ray free-electron laser emitting in the sub-ångström region. Nat Photon 6:540–544
17. Inagaki T, Kondo C, Maesaka H et al (2014) High-gradient C-band linac for a compact x-ray free-electron laser facility. Phys Rev ST Accel Beams 17:080702
18. SwissFEL conceptual design report (2010) Technical report, PSI
19. Zhao Z, Chen S, Yu L, et al (2011) Shanghai soft X-ray free electron laser test facility. In: Proceedings of IPAC2011, San Sebastián, Spain
20. Fang W, Gu Q, Tan J, et al (2016) Progress in C-band and X-band technology at SINAP. In: Proceedings of CLICWorkshop 2016, Geneva, Switzerland
21. Kang H, Kim K, Ko I (2014) Current status of PAL-XFEL project. In: Proceedings of IPAC2014, Dresden, Germany
22. Aksoy A, Yavaş Ö, Schulte D, et al (2014) Conceptual design of an X-FEL facility using CLIC X-band accelerating structure. In: Proceedings of IPAC2014, Dresden, Germany
23. Adolphsen C, Huang Z, Bane K, et al (2010) A compact X-band linac for an X-ray FEL. In: Proceedings of LINAC2010, Tsukuba, Japan
24. Sun Y, Emma P, Raubenheimer T et al (2014) X-band rf driven free electron laser driver with optics linearization. Phys Rev ST Accel Beams 17:110703
25. Beijers J, Brandenburg S, Eikemaand K et al (2010) ZFEL: A compact, soft X-ray FEL in the Netherlands. In: Proceedings of FEL2010, Malmö, Sweden
26. Zeroth-order design report for the Next Linear Collider (1996) Technical report, NLC
27. Wuensch W (2016) High-gradient acceleration: CLIC and beyond. In: Proceedings of CLIC Workshop 2016, Geneva, Switzerland
28. Shi J (2016) Development of X-band high-gradient structures at Tsinghua University. In: Proceedings of CLIC Workshop 2016, Geneva, Switzerland
29. Qian H (2012) Research on the Emittance Issues of Photocathode RF Gun. Ph.D. thesis, Tsinghua University
30. Limborg C, Adolphsen C, McCormick D et al (2016) Performance of a first generation X-band photoelectron rf gun. Phys Rev Accel Beams 19:053401
31. Limborg C, Adolphsen C, Chu S et al (2011) An X-band gun test area at SLAC. In: Proceedings of PAC2011, New York, USA
32. Benedetti S, Grudiev A, Latina A (2017) High gradient linac for proton therapy. Phys Rev Accel Beams 20:040101
33. Amaldi U, Bonomi R, Braccini S et al (2010) Accelerators for hadrontherapy: From Lawrence cyclotrons to linacs. Nucl Instrum Methods Phys Res, Sect A 620:563577

34. Higo T (2012) Recent high-gradient test result at KEK. In: Proceedings of Linear Collider Workshop 2012, Arlington, USA
35. Dolgashev V (2013) Recent high gradient tests at SLAC. In: Proceedings of HG2013, ICTP Trieste, Italy
36. Wang JW, Loew GA (1997) Field emission and rf breakdown in high-gradient room-temperature linac structures. Technical Report SLAC-PUB-7684, SLAC
37. Mesyats G, Trans IEEE (1983) Explosive processes on the cathode in a vacuum discharge. Electr Insul 18:218–225
38. Fursey G, Trans IEEE (1985) Field emission and vacuum breakdown. Electr Insul 20:659–670
39. Wuensch W (2002) High-gradient breakdown in normal-conducting rf cavities. In: Proceedings of EPAC2002, Paris, France
40. Dolgashev V, Tantawi S (2001) Simulations of currents in X-band accelerator structures using 2D and 3D particle-in-cell code. In: Proceedings of PAC2001, Chicago, USA
41. Adolphsen C, Baumgartner W, Jobe K et al (2001) Processing studies of X-band accelerator structures at the NLCTA. In: Proceedings of PAC2001, Chicago, USA
42. Munroe B, Zhang J, Xu H et al (2016) Experimental high gradient testing of a 17.1 GHz photonic band-gap accelerator structure. Phys Rev Accel Beams 19:031301
43. Degiovanni A, Wuensch W, Navarro J (2016) Comparison of the conditioning of high gradient accelerating structures. Phys Rev Accel Beams 19:032001
44. Dolgashev V, Raubenheimer T (2004) Simulation of rf breakdown effects on NLC beam. In: Proceedings of LINAC2004, Lübeck, Germany
45. Adolphsen C (2005) Advances in normal conducting accelerator technology from the X-band Linear Collider program. In: Proceedings of PAC2005, Knoxville, USA
46. Palaia A, Jacewicz M, Ruber R et al (2013) Effects of rf breakdown on the beam in the Compact Linear Collider prototype accelerator structure. Phys Rev ST Accel Beams 16:081004
47. Shi J (2012) Detuning of T18 after high power test. In: Proceedings of HG2012, Tsukuba, Japan
48. Grudiev A, Wuensch W (2008) Design of an X-band accelerating structure for the CLIC main linac. In: Proceedings of LINAC08, Victoria, Canada
49. Jones R, Adolphsen C, Wang J et al (2006) Wakefield damping in a pair of X-band accelerators for linear colliders. Phys Rev ST Accel Beams 9:102001
50. Marsh R, Shapiro M, Temkin R et al (2011) X-band photonic band-gap accelerator structure breakdown experiment. Phys Rev ST Accel Beams 14:021301
51. Forno M, Dolgashev V, Bowden G et al (2016) rf breakdown tests of mm-wave metallic accelerating structures. Phys Rev Accel Beams 19:011301
52. Forno M, Dolgashev V, Bowden G et al (2016) Experimental measurements of rf breakdowns and deflecting gradients in mm-wave metallic accelerating structures. Phys Rev Accel Beams 19:051302
53. Kilpatrick W (1957) Criterion for vacuum sparking designed to include both rf and dc. Rev Sci Instrum 28:824–826
54. Braun H, Döbert S, Wilson I et al (2003) Frequency and temperature dependence of electrical breakdown at 21, 30, and 39 GHz. Phys Rev Lett 90:224801
55. Döbert S, Fandos R, Grudiev A, et al (2007) High power test of an X-band slotted-iris accelerator structure at NLCTA. In: Proceedings of PAC2007, Albuquerque, USA
56. Adolphsen C (2003) Normal-conducting rf structure test facilities and results. In: Proceedings of PAC2003, Portland, USA
57. Wang F (2008) Breakdown characteristics study on an 18 cell X-band structure. In: Proceedings of AAC2008, Santa Cruz, USA
58. Grudiev A, Calatroni S, Wuensch W (2009) New local field quantity describing the high gradient limit of accelerating structures. Phys Rev ST Accel Beams 12:102001
59. Timko H, Matyash K, Schneider R et al (2011) A one-dimensional particle-in-cell model of plasma build-up in vacuum arcs. Contrib Plasma Phys 51:1
60. Nordlund K, Djurabekova F (2012) Defect model for the dependence of breakdown rate on external electric fields. Phys Rev ST Accel Beams 15:071002

61. Dolgashev V, Tantawi S (2003) Effect of rf parameters on breakdown limits in high-vacuum X-band structures. Technical Report SLAC-PUB-10175, SLAC
62. Pritzkau D (2001) rf Pulsed Heating. Ph.D. thesis, SLAC
63. Wang F, Adolphsen C, Nantista C (2011) Performance limiting effects in X-band accelerators. Phys Rev ST Accel Beams 14:010401
64. Wuensch W (2007) Progress in understanding the high-gradient limitations of accelerating structures. In: Proceedings of APAC2007, Indore, India
65. Shao J, Chen H, Du Y et al (2014) Observation of temporal evolution following laser triggered rf breakdown in vacuum. Phys Rev ST Accel Beams 17:072002
66. Nantista C, Adolphsen C, Wang F (2010) A dual-moded cavity for rf breakdown studies. In: Proceedings of IPAC2010, Kyoto, Japan
67. Wang F, Adolphsen C, Nantista C (2011) Initial high power test results of an X-band dual-moded coaxial cavity. In: Proceedings of PAC2011, New York, USA
68. Kuzikov S, Kazakov S, Jiang Y et al (2010) Asymmetric bimodal accelerator cavity for raising rf breakdown thresholds. Phys Rev Lett 104:214801
69. Jiang Y, Kuzikov S, Kazakov S et al (2011) Multi-harmonic test setup for rf breakdown studies. Nucl Instrum Methods Phys Res Sect A 657:71–77
70. Degiovanni A, Doebert S, Farabolini W et al (2014) Diagnostics and analysis techniques for high power X-band accelerating structures. In: Proceedings of LINAC2014, Geneva, Switzerland
71. Wuensch W, Degiovanni A, Calatroni S et al (2017) Statistics of vacuum breakdown in the high-gradient and low-rate regime. Phys Rev Accel Beams 20:011007
72. Wang F, Adolphsen C (2009) Localization of rf breakdowns in a standing wave cavity. Phys Rev ST Accel Beams 12:042001
73. Klavins J, Dementjevs S, Locans U et al (2013) Breakdown localization studies on the SWISSFEL C-band test structures. In: Proceedings of IPAC2013, Shanghai, China
74. Degiovanni A, Farabolini W, Rajamäki R et al (2016) Breakdown localization in rf structures. In: Proceedings of CLIC Workshop 2016, Geneva, Switzerland
75. Abe T, Kageyama T, Sakai H et al (2016) Breakdown study based on direct in situ observation of inner surfaces of an rf accelerating cavity during a high-gradient test. Phys Rev Accel Beams 19:102001
76. Fontenla A (2015) Post-Mortem analysis: SEM imaging review. In: Proceedings of MeVArc2015, Lapland, Finland
77. Wu X, Shi J, Chen H et al (2017) High-gradient breakdown studies of an X-band Compact Linear Collider prototype structure. Phys Rev Accel Beams 20:052001
78. Teo K, Minoux E, Hudanski L et al (2005) Carbon nanotubes as cold cathodes. Nature 437:968
79. Ganter R, Bakker R, Gough C et al (2006) Nanosecond field emitted and photo-field emitted current pulses from ZrC tips. Nucl Instrum Methods Phys Res Sect A 565:423–429
80. Leemann S (2007) Characterization of electron bunches from field emitter array cathodes for use in next-generation X-ray free electron lasers. Ph.D. thesis, Suisse:EPFL
81. Li X, Li M, Dan L et al (2013) Cold cathode rf guns based study on field emission. Phys Rev ST Accel Beams 16:123401
82. Baryshev S, Antipov S, Shao J et al (2014) Planar ultrananocrystalline diamond field emitter in accelerator radio frequency electron injector: Performance metrics. Appl Phys Lett 15:203505
83. Fowler R, Nordheim L (1928) Electron emission in intense electric fields. Proc Roy Soc London A 119:173–181
84. Gadzuk J, Plummer E (1973) Eielci Emission Energy Distribution (FEED). Rev Mod Phys 45:3
85. Fursey G (2007) Field emission in vacuum microelectronics. In: Brodie I, Schwoebel P (eds) Microdevices. Springer Science and Business Media, Berlin
86. Forbes R, Deane J (2007) Reformulation of the standard theory of Fowler-Nordheim tunnelling and cold field electron emission. Proc Roy Soc London A 463:2907–2927

87. Chen H, Du Y, Gai W et al (2012) Surface-emission studies in a high-field rf gun based on measurements of field emission and Schottky-enabled photoemission. Phys Rev Lett 109:204802
88. Zadin V, Pohjonen A, Aabloo A et al (2014) Electrostatic-elastoplastic simulations of copper surface under high electric fields. Phys Rev ST Accel Beams 17:103501
89. Norem J, Wu V, Moretti A et al (2003) Dark current, breakdown, and magnetic field effects in a multicell, 805 MHz cavity. Phys Rev ST Accel Beams 6:072001
90. Insepov Z, Norem J (2013) Can surface cracks and unipolar arcs explain breakdown and gradient limits? J Vac Sci Technol A 31:011302
91. Wang F (2015) The macroscopic field emission. In: Proceedings of HG2015, Beijing, China
92. Jensen K, Lau Y, Feldman D et al (2008) Electron emission contributions to dark current and its relation to microscopic field enhancement and heating in accelerator structures. Phys Rev ST Accel Beams 11:081001
93. Marinov T, Hariharan S (2009) Modeling of field emission from nanowires. J Appl Phys 105:064308
94. Kyritsakis A, Kokkorakis G, Xanthakis J et al (2010) Self focusing of field emitted electrons at an ellipsoidal tip. Appl Phys Lett 97:023104
95. Filip M, Filip L (2011) Electronic and field emission properties of two-dimensional nanotori. J Vac Sci Technol B 29:02B105
96. Patterson A, Akinwande A (2015) Elementary framework for cold field emission from quantum-confined, non-planar emitters. J Appl Phys 117:174311
97. Noer R, Niedermann P, Sankarraman N et al (1986) Electron field emission from intentionally introduced particles on extended niobium surfaces. J Appl Phys 59:3851–3860
98. Lysenkov D, Müller G (2005) Field emission measurement techniques for the optimisation of carbon nanotube cathodes. Int J Nanotechnol 2:3
99. Pandey A, Müller G, Reschke D et al (2009) Field emission from crystalline niobium. Phys Rev ST Accel Beams 12:023501
100. Han J, Bähr J, Grabosch H et al (2005) Dark current and multipacting in the photocathode rf guns at PITZ. In: Proceedings of PAC2005, Knoxville, USA
101. Dowell D, Jongewaard E, Limborg C, et al (2007) Measurement and analysis of field emission electrons in the LCLS gun. In: Proceedings of PAC2007, Albuquerque, USA
102. Xiang R, Arnold A, Kamps T et al (2014) Experimental studies of dark current in a superconducting rf photoinjector. Phys Rev ST Accel Beams 17:043401
103. Wang D, Gai W, Tang C et al (2016) Interaction of an ultrarelativistic electron bunch train with a W-band accelerating structure: High power and high gradient. Phys Rev Lett 116:054801
104. Wang P, Zha H, Syratchev I et al (2017) rf design of a pulse compressor with correction cavity chain for klystron-based compact linear collider. Phys Rev Accel Beams 20:112001

Chapter 2
Experimental Research of Laser-Triggered rf Breakdown

Abstract The nature of rf breakdown appears to be largely unpredictable, leading to difficulties in conducting a systematic and conclusive investigation. This chapter introduces a novel method to trigger rf breakdown with high intensity laser so that its occurrence location and moment can be well controlled. The experiment has been performed on an S-band 1.6-cell photocathode rf gun at the Accelerator Laboratory of Tsinghua University. Multiple breakdowns have been observed within one rf pulse due to power flow between cells after the initial explosive electron emission. Similarities of the laser-triggered rf breakdowns to those occurring in the course of cavity conditioning and normal operation have been unraveled by comparing the post breakdown signals. Through measurement and detailed analysis of the time dependence of the collected current at the gun exit and the stored rf energy inside the cavity, the time evolution of the rf breakdown process has been revealed which will no doubt benefit the research of high gradient accelerating structures.

2.1 Physical Background

It is generally believed that strong field emission from surface exposed to high electric field is the trigger of rf breakdown [1–3]. The strong emission current can melt and vaporize the surface, leading to plasma generation and explosive electron emission which will further cause cavity detuning, rf field collapse, and rf power reflection etc. [3, 4]. To understand the rf breakdown phenomenon, it is necessary to trace the whole procedure from the trigger in microscopic scale (size of field emitter: nanometer to micrometer; duration of EEE: tens of nanosecond) to the structure response in macroscopic scale (size of cavity: tens of centimeter; duration of field variation: microsecond) [3]. However, the occurrence location and moment of rf breakdown are both highly unpredictable [3]. Moreover, it's usually difficult to trace the occurrence of breakdown reversely from the structure response with high accuracy. As a result, thorough and conclusive nature of the entire rf breakdown procedure is yet to be discovered despite previous extensive experimental and theoretical efforts.

Short pulse laser is broadly applied in scientific research as well as industrial manufacturing. Photocathode rf guns employ low intensity laser to generate high

J. Shao, *Investigations on rf Breakdown Phenomenon in High Gradient Accelerating Structures*, Springer Theses, https://doi.org/10.1007/978-981-10-7926-9_2

quality electron beam by photoemission [5]. Meanwhile, laser ablation, an advanced machining technology, employs high intensity laser to effectively remove material from surface with high precision [6–9].

In laser ablation, short pulse (femtosecond to picosecond) high intensity laser can directly vaporize the surface. Thus, it's natural to consider using well-controlled laser to trigger EEE and rf breakdown rather than depending on unpredictable field emission. In a previous study, researchers from Brookhaven National Laboratory (BNL) have successfully triggered EEE in a photocathode rf gun by picosecond-laser with intensity higher than 10^9 W/cm^2. The laser-triggered EEE was mainly viewed as an electron source in their study and its properties were compared with those of photoelectron emission and field emission [10].

In the experimental research introduced in this chapter, high intensity laser has been applied to trigger EEE and rf breakdown in order to study the following temporal evolution in rf structures. It is shown that an intense laser can offer a more controllable and flexible method for rf breakdown studies.

2.2 Experimental Setup

The laser-triggered rf breakdown experiment was conducted at one of the S-band photocathode rf gun beam lines at the Accelerator Laboratory of Tsinghua University [11]. This section will introduce the photocathode rf gun and the diagnostics of the beam line.

2.2.1 S-Band Photocathode rf Gun

The 1.6-cell gun, as illustrated in Fig. 2.1, operates at 2856 MHz with an rf pulse length of 6 μs, rise time of 2 μs, and fall time of 2 μs [11]. The cathode surface of the gun is a solid copper plate. With 4.8 MW input power, the maximum electric field on the central area of the cathode surface is 58 MV/m. The gun works at TM_{010} π mode, in which the phase advance between the half cell and the full cell is 180°. A racetrack slot is opened at the full cell to couple the input power. Another slot with similar dimensions is placed oppositely for pumping and suppressing the dipole-field. The cold test results of the gun is listed in Table. 2.1, which will also be used in the equivalent circuit model in following sections.

In normal operation a UV laser (wavelength 266 nm, pulse width 1.2 ps full width at half maximum, 1 mm^2 spot size on the cathode, and 2 mJ maximum energy) is directed onto the central diamond polished area of the cathode to generate photoelectron emission. During the laser-triggered breakdown experiment, the laser was directed at the cathode ~0.5 μs before the end of the flat top after the cavity had been fully filled. The mirror inside the vacuum chamber at the gun exit was remotely controlled so that the breakdown location triggered by the laser can be changed. In

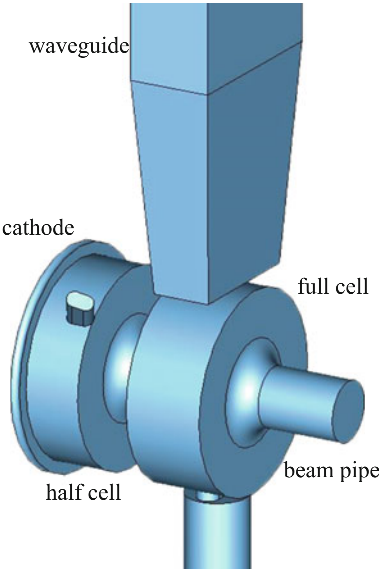

Fig. 2.1 The three-dimensional model the S-band 1.6-cell photocathode rf gun (only shows the in-vacuum part) [11]

Table 2.1 Cold test results of the S-band 1.6-cell photocathode rf gun

	π mode	Half cell	Full cell
Frequency (MHz)	2855.700	2853.575	2854.550
Q_0	6526	3835[a]	12,000
Q_e	10,442	/	/
Field balance	1	/	/

[a] Indirect calculation

the experiment, an offset up to 1.5 mm was achieved and the surface electric field varied less than 0.2%.

2.2.2 Diagnostics

A schematic layout of the experiment is shown in Fig. 2.2. Diagnostics involved in the experiment were a bidirectional coupler to monitor the input and reflected rf signals, a loop antenna (pickup) in the full cell to monitor the rf signal inside the cavity, a Faraday cup outside the gun to measure the beam current during breakdown events, and a CCD camera to monitor and index the breakdown location through the viewport at the half cell. All signals were recorded using a 50 Gs/s sampling rate, 12 GHz bandwidth digital scope (Tektronix MSO/DPO70000 series) synchronized to the incoming laser signal or to the input rf signal when the laser pulse was absent.

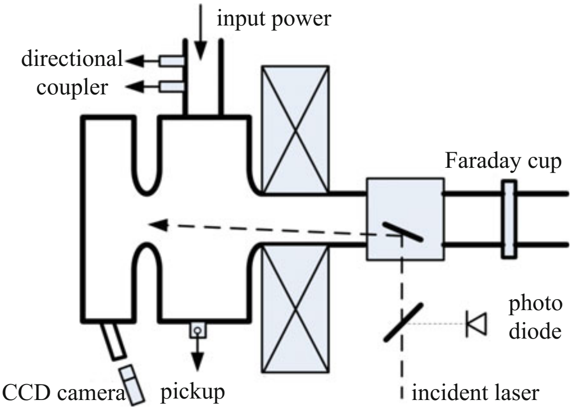

Fig. 2.2 Setup of the laser-triggered rf breakdown experiment at Tsinghua University

2.3 Experiment Observation

2.3.1 Surface Damage Test

To study the potential cathode damage from the high intensity laser, a copper sample with similar surface condition as the cathode was tested with various laser intensity prior to the laser-triggered rf breakdown experiment. The sample was then analyzed by WLI and SEM.

The energy intensity of picosecond-laser ablation threshold on copper surface has been reported to be 170 mJ/cm^2 [12]. However, ablation spots were found on the sample within the laser induced melting area even with an average laser energy intensity as low as 10 mJ/cm^2 (power intensity of 8 GW/cm^2), as shown in Fig. 2.3. With 30 pulses accumulated, the maximum damage depth was found to be 6 μm and the total removal volume was larger than 3×10^4 μm^3. The average ablation depth of each single laser pulse was 200 nm, which fell into the typical range of picosecond-laser ablation on copper [12]. The remarkably lower ablation threshold observed were probably caused by the non-uniform intensity distribution within the laser spot. This laser power intensity also agrees with the previous experiment conducted in BNL [10].

Features such as melting, droplets, and recrystallization within the laser spots have been found by the SEM, as shown in Fig. 2.4a, b. The features are similar with those discovered in rf breakdown spots in high gradient accelerating structures, as illustrated in Fig. 2.4c [13].

The test results confirm the copper surface damage caused by high intensity laser. Due to the similarity between the laser ablation spots and the rf breakdown spots where EEE occurs, the high intensity laser was expected to trigger EEE and rf breakdown in high power test with the photocathode rf gun.

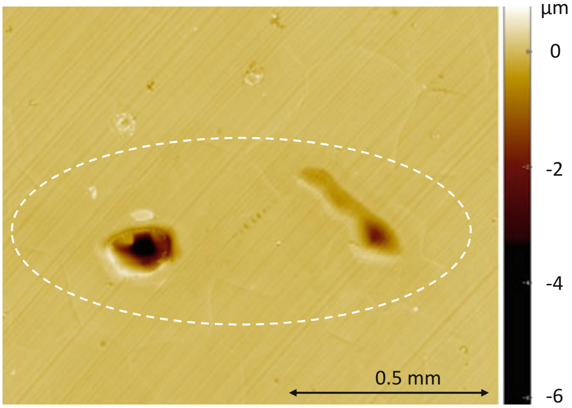

Fig. 2.3 Surface examination by WLI. The white dashed circle indicates the laser spot boundary

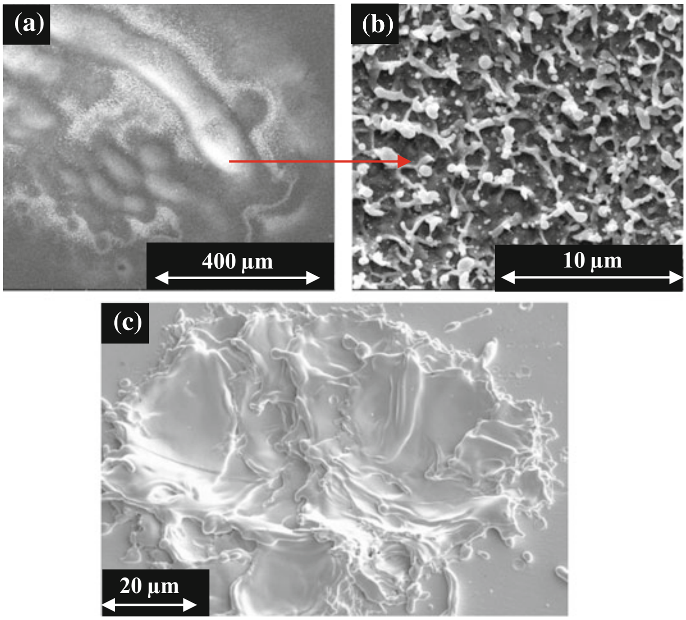

Fig. 2.4 Surface examination by SEM. **a**–**b** Treated by high intensity laser; **c** After rf breakdown [13]

2.3.2 High Power Test

2.3.2.1 Normal Condition

In normal operation of the S-band photocathode rf gun, a laser pulse with energy less than 5 μJ is used to generate a ∼100 pC photoelectron bunch when the gun is fully filled. The BDR is usually lower than $\sim 10^{-4}$/pulse. Figure 2.5 shows the typical recorded signals without rf breakdown, including the waveforms of input and reflected rf pulses in Fig. 2.5a, the rf pickup signal in Fig. 2.5b, and the Faraday cup signal excited by the emitted photoelectrons in Fig. 2.5c. The origin of the time axis (t = 0) has been set to the moment when the incident laser hits the cathode.

The duration of the photoelectron current is several picoseconds and the Faraday cup signal appears to be a damped oscillation lasting tens of nanoseconds due to ringing in the data acquisition system. Such oscillation contains the system transfer function of the Faraday cup circuit which can be extracted later to rebuild the time structure of rf breakdown currents. More details will be discussed in the following sections.

Fast Fourier transform (FFT) has been applied onto the rf field signal to study the spectrum. Only the 2856 MHz fundamental mode of the rf gun could be seen, as illustrated in Fig. 2.5d.

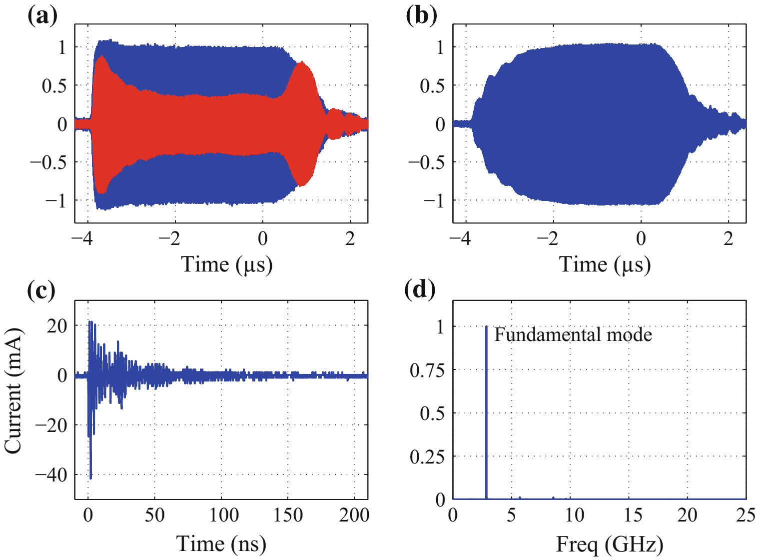

Fig. 2.5 Typical waveforms of normal condition without rf breakdown. **a** Normalized input (blue) and reflected (red) wave; **b** Normalized rf field inside the full cell; **c** Photoelectron current; **d** Normalized spectrum of the rf field

2.3.2.2 Spontaneous rf Breakdown

Like in other high power rf devices, rf breakdown may occasionally occur when the photocathode gun is pushed to its maximum operational gradient, even without the laser. During the experiment, at the gradient of 58 MV/m, tens of rf breakdown events were recorded over hundreds of thousands of rf pulses.

When an rf breakdown took place, spikes and sequential oscillation could be observed in the envelope of the pickup signal. Similar spikes were also found in the refection signal. Significant charge was captured by the Faraday cup. Typical waveforms of spontaneous rf breakdown are illustrated in Fig. 2.6a–c.

Apart from the fundamental mode, the third harmonic 8568 MHz could also be detected in the spectrum in rf breakdown events, as illustrated in Fig. 2.6d.

In the high power test, 29 spontaneous rf breakdown events were recorded. The occurrence moment were randomly distributed within the rf pulse, as illustrated in Fig. 2.7.

2.3.2.3 Laser-Triggered rf Breakdown

During the high power test with high intensity laser, the gradient on the cathode was limited to 48 MV/m. Under such condition, normal photoemission process occurred

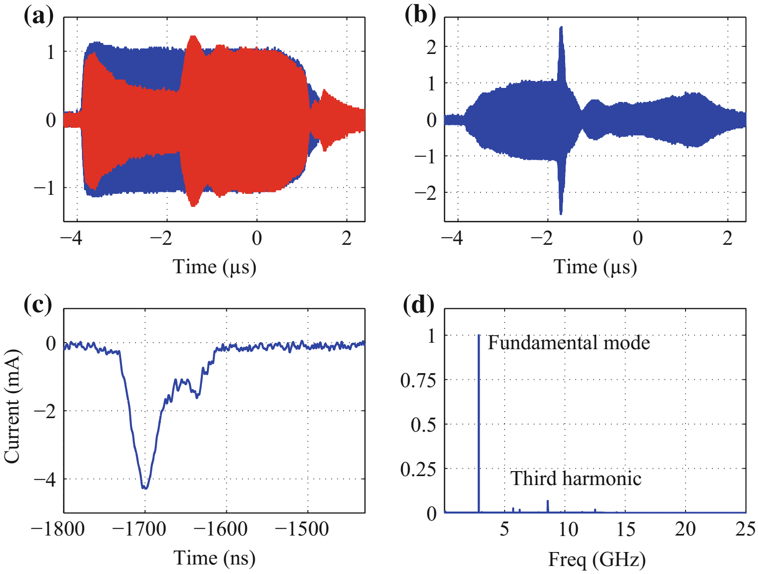

Fig. 2.6 Typical waveforms of spontaneous rf breakdown. **a** Normalized input (blue) and reflected (red) wave; **b** Normalized rf field inside the full cell; **c** rf breakdown current; **d** Normalized spectrum of the rf field

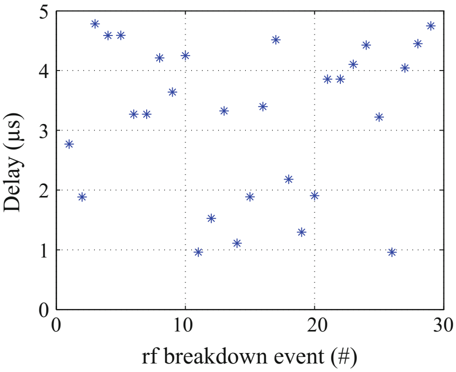

Fig. 2.7 The delay between the occurrence of rf breakdown and the rising edge of rf pulse in spontaneous rf breakdown events

without breakdown when the laser intensity was very low ($< 5\,\mu$J). As the laser energy was increased, the rf breakdown rate also increased. At laser energies greater than 100 μJ, breakdowns occurred at every rf pulse. The corresponding average laser energy intensity was 10 mJ/cm^2, which agreed well with the laser ablation threshold detected on the sample.

Similar to the spontaneous rf breakdown events, spikes could be observed in both the pickup and the refection signal. Even higher rf breakdown current up to the order of 100 mA could be detected by the Faraday cup. Given the duration of ~100 ns, the emitted charge was more than 10 nC, two orders of magnitude higher than that of the normal photoelectron (~100 pC). Typical waveforms of laser-triggered rf breakdown are illustrated in Fig. 2.8a–c). The third harmonic 8586 MHz could also been detected in the spectrum as in the spontaneous rf breakdown events, as illustrated in Fig. 2.8d.

In the experiment, ~1000 laser trigger rf breakdown events were recorded. The occurrence moment was solely determined by the laser incident moment.

Besides, the occurrence location was also well controlled by the laser. When an rf breakdown was triggered by the high intensity laser, a bright spot could be observed by the CCD camera through the viewport at the half cell, as shown in Fig. 2.9a. This bright spot was not observed when only photoelectrons were emitted without rf breakdown. Its position followed the tilting of the UV laser mirror at the gun exit. Figure 2.9b shows the image taken when the light was on; the dark mark at the same place also confirmed the rf breakdown location. This bright spot together with the high charge indicate the presence of a local plasma during the EEE process near the rf breakdown spot.

Formation of the laser induced pre-breakdown conditions including melting and ablation of copper occur on a scale of tens of picoseconds [14, 15]. Meanwhile, the physical evolution of EEE is around a hundred nanoseconds [16]. Therefore, the average gradient inside the cavity should play a more important role than the instant

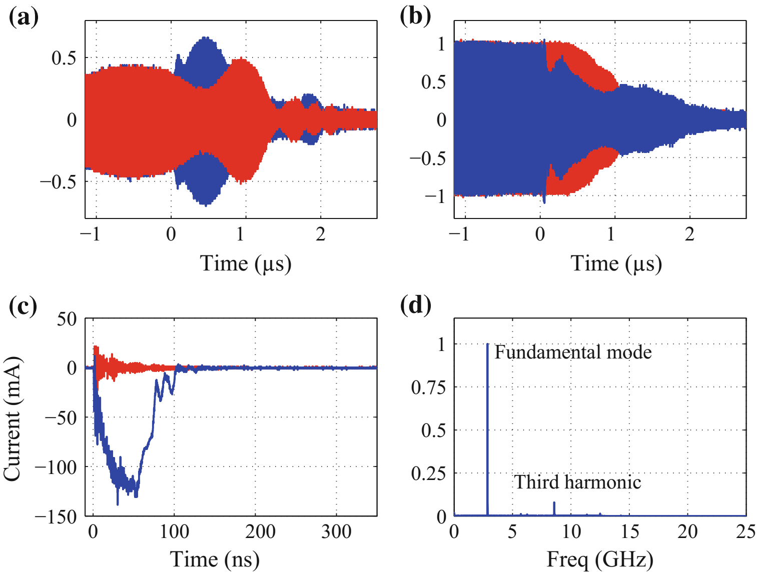

Fig. 2.8 Waveforms of laser trigger rf breakdown. The blue and red lines in (**a**–**c**) denote the rf breakdown event and the normal event, respectively. **a** Normalized reflected wave; **b** Normalized rf field inside the full cell; **c** Current detected by the Faraday cup; **d** Normalized spectrum of the rf field

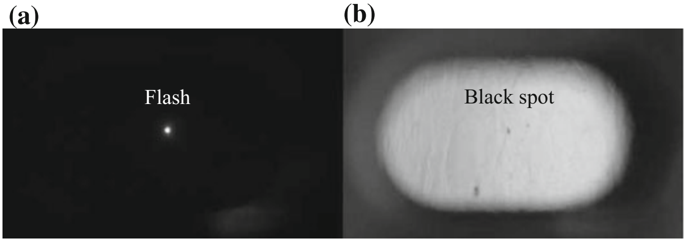

Fig. 2.9 Cathode images. **a** During rf breakdown when light was off; **b** After breakdown when light was on

electric field when laser hits the cathode in the breakdown strength (represented by the charge collected at the exit of the cavity).

This has been confirmed in the high power test by adjusting the laser incident moment within one rf period and the amplitude of electric field on the cathode. At fixed laser intensity and field amplitude, the detected charge has been found to be irrelevant to the laser incident moment, as illustrated in Fig. 2.10. However, strong dependence has been observed when adjusting the laser intensity and the field amplitude, as illustrated in Fig. 2.11.

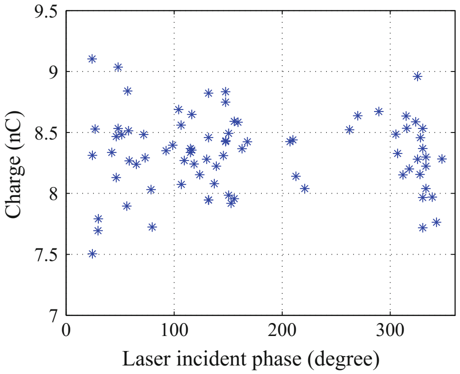

Fig. 2.10 Captured charge measured at the exit of the rf gun as a function of the laser incident moment

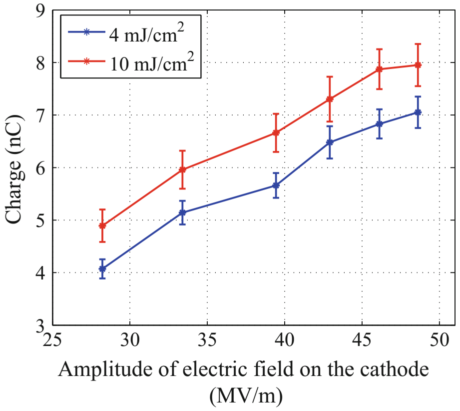

Fig. 2.11 Captured charge measured at the exit of the rf gun as a function of electric field at the cathode center with two different average laser input energy intensities

2.4 Basic Analysis

To understand the phenomena observed in the high power test, multiple methods have been applied to analyze rf breakdown events in the S-band 1.6 cell photocathode rf gun.

2.4.1 Modes Evolution

In rf breakdown events, the spikes observed in the pickup and the reflection signal are caused by the excitation of higher order modes of the gun. The breakdown current serves as another source apart from the original input rf power from klystron. The current lasts for tens of nanoseconds and contains a bunch train of captured electrons separated by one rf cycle of the fundamental mode. Each bunchlet of electrons comes into phase with the rf wave after the initial acceleration in the half cell and the duration is tens of picosecond (from simulation using the PARMELA code [17]). Thus HOMs of the cavity can be excited by the short bunchlets. In particular, HOMs whose frequency is close to a harmonic of the fundamental mode can be coherently reinforced by the bunch train [18].

The frequency of the TM_{410} mode of the photocathode rf gun is found to be close to the third harmonic by CST microwave studio simulation [19]. Its field pattern is shown in Fig. 2.12 (a simplified model without the waveguide coupling slot, the pumping slot, or observation hole, etc.).

In order to study the evolution of the fundamental mode and HOMs during rf breakdown events, a short time FFT has been applied along the recorded pickup signal with a 10 ns window moving at 0.5 ns per step. With an oscilloscope sampling rate of 50 GS/s, each window contains 500 data points. Therefore, the frequency resolution of the method is 100 MHz which is sufficient to distinguish the fundamental mode and HOMs.

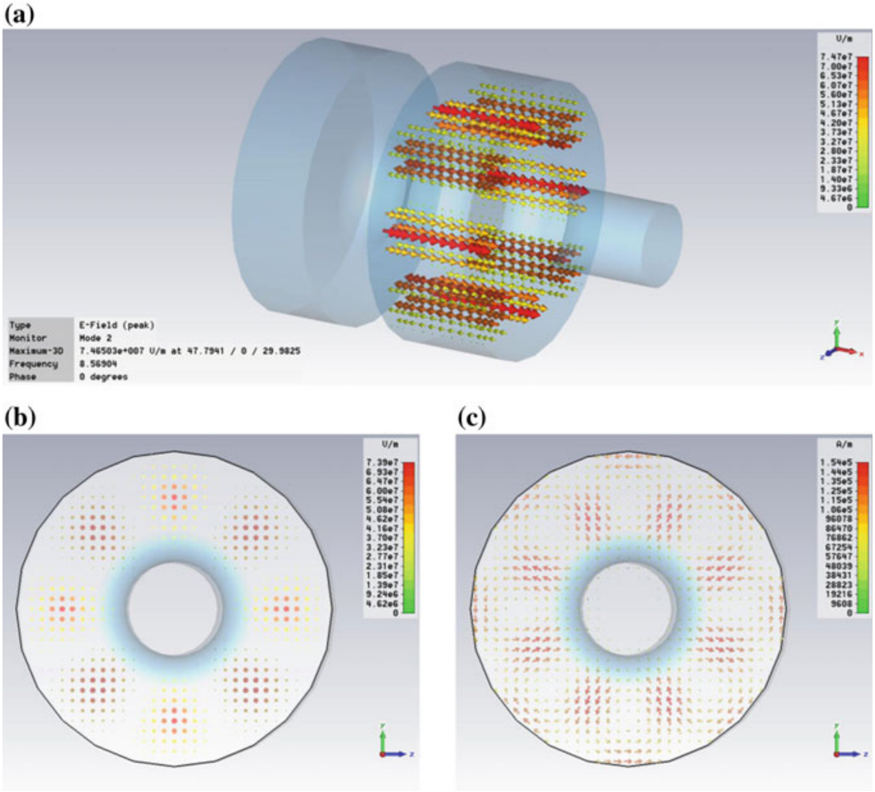

Fig. 2.12 Field pattern of the TM_{410} mode of the rf gun. **a** Simplified model and three-dimensional electric field distribution; **b** Two-dimensional electric field distribution; **c** Two-dimensional magnetic field distribution

2.4.1.1 Spontaneous rf Breakdown

Applying this method to spontaneous rf breakdown events, results in Fig. 2.13c, d clearly show the excitation of the TM_{410} mode associated with the collapse of the fundamental mode. Multiple azimuthal variations of the EM pattern of the HOM are caused by the large divergence of emitted electrons. The onset of an rf breakdown can then be defined at the moment of excitation of the TM_{410} mode. In the following analysis and discussion, the origin of the time axis of each signal is set to this moment. Besides, remarkable increase of the fundamental mode reflection can also be observed, as illustrated in Fig. 2.13a, b.

All the recorded breakdowns without laser triggers can be classified into two types, according to the breakdown current profile captured by the Faraday cup. In the single-breakdown type, there was only one current pulse; while in the multiple-breakdown type, two or more pulses could be detected within an interval of ~200 ns. In the 29 spontaneous rf breakdown events recorded, only four of them are categorized as single-breakdown type.

The rf field signals shown in Fig. 2.13 have been zoomed in around the onset of rf breakdown and compared with the current signal detected by the Faraday cup at the

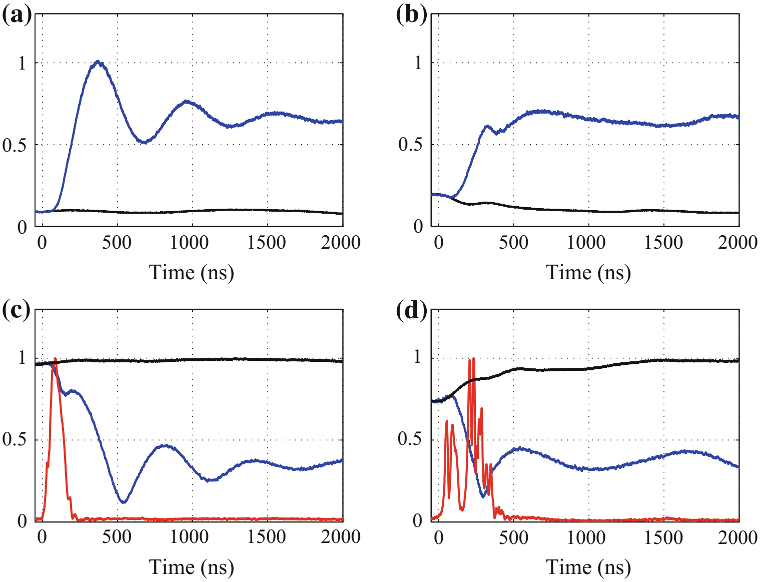

Fig. 2.13 Evolution of the fundamental mode and the HOM in spontaneous rf breakdown events. **a**, **c** Single-breakdown type; **b**, **d** Multiple-breakdown type. **a**, **b** Normalized FFT amplitude of the reflection signal, including the fundamental mode without (black) and with (blue) rf breakdown. **c**, **d** Normalized FFT amplitude of the pickup signal, including the fundamental mode without rf breakdown (black), the fundamental mode with rf breakdown (blue), and the TM_{410} mode with rf breakdown (red)

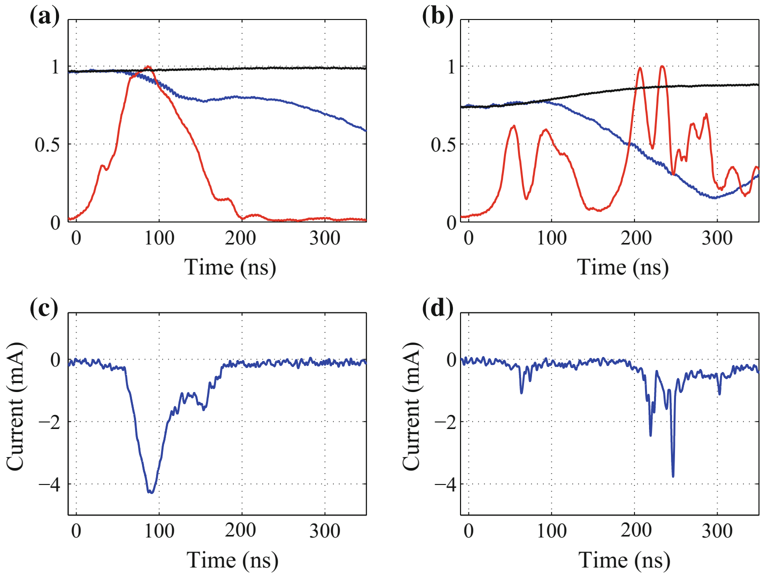

Fig. 2.14 Zoom-in view of the normalized FFT amplitude of the pickup signal (**a**, **b**) illustrated in Fig. 2.13 and the rf breakdown current (**c**, **d**). **a**, **c** Single-breakdown type; **b**, **d** Multiple-breakdown type

gun exit. The appearance and duration of the HOM match the rf breakdown current, as illustrated in Fig. 2.14. There is a 40∼140 ns time delay between the start of the collapse of the fundamental mode and the excitation of the HOM. What's more, for multiple-breakdown events, the excitation of the HOM caused by the second breakdown is always close to the end of the fundamental mode collapse. The physics behind these observation will be further studied with an equivalent circuit model of the S-band 1.6-cell photocathode rf gun in the next section.

2.4.1.2 Laser Trigger rf Breakdown

The same FFT method has also been applied to analyze the pickup signal of laser-triggered rf breakdown events and the result also indicates the excitation of the TM_{410} mode, as illustrated in Fig. 2.15. Similar to those rf breakdowns occurring without a laser trigger, laser-triggered rf breakdown can also be classified into two types according to the breakdown current pulses detected at the gun exit. However, multiple-breakdown events were quite rare and less than 10 of them were recorded out of a total of 1000 rf breakdown events.

The rf field signals shown in Fig. 2.15 have also been zoomed in around the onset of rf breakdown and compared with the current signal detected by the Faraday cup

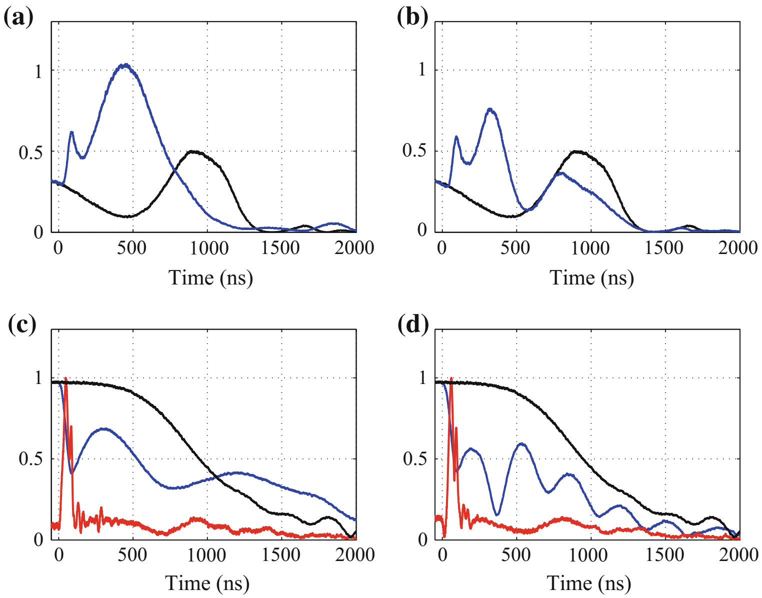

Fig. 2.15 Evolution of the fundamental mode and the HOM in laser-triggered rf breakdown events. **a**, **c** Single-breakdown type; **b**, **d** Multiple-breakdown type. **a**, **b** Normalized FFT amplitude of the reflection signal, including the fundamental mode without (black) and with (blue) rf breakdown. **c**, **d** Normalized FFT amplitude of the pickup signal, including the fundamental mode without rf breakdown (black), the fundamental mode with rf breakdown (blue), and the TM_{410} mode with rf breakdown (red)

at the gun exit, as illustrated in Fig. 2.16. The collapse time of the fundamental mode was ∼80 ns, in agreement with the duration of the Faraday cup signal. The onset of the fundamental mode collapse, the appearance of the HOM, and the starting time of the captured breakdown current all agree well with each other. Detailed discussion will also be presented with the equivalent circuit model analysis.

At a gradient of 48 MV/m, the stored energy in the full cell is 0.9 J and the average energy gain of a captured electron in the full cell is simulated to be ∼1 MeV using PARMELA code. In Fig. 2.16a, the pickup signal fell to 0.4 times its original level after the EEE occurred. Thus, ∼0.76 J energy was lost during the emission period. Assuming all the lost energy was absorbed by the captured electrons, the upper limit of the emitted charge is estimated to be 760 nC. This estimation has ignored the loss of energy gain due to the collapse of the field of the fundamental mode, otherwise the upper limit would be even higher. This upper limit is two orders of magnitude higher than the captured charge by the Faraday cup which may be caused by the large divergence of emitted electrons.

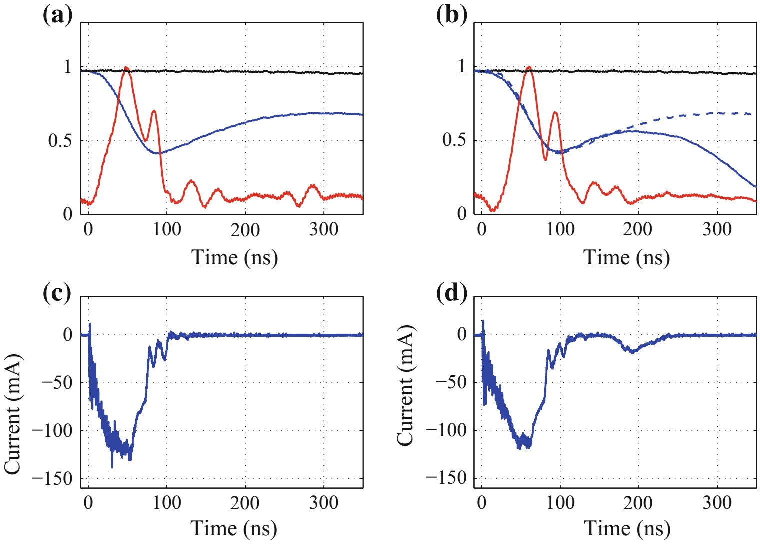

Fig. 2.16 Zoom-in view of the normalized FFT amplitude of the pickup signal (**a**, **b**) illustrated in Fig. 2.15 and the rf breakdown current (**c**, **d**). **a**, **c** Single-breakdown type; **b**, **d** Multiple-breakdown type. The blue dashed line in (**b**) indicates the evolution of the fundamental mode in single-breakdown events

2.4.2 Frequency Detuning

Apart from the 10 ns window FFT method to study the evolution of fundamental mode and HOMs, another FFT method with longer window (1000 ns) and higher frequency domain resolution (1 MHz) has also been applied to study the frequency shift of the gun after the onset of rf breakdown. Results show a ∼2 MHz frequency downshift in signle-breakdown events and no frequency shift in multi-breakdown events. The former case could be explained as plasma propagating along the axis (high E-field region) will detune two cells to a lower frequency. However, the latter case is yet to be clarified. It seems that the second breakdown detunes the cells to a higher frequency, hence cancels the frequency downshift by the first breakdown.

2.4.3 Time Structure of rf Breakdown Current

Because the occurrence location of the spontaneous rf breakdown is highly random, the emission current might not be captured by the Faraday cup which leads to difficulties in analyzing its time structure. However, the EEE location in laser-triggered events was well controlled to be near the cathode center so that the capture ratio of

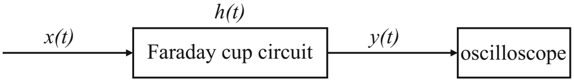

Fig. 2.17 Detected signal by Faraday cup as convolution of the real emission current signal and the transfer function

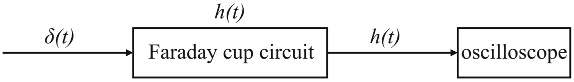

Fig. 2.18 Detection of an impulse function by the Faraday cup circuit

the Faraday cup could be higher. In the high power test, the current in laser-triggered rf breakdown events was two orders of magnitude higher than that in spontaneous ones, which also improves the signal-to-noise ratio in the following analysis.

Because of the ringing of the Faraday cup circuit, the observed signal $y(t)$ is a mixture of a real emission current signal $x(t)$ and the oscillations from its transfer function $h(t)$, as shown in Fig. 2.17. The three signals follow

$$y(t) = \int_{-\infty}^{+\infty} x(\tau)h(t-\tau)d\tau \tag{2.1}$$

As the length of the photoelectron current was only several picoseconds and even shorter than the 20 ps sampling interval of the oscilloscope, the detected photoelectron current shown in Fig. 2.5c can be viewed as the transfer function of the Faraday cup circuit, as illustrated in Fig. 2.18.

Therefore, the original rf breakdown current can be resolved by a deconvolution method [20]. Figure 2.19 shows the Faraday cup signals before and after deconvolution for both single-breakdown and multiple-breakdown events with laser trigger.

The deconvoluted time structures are slightly different in both events. The formation of a plasma during the EEE process depends on several parameters, such as surface condition, laser intensity, rf field, etc. These conditions fluctuated between every rf pulse. Thus this difference in time structure originates from the variation of different pulses rather than from different rf breakdown types. The resolved current pulses share a few common features. A significant impulse function (the deconvoluted photoelectron current) can be found at the start of the breakdown current. The deconvoluted signals also indicate that there are three stages after the onset of rf breakdown: the increasing electron emission (20∼50 ns); the steady state emission (20∼40 ns); and the decreasing emission (20∼30 ns).

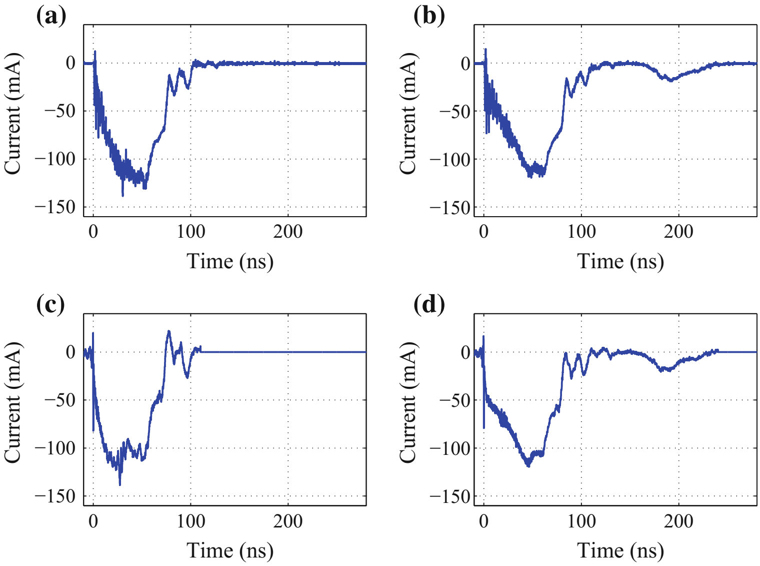

Fig. 2.19 The Faraday cup signal of a single-breakdown event (left) and a multiple-breakdown event (right). **a**–**b** Before deconvolution. **c**–**d** After deconvolution

2.5 Advanced Analysis with an Equivalent Circuit Model

An equivalent circuit model has been developed to further study the phenomena observed in the high power test and revealed in the previous analysis. With this model, most of the observations have been well explained. Multiple-breakdown is discovered to be caused by power flow between cells which is a result of the imbalanced stored energy after the first explosive electron emission.

The subscripts ‘g’, ‘1’, and ‘2’ in this section denote the power source, the full cell, and the half cell, respectively.

2.5.1 *Equivalent Circuit Model*

Accelerating structures can be modeled by RLC circuit to simulate their characters [21, 22]. A two-cell RLC circuit model has been established for the S-band 1.6-cell photocathode rf gun applied in the high power test. The parallel circuit is coupled to the power source (represented by a current source and a resistor) from the full cell, as shown in Fig. 2.20.

During an rf breakdown event, EEE occurring on the cathode generated strong emission current. To simulate this behavior, two current sources I_1 and I_2 are introduced to the circuit, as shown in Fig. 2.21. The time structures of these currents are the same as the deconvoluted result while their phases are opposite to the corresponding

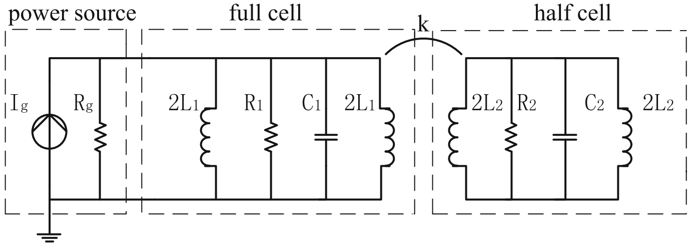

Fig. 2.20 Equivalent circuit model of the S-band 1.6-cell photocathode rf gun

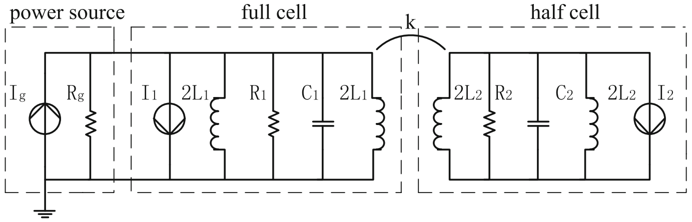

Fig. 2.21 Equivalent circuit model of the S-band 1.6-cell photocathode rf gun with rf breakdown current sources

cell voltages to absorb the stored energy. Because of the unknown current loss on the iris between cells, the amplitude of these two current sources is not necessarily the same.

Besides, frequency detuning of the two cells is also introduced to the model based on the FFT results with 1000 ns window. The detuning of each individual cell needs to be adjusted separately to meet the π mode detuning revealed from previous data.

In summary, there are four adjustable parameters in the circuit shown in Fig. 2.21, including the amplitude of the rf breakdown current and the frequency detuning of the two cells. The recorded waveforms in the high power test can be well reproduced by adjusting these parameters.

2.5.2 Basic Equations

A detailed derivation of basic equations to solve the equivalent circuit model of the S-band 1.6-cell photocathode rf gun with rf breakdown current sources is presented as following.

The coupling between two cells can be expressed as

$$\begin{cases} V_1 = 2L_1 \dfrac{di_{1,Lr}}{dt} + M\dfrac{di_{2,Ll}}{dt} \\ V_2 = 2L_2 \dfrac{di_{2,Ll}}{dt} + M\dfrac{di_{1,Lr}}{dt} \end{cases} \tag{2.2}$$

where V_1 and V_2 denote the voltage of the cells; $i_{1,Lr}$ denotes the current through the right inductor of the full cell; $i_{2,Ll}$ denotes the current through the left inductor of the half cell; M denotes the mutual inductance which can be expressed by the coupling factor k as $M = k\sqrt{4L_1L_2}$

Derived from Eq. 2.2,

$$\begin{cases} \dfrac{di_{1,Lr}}{dt} = \dfrac{1}{2L_1(1-k^2)}V_1 - \dfrac{1}{2\sqrt{L_1L_2}}\dfrac{k}{1-k^2}V_2 & (2.3) \\ \dfrac{di_{2,Ll}}{dt} = \dfrac{1}{2L_2(1-k^2)}V_2 - \dfrac{1}{2\sqrt{L_1L_2}}\dfrac{k}{1-k^2}V_1 & (2.4) \end{cases}$$

In the half cell, the current follows Kirchhoff's circuit laws as

$$I_2 + i_{2,R} + i_{2,C} + i_{2,Ll} + i_{2,Lr} = 0 \tag{2.5}$$

where $i_{2,R}$, $i_{2,C}$, and $i_{2,Lr}$ denote the current through the resistor, the capacitor, and the right inductor, which can be expressed as

$$\begin{cases} i_{2,R} = \dfrac{V_2}{R_2} \\ i_{2,C} = C_2\dfrac{dV_2}{dt} \\ \dfrac{di_{2,Lr}}{dt} = \dfrac{V_2}{2L_2} \end{cases} \tag{2.6}$$

For each cell ($m = 1, 2$), the frequency ω_m, the quality factor Q_m, the stored energy U_m, and the average wall dissipation during one rf period P_m follow

$$\begin{cases} \omega_m = \dfrac{1}{\sqrt{L_mC_m}} \\ Q_m = \dfrac{\omega_mU_m}{P_m} \\ U_m = \dfrac{1}{2}C_mV_m^2 \\ P_m = \dfrac{1}{2}\dfrac{V_m^2}{R_m} \end{cases} \tag{2.7}$$

Thus, the inductance of each cell can be derived as

$$L_m = \frac{1}{\omega_m^2C_m} = \frac{(R/Q)_m}{\omega_m} \tag{2.8}$$

Taking Eqs. 2.4, 2.6, and 2.8 into Eq. 2.5, it can be derived that

$$\frac{d^2V_2}{\omega_2^2dt^2}+\frac{1}{\omega_2Q_2}\frac{dV_2}{dt}+\frac{1}{2}(1+\frac{1}{1-k^2})V_2=\frac{1}{2}\sqrt{\frac{\omega_1}{\omega_2}\frac{(R/Q)_2}{(R/Q)_1}}\frac{k}{1-k^2}V_1 \\ -\frac{(R/Q)_2}{\omega_2}\frac{dI_2}{dt} \tag{2.9}$$

Similarly, the current follows Kirchhoff's circuit laws in the full cell as

$$I_g+I_1+i_{R_g}+i_{1,R}+i_{1,C}+i_{1,Ll}+i_{1,Lr}=0 \tag{2.10}$$

where i_{R_g}, $i_{1,R}$, $i_{1,C}$, and $i_{2,Ll}$ denote the current through the source resistor, the resistor, the capacitor, and the left inductor, respectively. These current follow

$$\begin{cases} i_{R_g} &= \dfrac{V_1}{R_g} \\ i_{1,R} &= \dfrac{V_1}{R_1} \\ i_{1,C} &= C_1\dfrac{dV_1}{dt} \\ \dfrac{di_{1,Ll}}{dt} &= \dfrac{V_1}{2L_1} \end{cases} \tag{2.11}$$

Taking Eqs. 2.3, 2.8, and 2.11 into Eq. 2.10, it can be derived that

$$\frac{d^2V_1}{\omega_1^2dt^2}+\frac{1}{\omega_1Q_1}\frac{dV_1}{dt}+\frac{1}{2}(1+\frac{1}{1-k^2})V_1=\frac{1}{2}\sqrt{\frac{\omega_2}{\omega_1}\frac{(R/Q)_1}{(R/Q)_2}}\frac{k}{1-k^2}V_2 \\ +\frac{(R/Q)_1}{\omega_1}\frac{d}{dt}(I_g-I_1-\frac{V_1}{R_g}) \tag{2.12}$$

In photocathode rf guns, the coupling factor $k \ll 1$. Thus, Eq. 2.9 and Eq. 2.12 can be simplified as

$$\begin{cases} \dfrac{d^2V_1}{\omega_1^2dt^2}+\dfrac{1}{\omega_1Q_1}\dfrac{dV_1}{dt}+V_1=\dfrac{k}{2}\sqrt{\dfrac{\omega_2}{\omega_1}\dfrac{(R/Q)_1}{(R/Q)_2}}V_2 \\ \qquad +\dfrac{(R/Q)_1}{\omega_1}\dfrac{d}{dt}(I_g-I_1-\dfrac{V_1}{R_g}) \\ \dfrac{d^2V_2}{\omega_2^2dt^2}+\dfrac{1}{\omega_2Q_2}\dfrac{dV_2}{dt}+V_2=\dfrac{k}{2}\sqrt{\dfrac{\omega_1}{\omega_2}\dfrac{(R/Q)_2}{(R/Q)_1}}V_1-\dfrac{(R/Q)_2}{\omega_2}\dfrac{dI_2}{dt} \end{cases} \tag{2.13}$$

To solve Eq. 2.13 numerically, the cell voltage is further expressed in the complex format as $V_m=(V_{m,r}+jV_{m,i})e^{j\omega t}$, $m=1,2$, where ω is the operation frequency of the rf gun. Then, the time derivatives of the voltages follow

$$\left\{\begin{aligned} \dot{V}_m &= [(\dot{V}_{m,r} - \omega V_{m,i}) + j(\dot{V}_{m,i} + \omega V_{m,r})]e^{j\omega t} && (2.14)\\ \ddot{V}_m &= [(\ddot{V}_{m,r} - 2\omega \dot{V}_{m,i} - \omega^2 V_{m,r}) + j(\ddot{V}_{m,i} + 2\omega \dot{V}_{m,r} - \omega^2 V_{m,i})]e^{j\omega t} && (2.15) \end{aligned}\right.$$

Only considering slow variation in the envelope and ignoring any higher order terms, Eq. 2.15 can be simplified as

$$\ddot{V}_m \approx [(-2\omega \dot{V}_{m,i} - \omega^2 V_{m,r}) + j(2\omega \dot{V}_{m,r} - \omega^2 V_{m,i})]e^{j\omega t} \tag{2.16}$$

Similarly, current items can be expressed in the complex form as

$$\left\{\begin{aligned} I_g &= (I_{g,r} + jI_{g,i})e^{j\omega t}\\ I_1 &= (I_{1,r} + jI_{1,i})e^{j\omega t}\\ I_2 &= (I_{2,r} + jI_{2,i})e^{j\omega t} \end{aligned}\right. \tag{2.17}$$

And their time derivatives are

$$\left\{\begin{aligned} \dot{I}_g &= [(\dot{I}_{g,r} - \omega I_{g,i}) + j(\dot{I}_{g,i} + \omega I_{g,r})]e^{j\omega t}\\ \dot{I}_1 &= [(\dot{I}_{1,r} - \omega I_{1,i}) + j(\dot{I}_{1,i} + \omega I_{1,r})]e^{j\omega t}\\ \dot{I}_2 &= [(\dot{I}_{2,r} - \omega I_{2,i}) + j(\dot{I}_{2,i} + \omega I_{2,r})]e^{j\omega t} \end{aligned}\right. \tag{2.18}$$

Taking Eqs. 2.14–2.18 into Eq. 2.13, the differential equation set to be solved for the photocathode rf gun is

$$\left\{\begin{aligned} \dot{V}_{1,r} &= \frac{\omega_1^2}{2\omega}[-(\frac{\omega}{\omega_1 Q_1} + \frac{(R/Q)_1\omega}{\omega_1 R_g})V_{1,r} + (\frac{\omega^2}{\omega_1^2} - 1)V_{1,i}\\ &\quad + \frac{k}{2}\sqrt{\frac{\omega_2}{\omega_1}\frac{(R/Q)_1}{(R/Q)_2}}V_{2,i} - (\frac{1}{\omega_1 Q_1} + \frac{(R/Q)_1}{\omega_1 R_g})\dot{V}_{1,i}\\ &\quad + \frac{(R/Q)_1}{\omega_1}(\dot{I}_{g,i} + \omega I_{g,r} - \dot{I}_{1,i} - \omega I_{1,r})]\\ \dot{V}_{1,i} &= -\frac{\omega_1^2}{2\omega}[(\frac{\omega^2}{\omega_1^2} - 1)V_{1,r} + (\frac{\omega}{\omega_1 Q_1} + \frac{(R/Q)_1\omega}{\omega_1 R_g})V_{1,i}\\ &\quad + \frac{k}{2}\sqrt{\frac{\omega_2}{\omega_1}\frac{(R/Q)_1}{(R/Q)_2}}V_{2,r} - (\frac{1}{\omega_1 Q_1} + \frac{(R/Q)_1}{\omega_1 R_g})\dot{V}_{1,r}\\ &\quad + \frac{(R/Q)_1}{\omega_1}(\dot{I}_{g,r} - \omega I_{g,i} - \dot{I}_{1,r} + \omega I_{1,i})]\\ \dot{V}_{2,r} &= \frac{\omega_2^2}{2\omega}[\frac{k}{2}\sqrt{\frac{\omega_1}{\omega_2}\frac{(R/Q)_2}{(R/Q)_1}}V_{1,i} - \frac{\omega}{\omega_2 Q_2}V_{2,r} + (\frac{\omega^2}{\omega_2^2} - 1)V_{2,i}\\ &\quad - \frac{1}{\omega_2 Q_2}\dot{V}_{2,i} - \frac{(R/Q)_2}{\omega_2}(\dot{I}_{2,i} + \omega I_{2,r})]\\ \dot{V}_{2,i} &= -\frac{\omega_2^2}{2\omega}[\frac{k}{2}\sqrt{\frac{\omega_1}{\omega_2}\frac{(R/Q)_2}{(R/Q)_1}}V_{1,r} + (\frac{\omega^2}{\omega_2^2} - 1)V_{2,r} + \frac{\omega}{\omega_2 Q_2}V_{2,i}\\ &\quad - \frac{1}{\omega_2 Q_2}\dot{V}_{2,r} - \frac{(R/Q)_2}{\omega_2}(\dot{I}_{2,r} - \omega I_{2,i})] \end{aligned}\right. \tag{2.19}$$

2.5.3 Parameters

To solve the differential equation set Eq. 2.19, parameters including ω_m, Q_m, $(R/Q)_m$, k, R_g, I_g, and I_m are derived from the cold test as well as the CST microwave studio simulation.

2.5.3.1 Frequency and Quality Factor

ω_1, ω_2, Q_1, and the quality of the π mode Q_π can be directly obtained in the cold test of the rf gun, which follow

$$\begin{cases} Q_1 = \dfrac{\omega_1 U_1}{P_1} \approx \dfrac{\omega_\pi U_1}{P_1} \\ Q_2 = \dfrac{\omega_2 U_2}{P_2} \approx \dfrac{\omega_\pi U_2}{P_2} \\ Q_\pi = \dfrac{\omega_\pi U_\pi}{P_\pi} = \dfrac{\omega_\pi (U_1 + U_2)}{P_1 + P_2} \end{cases} \tag{2.20}$$

Thus, Q_2 can be derived as

$$Q_2 = \alpha/(\frac{1+\alpha}{Q_\pi} - \frac{1}{Q_1}) \tag{2.21}$$

where α is defined as the ratio of stored energy in the half cell to the full cell in π mode as $\alpha \equiv \frac{U_2}{U_1} \approx \frac{l_2}{l_1}$ (l_m denotes the cell length).

2.5.3.2 Shunt Impedance

In CST microwave studio simulation, the quality factor and shunt impedance of each single cell can be obtained and their values are listed in Table. 2.2

Since $(R/Q)_1$ and $(R/Q)_2$ are only determined by the shape of cells and irrelevant to the material and surface finishing, the practice shunt impedance can be derived from these values together with the measured quality factors in the cold test.

Table 2.2 CST microwave studio simulation results of the S-band 1.6-cell photocathode rf gun

$Q_{1,CST}$	$Q_{2,CST}$	$R_{1,CST}$ (Ω)	$R_{2,CST}$ (Ω)
14,343	9736	4.33×10^6	2.17×10^6

2.5.3.3 Coupling Factor

Considering the eigenmode of the photocathode rf gun without drive currents and defining $V_1(t) = V_{1,0}\cos(\omega_\pi t + \theta_1)$ and $V_2(t) = V_{2,0}\cos(\omega_\pi t + \theta_2)$ for the π mode, Eq. 2.13 can be expressed as

$$\begin{cases} (1 - \frac{\omega_\pi^2}{\omega_1^2} + j\frac{\omega_\pi}{\omega_1 Q_1})V_{1,0} = \frac{k}{2}\sqrt{\frac{\omega_2}{\omega_1}\frac{(R/Q)_1}{(R/Q)_2}}V_{2,0} \\ (1 - \frac{\omega_\pi^2}{\omega_2^2} + j\frac{\omega_\pi}{\omega_2 Q_2})V_{2,0} = \frac{k}{2}\sqrt{\frac{\omega_1}{\omega_2}\frac{(R/Q)_2}{(R/Q)_1}}V_{1,0} \end{cases} \tag{2.22}$$

Thus, the coupling factor between the half cell and the full cell can be derived as

$$k = 2\sqrt{|1 - \frac{\omega_\pi^2}{\omega_1^2} + j\frac{\omega_\pi}{\omega_1 Q_1}||1 - \frac{\omega_\pi^2}{\omega_2^2} + j\frac{\omega_\pi}{\omega_2 Q_2}|} \tag{2.23}$$

2.5.3.4 Power Source

The coupling between the rf gun and the waveguide can be expressed as

$$\beta = \frac{Q_\pi}{Q_e} = \frac{P_e}{P_\pi} = \frac{V_{1,0}^2/R_g}{V_{1,0}^2/R_1 + V_{2,0}^2/R_2} \tag{2.24}$$

From Eq. 2.22, the voltage ratio of the half cell to the full cell can be defined as

$$\gamma \equiv \frac{|V_{2,0}|}{|V_{1,0}|} = |1 - \frac{\omega_\pi^2}{\omega_1^2} + j\frac{\omega_\pi}{\omega_1 Q_1}|/(\frac{k}{2}\sqrt{\frac{\omega_2}{\omega_1}\frac{(R/Q)_1}{(R/Q)_2}}) \tag{2.25}$$

Thus, R_g follows

$$R_g = \frac{1}{\beta}\frac{1}{1/R_1 + \gamma^2/R_2} \tag{2.26}$$

According to the transmission line theory, the voltage and current of the cavity V_{cav} and I_{cav} follow

$$\begin{cases} V_{cav} = V_1 = V_+ + V_- \\ I_{cav} = I_g - \frac{V_{cav}}{R_g} = I_+ - I_- = \frac{V_+}{R_g} - \frac{V_-}{R_g} \\ P_g = P_+ = \frac{1}{2}\frac{|V_+|^2}{R_g} \end{cases} \tag{2.27}$$

where V_+, V_-, I_+, I_+, P_+, P_g denote the forward and backward voltage, the forward and backward current, the forward power, and the klystron power, respectively. Thus, the klystron current can be derived as

$$I_g = \sqrt{\frac{8P_g}{R_g}} \tag{2.28}$$

Therefore, the parameters of the equivalent circuit model can be summarized in Table. 2.3.

2.5.4 *Analysis*

2.5.4.1 Normal Condition

The results of the equivalent circuit model and the experiment have been compared in normal event without rf breakdown to validate the model and its parameters. In this case, the frequency detuning and rf breakdown current are all set to zero. Simulation results agree well with the experimental observation, as illustrated in Fig. 2.22.

2.5.4.2 Laser-Triggered rf Breakdown

In rf breakdown events, the actual plasma proportion and corresponding influence on frequency are complex. In the equivalent circuit model, the onset of frequency detuning is chosen based on the speed of plasma movement and best match the observed rf signal during the rf breakdown event. As the breakdown occurred on the cathode, the half cell is set to be detuned by a certain value immediately after

Table 2.3 Parameters of the equivalent circuit model

Parameter	Value
f_1	2854.550 MHz
f_2	2853.575 MHz
Q_1	12000
Q_2	3835
R_1	1.81×10^6 Ω
R_2	4.28×10^5 Ω
k	2.21 %
R_g	1.08×10^6 Ω
I_g	5.96 A[a]

[a] With 4.8 MW input power

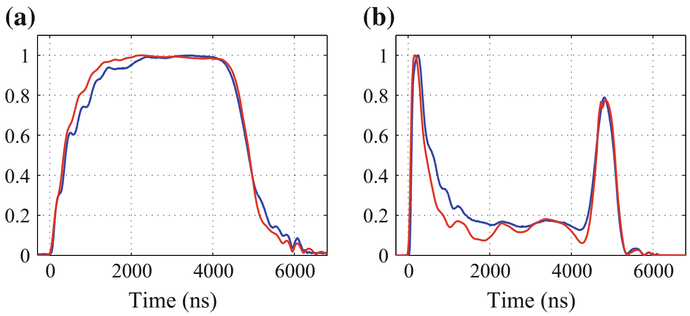

Fig. 2.22 Comparison of simulation (red) and experimental results (blue) without breakdown. **a** Normalized pickup signal. **b** Normalized reflection signal

the EEE. In a previous experiment, the highest ion speed v_s in the cold explosions has been reported to be 2×10^4 m/s [23]. Previous theoretical work has analyzed the arrival time spectra of ions and shown that ions can reach even higher speeds when the thermal energy is increased [24]. So the full cell is set to start detuning 200 ns after the onset of the breakdown and linearly shifted to a certain value. When the magnitude of the two currents is 18 A and the frequency shifts are 3.2 MHz and 0.9 MHz for the half cell and full cell respectively, the simulation agrees well with the single-breakdown experiment result, as shown in Fig. 2.23a, c. The frequency of the π-mode is therefore downshifted by 1.7 MHz, also agrees with the FFT result. The stored energy in the full cell and half cell before the onset of breakdown is 0.91 and 0.40 J respectively. The calculated energy absorbed by the explosive emission current is 0.78 J in the full cell and 0.39 J in the half cell. The simulation of multiple-breakdown events is more complex and a second detuning to the half cell after the onset of the second EEE is introduced as discussed before. The upper shift is set to 1.3 MHz and the simulation shows satisfying agreement with experiment, as shown in Fig. 2.23b, d.

2.5.4.3 Spontaneous rf Breakdown

Although the occurrence location of spontaneous rf breakdown is uncontrollable, it's still likely to be on the cathode where the electric field is the highest in the S-band 1.6-cell photocathode rf gun. In simulation of spontaneous rf breakdown event, the time structure of the rf breakdown current and the evolution of frequency detuning are assumed to be same as in the laser-triggered ones for simplicity.

When the rf breakdown current magnitudes are 13 and 0 A, and the frequency shifts are 4.5 and 0.4 MHz for the half cell and full cell respectively, the simulation agrees well with the single-breakdown experiment result, as shown in Fig. 2.24a, b. Besides, a delay of ∼100 ns between the onset of rf breakdown and the collapse of

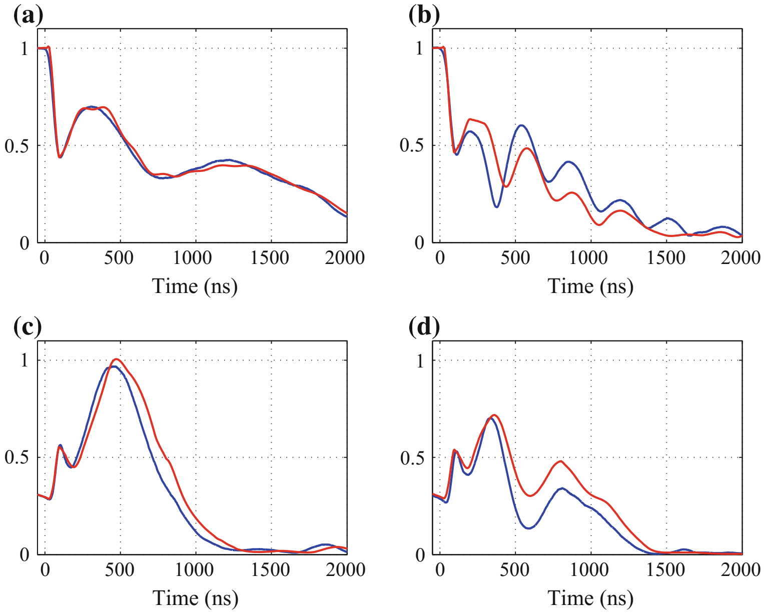

Fig. 2.23 Comparison of simulation (red) and experimental results (blue) of single-breakdown event (left) and multiple-breakdown event (right) with laser trigger. **a**–**b** Normalized pickup signal. **c**–**d** Normalized reflection signal

the fundamental mode can be clearly observed in simulation which is in accordance with the experiment results, as illustrated in Fig. 2.24c.

Due to its complexity, multiple-breakdown without laser trigger has not been simulated with the equivalent circuit model.

2.5.5 Discussion

Similarities in many aspects have been found between rf breakdowns with and without laser trigger, such as excitation of HOMs, frequency shift of the gun cavity after the onset of breakdown events, two types of breakdown events according to the detected charge pulses, etc.

Meanwhile, some noticeable differences exist between rf breakdowns with and without the laser trigger. For rf breakdowns without the laser trigger, the shape of the current is spiky and the captured charge is two orders of magnitude lower than that with the laser trigger. Besides, multiple-breakdown type dominates the spontaneous rf breakdown events while it’s rare in laser-triggered ones. What’s more, a delay of ∼100 ns between the onset of rf breakdown and the collapse of the fundamental mode can only be observed in spontaneous rf breakdown events.

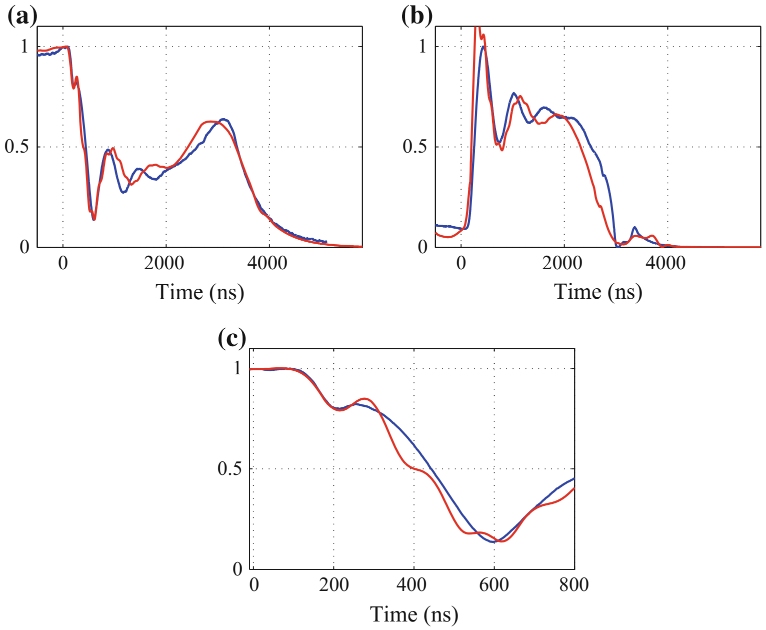

Fig. 2.24 Comparison of simulation (red) and experimental results (blue) of single-breakdown event without laser trigger. **a** Normalized pickup signal. **b** Normalized reflection signal. **c** Zoom-in view around the onset of rf breakdown in (**a**)

With the equivalent circuit model, most observations in both spontaneous and laser-triggered rf breakdowns can be reproduced. The most remarkable difference in circuit parameters between these two events is the rf breakdown current in two cells. In spontaneous rf breakdown events, the rf breakdown current in the half cell is significantly higher than that in the full cell. However, the rf breakdown currents in both cells are identical in the laser-triggered cases.

The physics of the current setting is believed to be ascribed to the EEE location on the cathode center. In laser-triggered rf breakdown events, it was near the cathode center as controlled by the high intensity laser. Therefore, the emission electrons could easily pass through the iris and absorb the stored energy in both cells with negligible delay, as illustrated in Fig. 2.25a.

On the other hand, in spontaneous rf breakdown events, the EEE location might be away from the cathode, causing emission electrons blocked by the iris. As a result, the emission electrons could only absorb the stored energy in the half cell. The severe imbalance of stored energy could lead to power flow from the full cell to the half one and following oscillation, as illustrated in Fig. 2.25b. The power flow moves at the group velocity of the gun, which matches the ∼100 ns delay between the collapse of the rf field in the full cell and the onset of the rf breakdown. Due to the power flow from the full cell, the stored energy in the half cell would recover to ∼75 % of its

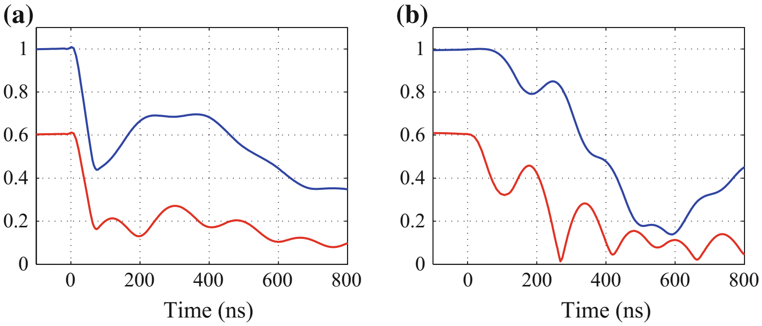

Fig. 2.25 Evolution of the rf field in the full cell (blue) and the half cell (red) after the onset of rf breakdown. **a** Laser-triggered rf breakdown; **b** Spontaneous rf breakdown

initial valve before the onset of rf breakdown in ∼200 ns. Since there is still plasma in the half cell, the recovered energy is likely to trigger a second rf breakdown.

Generally speaking, when an rf breakdown occurs in a traveling-wave structure, a significant portion of the power flow will be absorbed inside the structure, which will in turn cause severe damage. However, in standing-wave structures, most of the input power will be reflected, leading to less consequential damage. Among various X-band high-gradient structures tested by CERN, SLAC, and KEK, the standing-wave single-cell structures are proved to have lower BDR, compared with traveling-wave multi-cell structures [25]. In the experiment, multiple-breakdowns within one rf pulse are studied both in experiment and with the equivalent circuit model. The results suggest the second rf breakdown is caused by the power flow from another cell into the cell where the first breakdown occurred. This observation implies that in multi-cell standing-wave structures, subsequent breakdowns within one rf pulse can be triggered after the first one takes place even when the input power is fully reflected. To avoid this phenomenon as well as its damage, accelerating cells need to be separated from each other. Based on individually rf feeding structures shown in Fig. 2.26 [25, 26], it is possible to design such a standing-wave structure with zero coupling between cells by reducing iris size or increasing iris thickness.

Apart from providing a new understanding on the influence of power flow in rf breakdown, the experiment also confirms that intense laser assists the plasma formation on the cathode surface at a time and location corresponding to the presence of a large electric field, which eventually caused rf breakdown. It suggests that rf breakdown which limits the high gradient operation of this photocathode rf gun may occur predominately in high electric field region at the surface. In future experiments, the laser could also be directed to a high magnetic field or high power flow region in other photoinjectors to study additional rf breakdown phenomena in a more controllable way.

Laser triggering is also a more flexible method as the breakdown rate can be very high with intense laser. As a result, much time can be saved when obtaining a large amount of breakdown data and the path of experiments may be expedited.

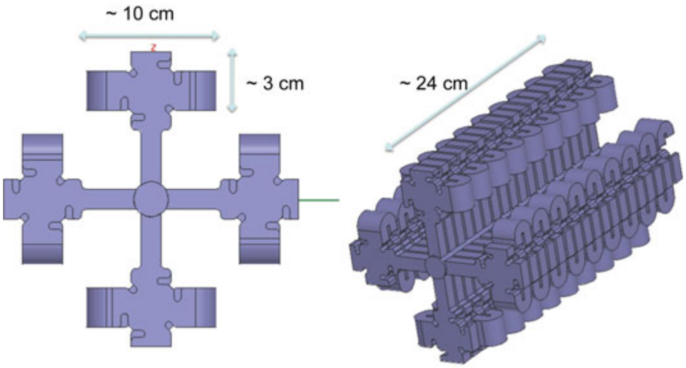

Fig. 2.26 Single-feed standing-wave multi-cell structure

2.6 Summary

In summary, it is demonstrated that rf breakdown in the photocathode rf gun can be triggered by an intense laser pulse at predictable locations and moments. The time evolution of electron emission at the nanosecond scale after the onset of breakdown has been observed and analyzed. Comparison between rf breakdowns with and without laser triggering shows that the laser trigger can serve as a more controllable and flexible method for breakdown study. The experiment reveals that multiple-breakdown can be triggered by the power flow between cells after the initial EEE, which implies standing-wave structures with separated cells may be more favorable for high gradient accelerators.

The laser-triggered rf breakdown experiment and its analysis has been published in Phys. Rev. ST Accel. Beams 17, 072002 (2014) [27].

References

1. Mesyats G (1983) Explosive processes on the cathode in a vacuum discharge. Trans IEEE. Electr Insul 18:218–225
2. Fursey G (1985) Field emission and vacuum breakdown. Trans IEEE. Electr Insul 20:659–670
3. Wang JW, Loew GA (1997) Field emission and rf breakdown in high-gradient room-temperature linac structures. Technical Report SLAC-PUB-7684, SLAC
4. Wuensch W (2002) High-gradient breakdown in normal-conducting rf cavities. In: Proceedings of EPAC2002, Paris, France
5. Qian H (2012) Research on the Emittance Issues of Photocathode RF Gun. Ph.D. thesis, Tsinghua University (2012)
6. Chicbkov B, Momma C, Nolte S et al (1996) Femtosecond, picosecond and nanosecond laser ablation of solids. Appl Phys A 63:109–115
7. Momma C, Chichkov B, Nolte S et al (1996) Short-pulse laser ablation of solid targets. Opt Commun 129:134–142

8. Nolte S, Momma C, Jacobs H et al (1997) Ablation of metals by ultrashort laser pulses. J Opt Soc Am B 4:10
9. Liu X, Du D, Mourou G (1997) Laser ablation and micromachining with ultrashort laser pulses. IEEE J Quantum Electron 33:10
10. Wang X, Tsang T, Kirk H et al (1992) Intense electron emission due to picosecond laserproduced plasmas in high gradient electric fields. J Appl Phys 72:888–894
11. Li R (2010) Theoretical and Experimental Investigations of Megaelectron Volt Ultrafast Electron Diffraction. Ph.D. thesis, Tsinghua University
12. Preuss S, Demchuk A, Stuke M (1995) Sub-picosecond UV laser ablation of metals. Appl Phys A 61:33–37
13. Fontenla A (2015) Post-Mortem analysis: SEM imaging review. In: Proceedings of MeVArc2015, Lapland, Finland
14. Schäfer C, Urbassek H, Zhigilei L (2002) Metal ablation by picosecond laser pulses: A hybrid simulation. Phys Rev B 66:115404
15. Häkkinen H, Landman U (1993) Superheating, melting, and annealing of copper surfaces. Phys Rev Lett 71:1023
16. Litvinov E, Mesyats G, Proskurovskiĭ D, (1983) Field emission and explosive electron emission processes in vacuum discharges. Sov Phys Usp 26:138
17. Young L (1996) Parmela. Technical Report LA-UR-96-1835, Los Alamos National Laboratory
18. Gao F (2009) High-power radio frequency pulse generation and extraction based on wakefield excited by an intense charged particle beam in dielectric-loaded waveguides. Ph.D. thesis, Argonne National Laboratory
19. CST (2010) CST MICROWAVE STUDIO
20. Drachman B (1984) Two methods to deconvolve: L1-method using simplex algorithm and L2-method using least squares and a parameter. IEEE Trans. Antennas Propag. 32(3)
21. Zheng S (2000) Research on backward traveling wave accelerating structures. Ph.D. thesis, Tsinghua University
22. Wang F, Adolphsen C (2009) Localization of rf breakdowns in a standing wave cavity. Phys Rev ST Accel Beams 12:042001
23. Johnson M, Ruber R, Ziemann V et al (2008) Arrival time measurements of ions accompanying rf breakdown. Nucl Instrum Methods Phys Res Sect A 595:568–571
24. Ziemann V (2007) The arrival-time spectrum of hot Coulomb explosions. Nucl Instrum Methods Phys Res Sect A 575:539–541
25. Neilson J, Tantawi S, Dolgashev V (2011) Update on design of standing-wave accelerator structure. In: proceedings of the 5th collaboration meeting on X-band accelerator structure design and test program, Tsukuba, Japan
26. Tantawi S (2006) rf distribution system for a set of standing-wave accelerator structures. Phys Rev ST Accel Beams 9:112001
27. Shao J, Chen H, Du Y et al (2014) Observation of temporal evolution following laser triggered rf breakdown in vacuum. Phys Rev ST Accel Beams 17:072002

Chapter 3
Experimental Research of Pin Cathode

Abstract Field emission from a solid metal surface, the precursor of rf breakdown, has been continuously studied for a century from macroscopic to atomic scales. However, many fundamental questions are yet to be answered, especially in rf case. Uncontrollable field emission position is one of the main barriers on the path to explore its nature. This chapter introduces a novel method to control the location of field emission and that of rf breakdown with a pin cathode. The study has been conducted on an L-band single-cell photocathode rf gun at the Argonne Wakefield Accelerator facility. The first part is to study the evolution of field emission during the rf conditioning period. The experimental results suggest there is an rf breakdown threshold of the maximum electric field on copper surface. The second part is to examine the localized field emission dependence on global parameters. The stored energy of the rf gun was changed by adjusting the longitudinal position (distance between the cathode base and the gun back surface) of the cathode while the applied electric field on the cathode tip was kept constant. A strong dependence of field emission on the stored energy has been observed which implies that under certain circumstances, a localized field emission may be significantly altered by the global parameters in a system.

3.1 L-Band Photocathode rf Gun Test Stand

The L-band high gradient photocathode rf gun test stand at AWA is shown in Fig. 3.1.

3.1.1 L-Band Photocathode rf Gun

3.1.1.1 Design and Cold Test

The L-band high gradient single-cell photocathode rf gun operates at 1.3 GHz, as illustrated in Fig. 3.2 [1]. The unique feature of the rf gun is its detachable cathode design which is ideal for testing cathodes with different shapes and materials in-situ

J. Shao, *Investigations on rf Breakdown Phenomenon in High Gradient Accelerating Structures*, Springer Theses, https://doi.org/10.1007/978-981-10-7926-9_3

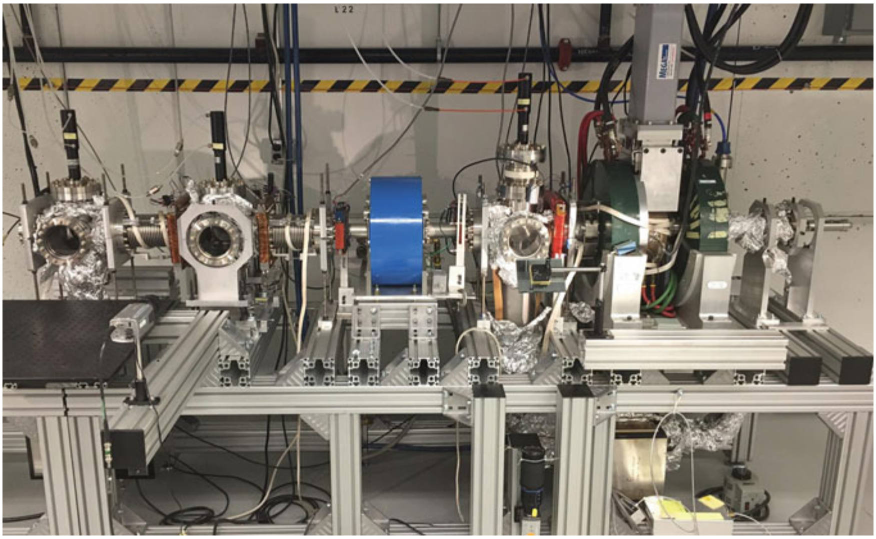

Fig. 3.1 L-band high gradient photocathode rf gun test stand at AWA

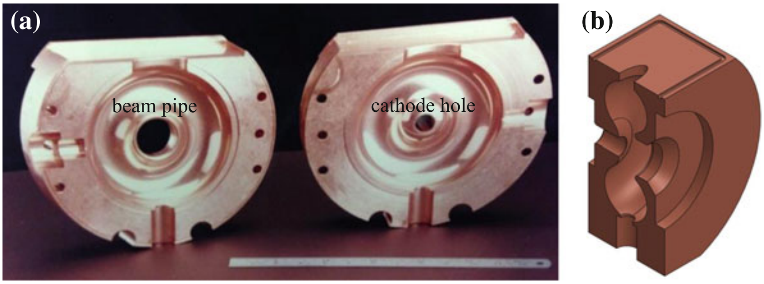

Fig. 3.2 L-band single-cell photocathode rf gun. **a** Components in fabrication; **b** Three-dimensional model

as well as examining the cathode condition with advanced surface analysis tools ex-situ.

The gun adopts nose design on both apertures for beam pipe and cathode insertion to achieve high electric field on the cathode with moderate input power. However, such design also causes a problem: the electric field on the cathode hole edge and the beam pipe edge is even higher than the cathode when a conventional flat cathode is installed. Therefore, field emission and rf breakdowns are most likely to occur on these surfaces instead of on the cathode itself with uncontrollable location. This will not only lead to severe damage of the rf gun but also cause difficulties when studying the cathode behavior both in-situ and ex-situ.

To confine field emission and rf breakdown to the cathode, it's necessary to enhance its electric field. Therefore, pin cathodes designed by SLAC, as shown in Fig. 3.3, have been applied in the study.

The pin cathode is made of oxygen-free copper. It consists of a Φ20 mm base and a 20 mm long detachable cone-shaped pin which are assembled by thread. The bottom diameter of the pin is 1.5 mm and the top is rounded as a Φ1 mm hemisphere. The pins were machined and electropolished by SLAC. The base was fabricated by the Accelerator Laboratory at Tsinghua University.

Electrical contact between the cathode and the cavity is ensured by a spring located ~5.5 mm behind the cathode base. The low field at the ~0.03 mm gap leads to negligible field emission from this area.

The cathode recess, as shown in Fig. 3.4, is adjusted by a micrometer. The longitudinal position of the cathode inside the cavity is measured by the micrometer and confirmed by direct measurement with a long stick inserted at the gun exit. The maximum error of the cathode position measurement is ~0.1 mm which is acceptable in the study.

The cathode displacement introduces frequency detuning to the rf gun. As energy density of electric field is higher than the magnetic field near the cavity axis, the frequency is downshifted when the pin cathode is pushed forward into the cavity. In the cold test prior to the experiment, the frequency detuning with different cathode longitudinal positions is illustrated in Fig. 3.5.

Fig. 3.3 Pin cathodes from SLAC

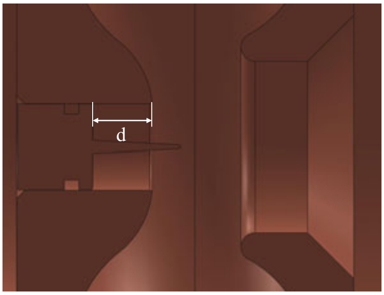

Fig. 3.4 Longitudinal position of the pin cathode in the gun. $d < 0$ indicates the cathode is behind its flush position with the cathode hole edge

Fig. 3.5 The frequency detuning of rf gun as a function of cathode longitudinal position

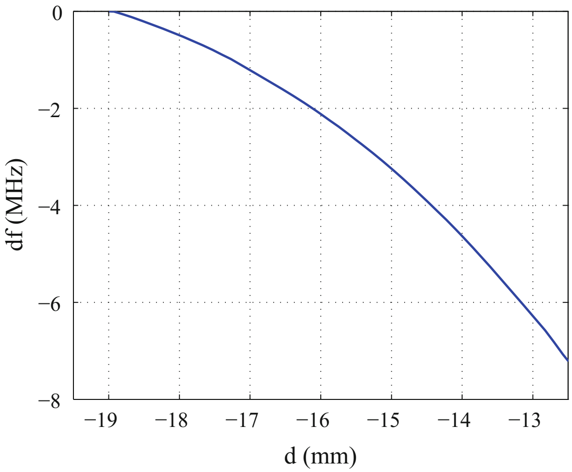

Fig. 3.6 The frequency detuning of rf gun as a function of tuner position. The zero position indicates the shaft has been fully recessed from the gun

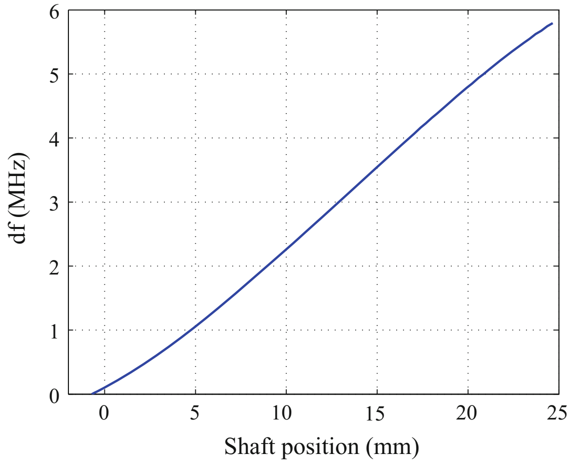

The detuning of the gun by the cathode displacement can be compensated by a Φ15.6 mm tuner at the side of the gun. Its position is controlled by another 25.4 mm travel micrometer. In the cold test, the frequency detuning of gun at different tuning shaft positions is illustrated in Fig. 3.6. The range of frequency tuning is ~6 MHz which limited the cathode position to be from –19 to –13 mm.

Within such range, the gun has been tuned at six cathode positions for the high power test, as listed in Table. 3.1.

The rf gun is cooled by water with 1° precision. The resulted fluctuation in frequency is ~20 kHz which is acceptable in the study.

Table 3.1 Cold test results of the L-band photocathode rf gun with different cathode positions

No.	Cathode position (mm)	Tuner position (mm)	Q_0	β_{ext}[a]
1	–18.87	–0.71	13730	1.47
2	–18.42	0.82	13765	1.46
3	–17.88	2.53	13615	1.45
4	–16.98	5.53	13518	1.43
5	–15.37	11.88	13271	1.41
6	–13.69	21.03	12847	1.36

[a] Coupling between the rf gun and the waveguide

3.1.1.2 Cavity Simulation

The electromagnetic simulation of the cavity has been done in two-dimension with the Superfish code [2] and in three-dimension with the Omega3P code [3]. The results of the two simulations are consistent with each other. The two-dimensional model used in Superfish is shown in Fig. 3.7.

When the cathode is at position No.1 in Table. 3.1, the electromagnetic field distribution along the contour is illustrated in Fig. 3.8. The three peaks in the electric field distribution correspond to the pin cathode tip (E_{tip}), the cathode hole edge (E_{edge}) and the beam pipe edge (E_{pipe}), respectively. The low magnetic field on the tip leads to negligible pulse heating in the experiment.

The ratios of E_{tip} to E_{edge} and E_{tip} to E_{pipe} at different cathode positions are illustrated in Fig. 3.9. In the adjustable range of the pin cathode longitudinal position, the electric field on the tip is significantly higher than that of the other two. Consequently, both field emission and rf breakdown are expected to be dominated by the tip in the high power test.

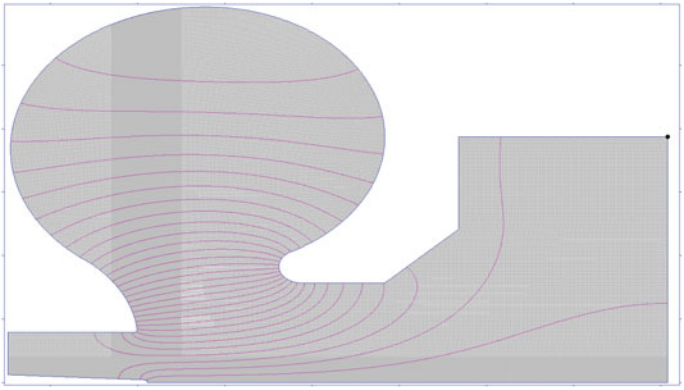

Fig. 3.7 Two-dimensional model of the L-band single-cell rf gun with the pin cathode. Local mesh density around the pin has been increased to improve accuracy. The magenta lines indicate the electric field

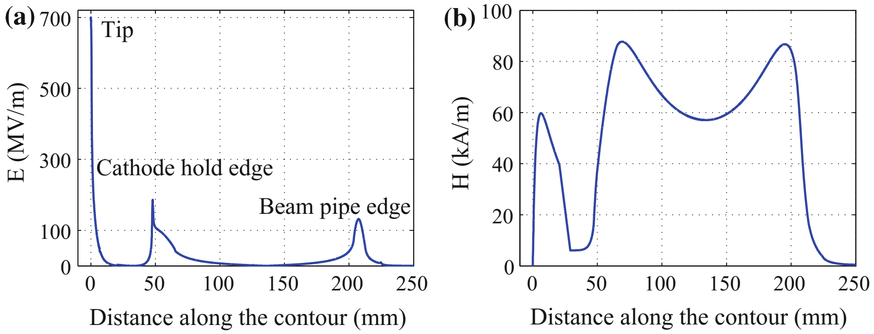

Fig. 3.8 Electromagnetic field along the cavity surface contour (start from the pin). **a** Electric field; **b** Magnetic field

Fig. 3.9 The ratio of E_{tip} to E_{edge} (blue) and E_{tip} to E_{pipe} (red) as a function of the pin cathode longitudinal position

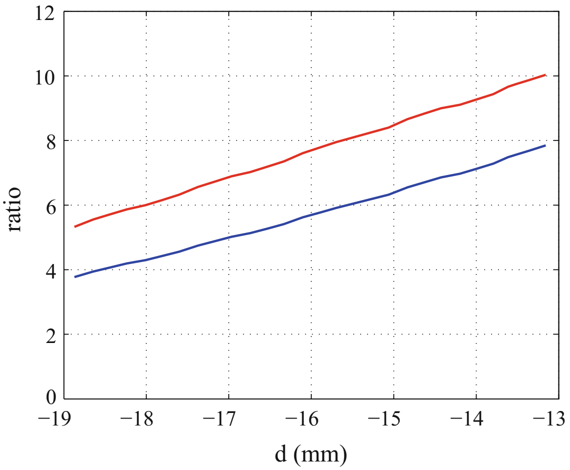

When the cathode is pushed further into the rf gun, the electric field on the cathode tip is enhanced so lower stored energy and input power are needed to maintain a constant E_{tip} as illustrated in Fig. 3.10.

3.1.2 Test Stand

The layout of the L-band high gradient photocathode rf gun test stand at AWA is shown in Fig. 3.11. The test stand is powered by a 25 MW klystron. Two solenoids with opposite current (the green ones in Fig. 3.11) installed around the gun are used to cancel the magnetic field on the cathode and to focus the beam.

Fig. 3.10 Stored energy inside the cavity and input power for the same E_{tip} (625 MV/m) at different cathode positions. The red squares indicate the six cathode positions listed in Table. 3.1

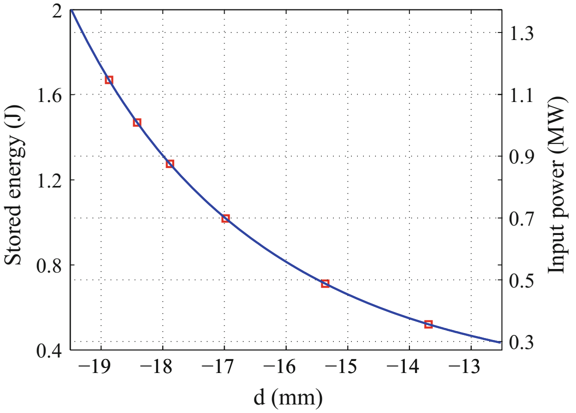

Fig. 3.11 Layout of the L-band photocathode rf gun test stand at AWA

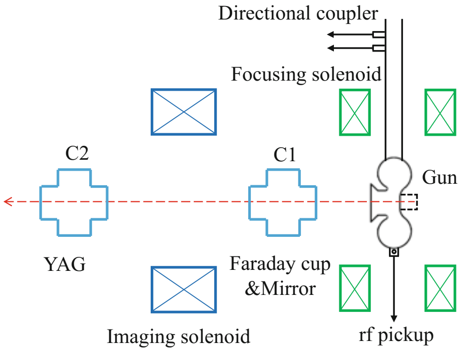

Diagnostics involved in the experiment are a bidirectional coupler to monitor the input and reflected rf signals, an antenna (pickup) to monitor the rf signal inside the cavity, a Faraday cup located at the gun exit to measure the field emission and rf breakdown current, and a yttrium-aluminum-garnet (YAG) screen to locate field emitters on the cathode with low resolution.

The aluminum Faraday cup is placed 45° to the beam with a silicon mirror, as shown in Fig. 3.12. The mirror is used to guide cathode installation as well as to detect rf breakdown location in-situ with the accompanying flash [4].

Due to the low amplitude of field emission current, an integral circuit is attached to the Faraday to improve its sensitivity, as illustrated in Fig. 3.13. In the circuit, L_c and C_c denote the distributed inductance and capacitance of the cable connecting the Faraday cup and the oscilloscope, R_L denotes the impedance of the oscilloscope. With $R_L = 1\mathrm{M}\Omega$ used in the high power test, the time constant of the circuit is 4.75 ms. Assuming the duration of field emission current is 5 μs, the minimal detectable charge and current by the Faraday cup is 100 pC and 20 nA, respectively.

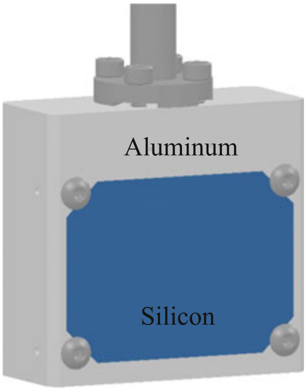

Fig. 3.12 Three-dimensional model of the Faraday cup assembly

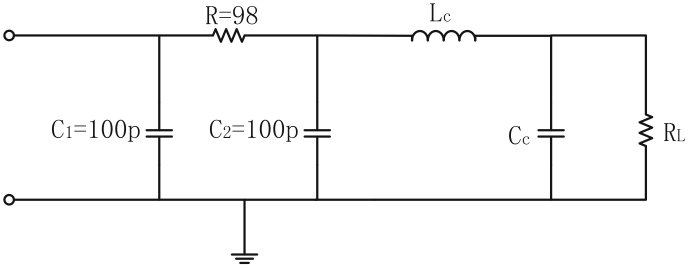

Fig. 3.13 Integral circuit of the Faraday cup

The test stand is interlocked by vacuum gauges and X-ray detectors to prevent continuous rf breakdowns in the high power test [4].

3.2 Evolution of Field Emission During rf Conditioning

In newly-built accelerating structures, the designed gradient could not be achieved by increasing the input rf power rapidly [4, 5]. Instead, it needs to go through a slow procedure called rf conditioning in which the input power and the pulse length are gradually raised. The number of rf pulses required in this period can be hundreds of thousands, depending on the target gradient and conditioning strategy. The latest research by CERN shows that the maximum achievable gradient is determined by the number of total rf pulses rather than rf breakdown events during the rf conditioning period [5]. The research result indicates the surface condition is being continuously modified by every pulse in rf conditioning to sustain increasing gradient.

Because field emission current can be an indicator of surface condition, it's helpful to study emission parameters, including field enhancement factor β and effective emission area A_e, to understand the effect of rf conditioning on accelerating structures [6–8].

For conventional accelerating structures, the location of field emitters are uncontrollable thus emission current may not be effectively detected. This might lead to incorrect results when measuring field emission parameters. By using pin cathodes to precisely control the field emission and rf breakdown location, it is possible to systematically study the evolution of field emission during rf conditioning.

3.2.1 rf Conditioning of Pin Cathodes

Four identical pin cathodes, numbered ♯1, ♯2, ♯7, and ♯15, have been conditioned at the position No.1 listed in Table. 3.1. During the rf conditioning period, the focusing solenoid strength was set to zero. The rf breakdown rate was controlled to be $10^{-4}\sim10^{-3}$/pulse.

Figure 3.14(a–c) shows the typical recorded waveforms without rf breakdown. Only the fundamental mode 1.3 GHz could be detected in the spectrum, as illustrated in Fig. 3.14(d).

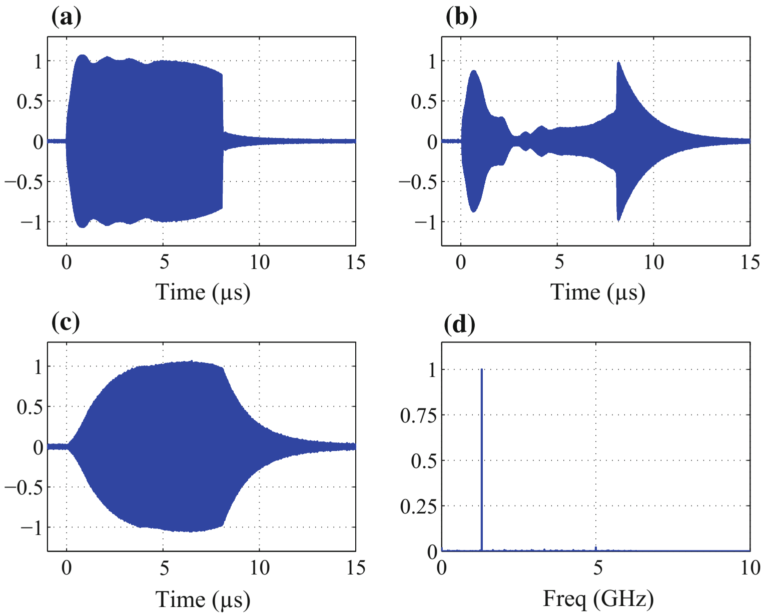

Fig. 3.14 Typical waveforms of normal operation without rf breakdown. **a** Normalized input wave; **b** Normalized reflected wave; **c** Normalized rf field inside the cavity; **d** Normalized spectrum of the rf field

Figure 3.15 shows the typical waveforms of rf breakdown event in which full reflection and rf field collapse can be clearly observed. No HOM has been detected in the spectrum which might result from the weak coupling of the rf pickup probe.

By monitoring the flash accompanying rf breakdown with the silicon mirror, most rf breakdown/EEE events were observed occurred at the tip where the electric field was the highest in the rf gun. A few rf breakdown/EEE events also occurred at the cathode hole edge, as illustrated in Fig. 3.16.

Automatic interlock system has only been applied when rf conditioning the ♯1 and the ♯2 pin cathode to pause the input power after detection of an rf breakdown event. For the ♯7 and the ♯15 pin cathode, the whole system was manually paused after several continuous rf breakdowns. After the pause, input power was lowered to certain level and gradually increased back if no more rf breakdown occurred in ∼1000 pulses.

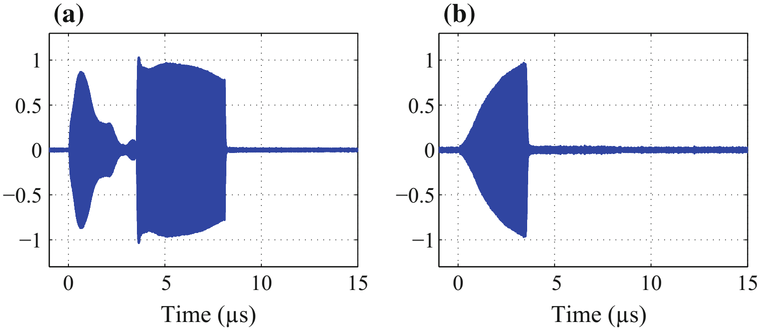

Fig. 3.15 Typical waveforms of rf breakdown event. **a** Normalized reflected wave; **b** Normalized rf field inside the cavity

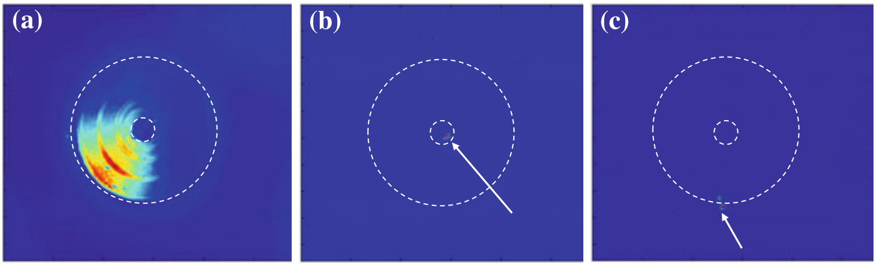

Fig. 3.16 Cathode images obtained by the silicon mirror. The outer and inner white dashed circuit denote the cathode hole edge and the tip, respectively. The arrows point to the rf breakdown/EEE location. **a** Room light on, the brightness was from light reflection on the mirror-like finishing cathode base; **b**, **c** Room light off, the brightness was from the flash accompanying rf breakdown. **b** rf breakdown/EEE occurred at the tip; **c** rf breakdown/EEE occurred at the cathode hole edge

Table 3.2 rf condition results of the pin cathodes

	♯1	♯2	♯7	♯15
Pulse length (μs)	8.0	8.0	8.0	5.5
Repetition (Hz)	10	10	10	2
Vacuum level (Torr)	$\sim 4 \times 10^{-9}$	$\sim 9 \times 10^{-9}$	$\sim 5 \times 10^{-9}$	$\sim 2 \times 10^{-9}$
Automatic interlock	Yes	Yes	No	No
Total pulses	~450000	~320000	~190000	~50000
Maximum input power (kW)	900	420	1310	1310
Maximum E_{tip} (MV/m)	580	395	700	700
Maximum E_{edge} (MV/m)	154	105	186	186
Maximum E_{pipe} (MV/m)	109	74	132	132

The rf condition results of the pin cathodes are listed in Table. 3.2. The maximum electric field on the tip is determined by an equivalent circuit model as introduced in Appendix.

3.2.2 Field Emission Measurement

In rf conditioning, the typical waveform of detected current by the Faraday cup with integral circuit is illustrated in Fig. 3.17. The rapid falling edge, at the order of microsecond, is determined by the field emission current during the rf pulse. The slow rising edge, at the order of millisecond, is governed by the time constant τ_{Faraday} of the integral circuit and follows

$$V(t) = V_{\min} \exp(-t/\tau_{\text{Faraday}}) \tag{3.1}$$

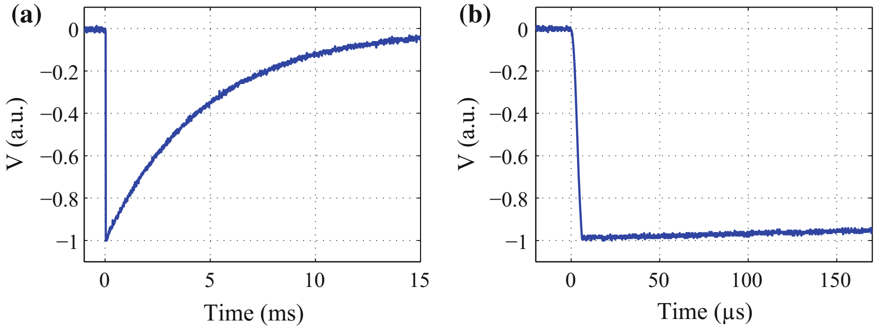

Fig. 3.17 Typical Faraday cup signal. **b** is the zoom-in view of **a** near $V_{\min}$

where $V_{\min}$ is the minimum of the Faraday cup signal.

Since the Faraday cup signal is several orders of magnitude longer than the input power signal, only part of the former one (around $V_{\min}$) could be recorded by the oscilloscope when taking the two signals together. The total charge of the detected current can be derived as

$$C = -\frac{V_{\min}\tau_{\text{Faraday}}}{R_{\text{L}}} \tag{3.2}$$

where R_{L} is the impedance of the oscilloscope.

During the rf conditioning period, rf breakdown occasionally occurred and the BDR was controlled to be 10^{-4} to 10^{-3}/pulse. The field emission parameters, including field enhancement factor β and effective emission area A_{e}, have been measured during the peace period between rf breakdown events. To measure the field emission parameters, the input power was gradually lowered from the maximum conditioned value and the corresponding field emission current at each power level was recorded synchronously, as illustrated in Fig. 3.18(a). Then, the data was plotted in the F-N coordinate and linearly fitted, as illustrated in Fig. 3.18(b). From the fitting, the field emission parameters could be derived according to Eq. 1.13. Generally, each measurement took ~300 rf pulses.

As the input power was gradually increased and more rf pulses were accumulated during the rf conditioning period, the field emission current at a fixed E_{tip} has been observed to decrease which suggests a continuous surface condition evolution. For example, Fig. 3.19 shows the field emission current measurement results when E_{tip} was conditioned to 360, 500, 610, and 700 MV/m.

Figure 3.20 shows the evolution of the emission parameters of the ♯7 pin cathode during the rf conditioning period. Despite small fluctuation, the trends are clear. When E_{tip} was conditioned from 200 to 700 MV/m, β decreased from ~60 to ~20, A_{e} increased from 10^2 to 10^3–10^4 nm^2, and the maximum local electric field on the tip $\beta \cdot E_{\text{tip}}$ maintained around 11.4 GV/m.

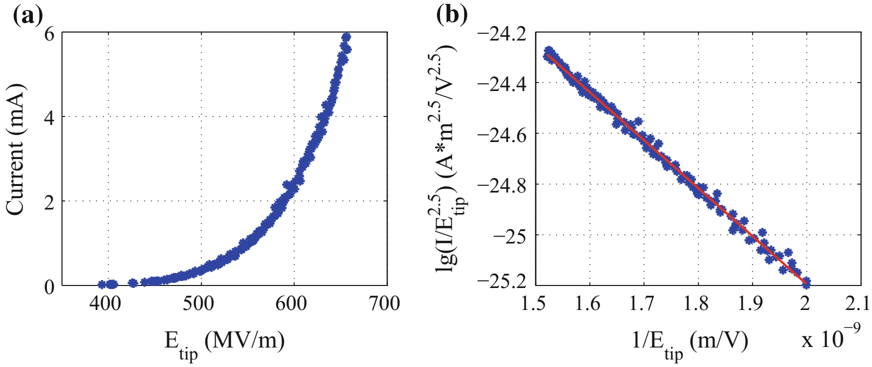

Fig. 3.18 Field emission current as a function of E_{tip}. **a** Normal coordinate; **b** F-N coordinate, the blue dots and the red line denote the original data points and the linear fitting, respectively

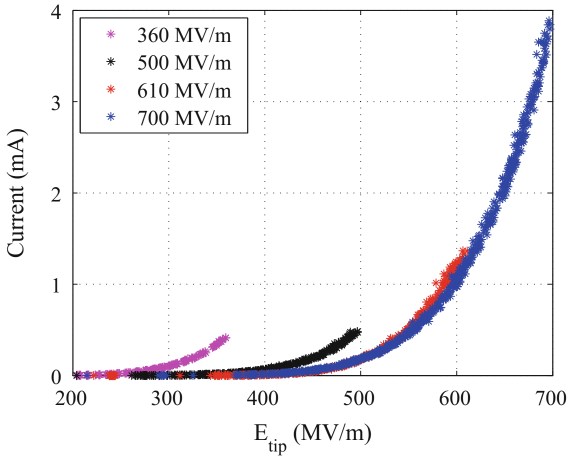

Fig. 3.19 Field emission current as a function of E_{tip} at different rf conditioning stages

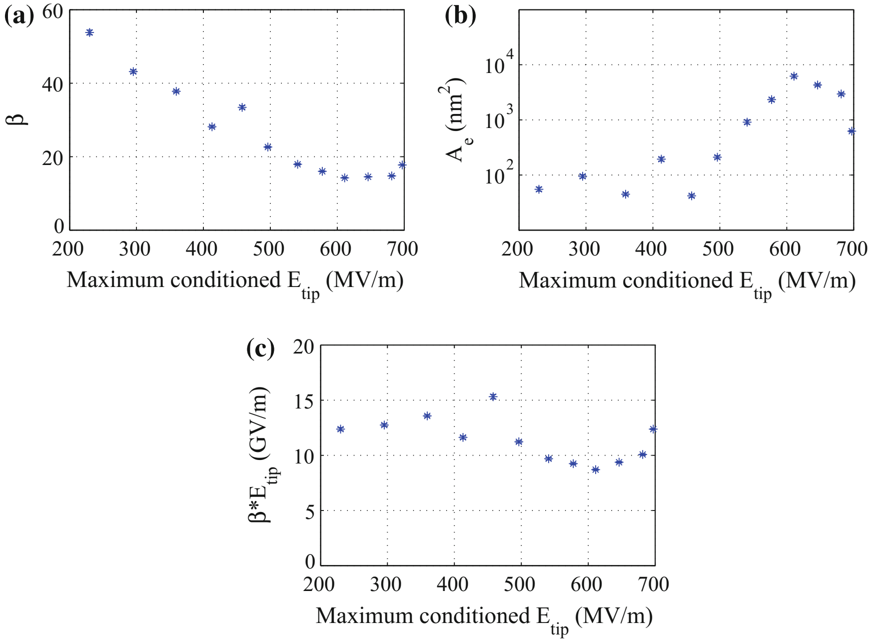

Fig. 3.20 The evolution of field emission parameters during rf conditioning period. **a** β; **b** A_{e}; **c** $\beta \cdot E_{\mathrm{tip}}$

3.2.3 Surface Examination

The surface condition has been examined by SEM before and after the high power test.

Figure 3.21 shows the SEM images of the ♯7 pin prior to the high power test. No leftover features from turning could be detected after the electropolishing procedure. The different colors on the surface, as shown in Fig. 3.21(b, c), might be caused by chemical residue during the cleaning process. Several scratches, as shown in Fig. 3.21(d), were found on the surface which might be caused by handling. The overall surface condition was very smooth and no feature with high aspect ratio which would cause high field enhancement factor was found.

Figure 3.22 shows the SEM images of the ♯7 pin after the high power test, which are remarkably different from the ones in Fig. 3.21. Hundreds of rf breakdown spots which contain craters from melting and recrystallization can be found on the surface

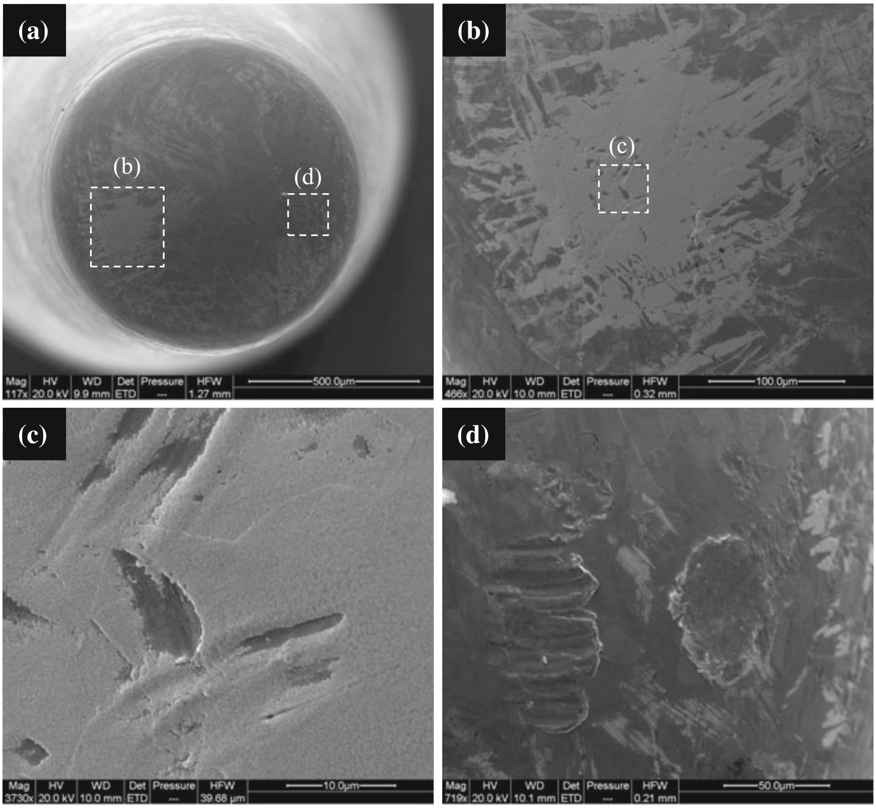

Fig. 3.21 SEM images of the ♯7 pin prior to the high power test. **a** The whole tip; **b**, **c** Possible chemical residue; **d** Scratches

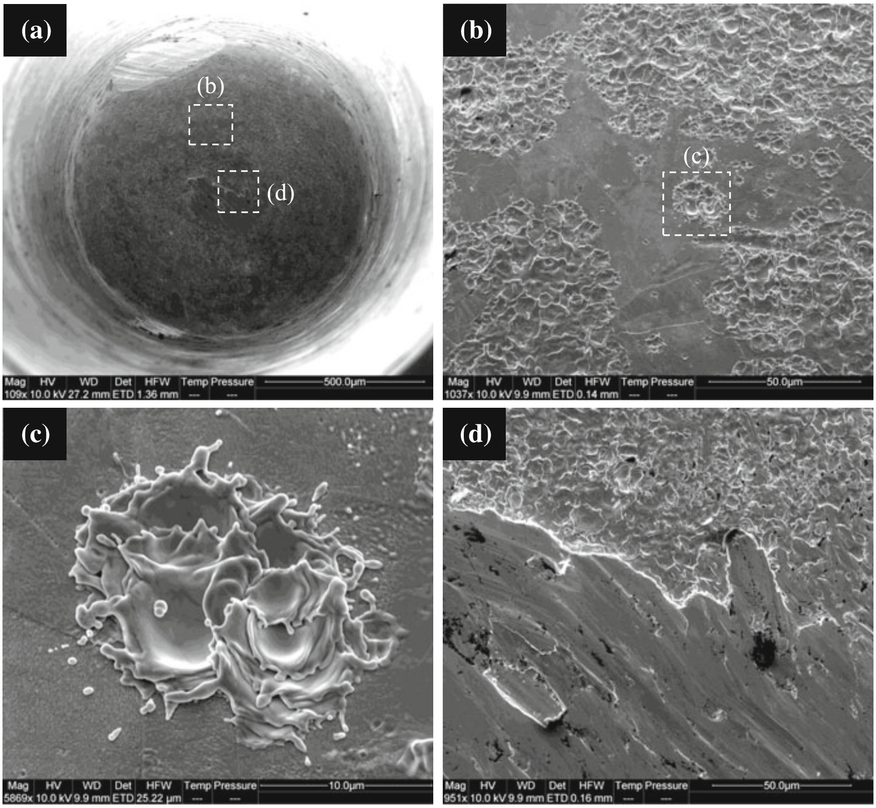

Fig. 3.22 SEM images of the ♯7 pin after the high power test. **a** The whole tip; **b**, **c** rf breakdown spots; **d** Scratches

either separately or in clusters, as shown in Fig. 3.22(b, c). The typical spot size is at the order of square micrometer, which is significantly larger than the fitted value by the F-N equation. Therefore, field emission electrons might be dominated by tiny features with high aspect ratio within the breakdown spots, rather than emit uniformly from them. The scratches shown in Fig. 3.22(d) were caused during the cathode disassembling process after the high power test.

3.2.4 Discussion

The macroscopic electric field on the pin cathodes is remarkably higher than previous rf or dc studies [8–11]. In various X-band accelerating structures high power tests, the maximum macroscopic surface field obtained is around 300 MV/m with a pulse length of 160 ns and BDR of 10^{-6}/pulse [11]. In the high power test of pin cathodes, 700 MV/m macroscopic electric field has been achieved with a pulse length of several μs and BDR lower than 10^{-3}/pulse. The significant improvement might be a result of the low surface pulse heating at the tip (2 K comparing with 20–50 K in X-band structures [12]).

The maximum electric field on the tip $\beta \cdot E_{\mathrm{tip}}$ maintained to be around 11.4 GV/m with small fluctuation during the entire rf conditioning period despite the rise of E_{tip} by a factor of 3.5. When the localized electric field exceeds the order of 10 GV/m, previous theoretical study with Particle-In-Cell (PIC) simulation predicts surface failure which would lead to breakdown [13]. Several dc tests with macroscopic electric field limited to 200 MV/m also show a breakdown threshold around 10 GV/m on copper surface [8, 10]. The results with pin cathode presented here support this hypothesis of surface failure/breakdown threshold, but in a wider range with macroscopic electric field up to 700 MV/m.

From the evolution of field emission parameters during the rf conditioning period, a strong correlation between A_{e} and β could be observed, as illustrated in Fig. 3.23. It indicates the surface condition was continuously modified under high electric field. Due to the surface failure or breakdown threshold of the surface, emitters with high field enhancement factors would be destroyed by rf breakdown when the electric field was being gradually increased. The increasing effective emission area may suggest an initially sharp emitter would develop into smoother ones with larger surface area during rf conditioning.

In addition to the field emission parameters evolution from F-N measurement, the surface condition can also be vividly compared before and after the high power test by SEM images. From the measurement results in Fig. 3.23, it's surprising that the smooth surface prior to high power test has a much higher field enhancement factor than the damaged surface with hundreds of rf breakdown spots afterwards. This may suggest the field enhancement factor might not be solely determined by geometry, but also by other factors like low work function area. It may also indicate there were

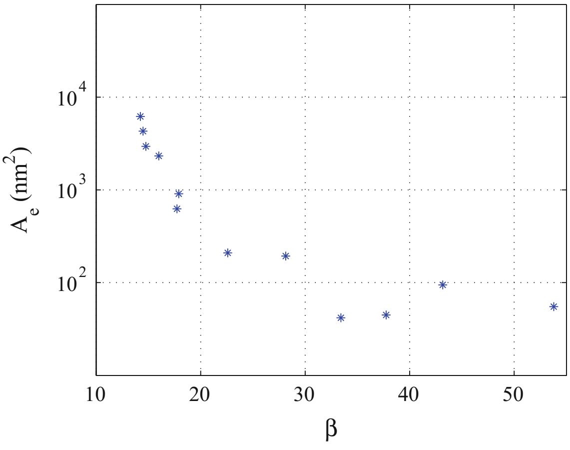

Fig. 3.23 The correlation between A_{e} and β during rf conditioning. The evolution trends to be from right to left with fluctuation

tiny emitters beyond the resolution of SEM (∼nanometer) on the initial surface. Investigation with higher resolution instruments, such as atomic force microscopy, will be applied in future study.

3.3 Field Emission Dependence on Stored Energy

Usually, when applying the F-N equation (Eq. 1.12) in high gradient accelerating structure research, only the fundamental mode is considered in the electric field term. Recently with theoretical and PIC simulation study, researches from SLAC have proposed a hypothesis that HOMs excited from the emission current would change the total surface electric field as well as the following emission current [14]. In their research, the amplitude of the excited HOMs depends not only on localized field emission current, but also on global parameters such as frequency, group velocity, etc. Therefore, the localized field emission may be coupled to global parameters. If it's true, this hypothesis would deepen the current understanding of field emission phenomenon in high gradient rf accelerating structures, which might help to explain various contradictions between the F-N fitting results and surface condition observation, including extremely high field enhancement factor and unphysically low emission area. Pin cathodes have been applied in the following study to test the hypothesis with the high gradient L-band photocathode rf gun at AWA.

3.3.1 Field Emission Current Measurement

The input power and the stored energy to maintain the same E_{tip}, if only considering the fundamental mode, decrease when the pin is being pushing into the gun, as illustrated in Fig. 3.10. The frequency of the gun can be compensated by the turner. This feature will decouple the localized parameter (E_{tip}) and global ones (input power or stored energy) which is ideal to test the hypothesis.

The ♯7 and the ♯15 pin cathodes have been applied to measure the field emission current at different longitudinal positions, as listed in Table. 3.1. The ♯7 pin cathode has been tested at all six positions while the ♯15 pin cathode has been tested at four positions with high stored energy to confirm the measurement.

At each cathode position, the focusing solenoid strength B_{f} has been scanned in the experiment to ensure the emission current capture by the Faraday cup. The scanning has been performed from 0 to a maximum value of 1500 Gauss with a step of 125 Gauss. The input power has also been scanned in a procedure similar to that of the field emission parameters measurement in the rf condition period. Certain E_{tip} and corresponding emission current could then be derived from interpolation with high accuracy.

The field emission current largely depends on the surface condition. To avoid condition variation caused by rf breakdown, the E_{tip} was controlled to be lower than 660 MV/m in this study after being conditioned to 700 MV/m. At each cathode position, the measurement typically lasted for 7000 rf pulses when both B_f and the input power were scanned. At the end of measurement of each cathode position, field emssion with several selected settings of B_f and input power has been remeasured to ensure the surface condition has not changed due to accumulated rf pulses, as illustrated in Fig. 3.24.

When B_f was high, additional falling edge after the rf pulse could be observed in the Faraday cup signal, as illustrated in Fig. 3.25.

The amplitude of the additional falling edge almost remained constant when the input power varied, as illustrated in Fig. 3.26(a). It's likely to be caused by the multipacting effect described as following [15–18]. In rf structures, field emission from a surface (A) could hit back or arrive at another surface (B). A number of secondary

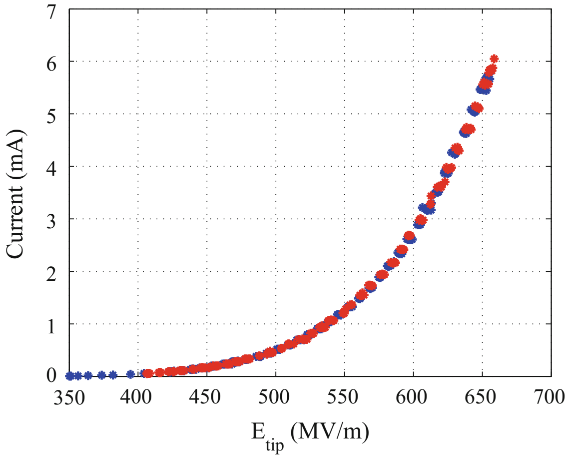

Fig. 3.24 Field emission current as a function of E_tip at the beginning (blue) and the end (red) of the test

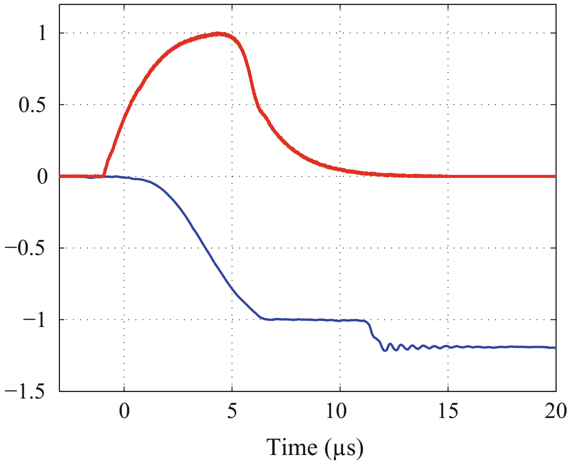

Fig. 3.25 The Faraday cup signal (blue) with high B_f. The red line denotes the normalized envelope of the rf field inside the gun for reference

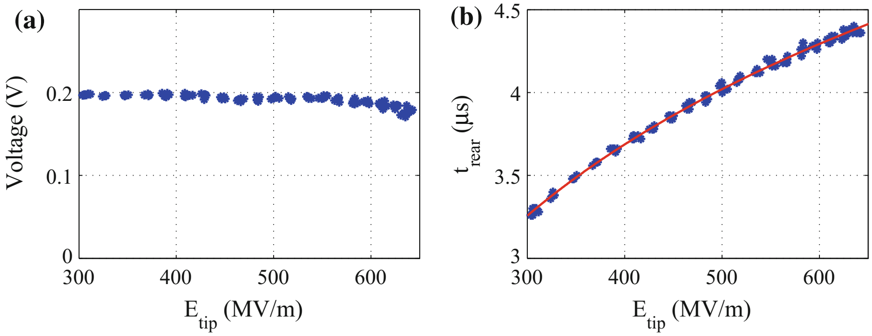

Fig. 3.26 The behavior of the additional falling edge as a function of E_{tip}. **a** Amplitude; **b** t_{rear}, the blue dots and the red line denote the original date and the fitting by Eq. 3.3, respectively

electrons would yield, depending on the energy and angle of the incident electron. In certain circumstances, the generated electrons could travel back to surface A in half an rf period and generate even more secondary electrons. Therefore, resonance could be formed between surface A and B, resulting in a strong emission current. Multipacting phenomenon often occurs when the surface electric field is low and the secondary electron yield is high, such as during the rising and the falling time of an rf pulse. A previous study with rf guns has shown that multipacting effect is more likely to occur during the falling time when the resonance condition is easies to be satisfied [18]. Additionally, multipacting during both the rising and falling edge has also been observed when the input power is very low [18]. The study has also presented the delay between the occurrence of multipacting and the end of input power, which follows [18]

$$E_{\mathrm{MP}} = E_{\max} \exp(-t_{\mathrm{rear}}/\tau) \tag{3.3}$$

where $E_{\max}$ and E_{MP} denote the maximum electric field during the whole rf period and that when the maltipacting occurs, τ denotes the filling time of the standing-wave structure.

In the high power test, t_{rear} has been measured at different input power as illustrated in Fig. 3.26(b). According to Eq. 3.3, τ can be fitted as 1.48 µs. While from the cold test results listed in Table. 3.1, τ can be calculated as $\tau = 2Q_0/[(1+\beta_{\mathrm{ext}})\omega] = 1.36$ µs. The reasonable agreement confirms that the additional falling edge is caused by multipacting effect in the rf gun.

As the second falling edge caused by multipacting is quite distinguishable in the Faraday cup signal, it can be easily excluded in the following analysis. With certain B_{f}, the field emission current with different input power and cathode positions is illustrated in Fig. 3.27. In the F-N coordinate, the curves should be linear. However, when the cathode was at position 5 and 6, non-linearity could be observed at the low-end of the electric field. This might be caused by multipacting at the beginning

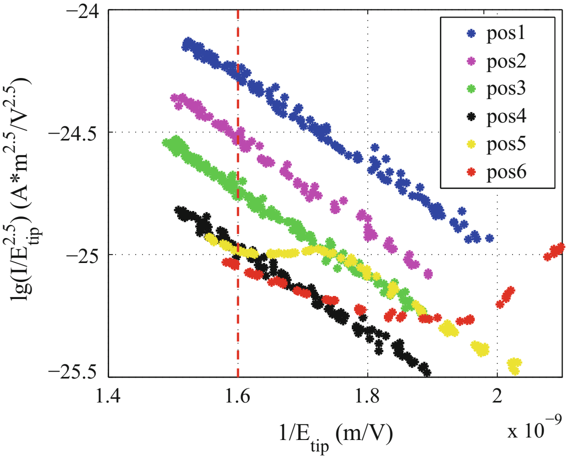

Fig. 3.27 With certain B_f, the detected current as a function of E_{tip} and the cathode position in the F-N coordinate. The red dashed line denotes $E_{tip} = 625$ MV/m

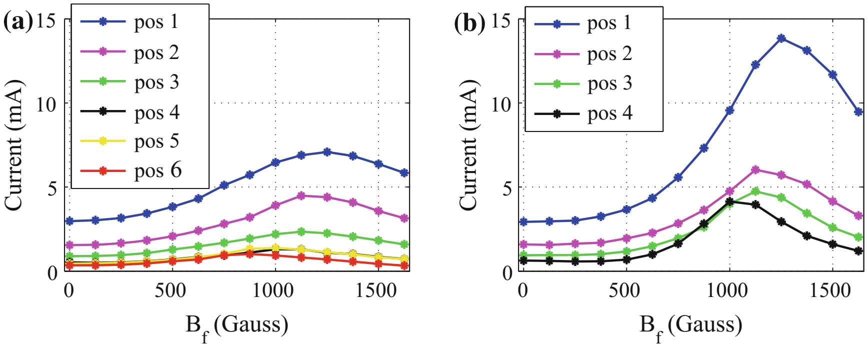

Fig. 3.28 The detected current by the Faraday cup as a function of B_f and cathode position. **a** The ♯7 pin cathode; **b** The ♯15 pin cathode

of the rf pulse when the input power was extremely low. The response of the Faraday cup is not fast enough to distinguish this current from the main field emission current. In order to eliminate this effect, the field emission current at high electric field of 625 MV/m is interpolated and compared in the following analysis.

When E_{tip} is fixed at 625 MV/m, the interpolation results with different focusing solenoid strength B_f and cathode positions are illustrated in Fig. 3.28. The captured current depends not only on the stored energy, but also on B_f due to the dynamics of field emission electrons in the rf gun.

3.3.2 Dynamics of Field Emission Current

The current detected by the Faraday cup I_{Fadaray} is determined by the field emission current I_{emit} and the capture ratio η as

$$I_{\text{Fadaray}} = \eta I_{\text{emit}} \tag{3.4}$$

To eliminate the influence of capture ratio on the detected current at different cathode positions, three-dimensional particle tracking code ASTRA [19] has been applied to study the dynamics of field emission electrons in the rf gun. Space charge effect has been ignored in the study [20, 21].

3.3.2.1 Parameters

Parameters such as the field distribution of the rf gun with different cathode positions, the geometry boundary of the beam line, and properties of the emitted electrons are required in the ASTRA simulation.

Field distribution
The field distribution of the rf gun with different cathode positions has been calculated by Superfish [2]. Local mesh density around the tip has been increased to improve accuracy, as shown in Fig. 3.7. A self-developed code has been applied to convert the field distribution into a three-dimensional one with denser step around the tip for ASTRA.

Geometry boundary
The geometry boundary condition is modified from the rf gun design, as shown in Fig. 3.29. The precise details of the pin cathode are maintained for dynamics simulation while the other surfaces of the gun are simplified.

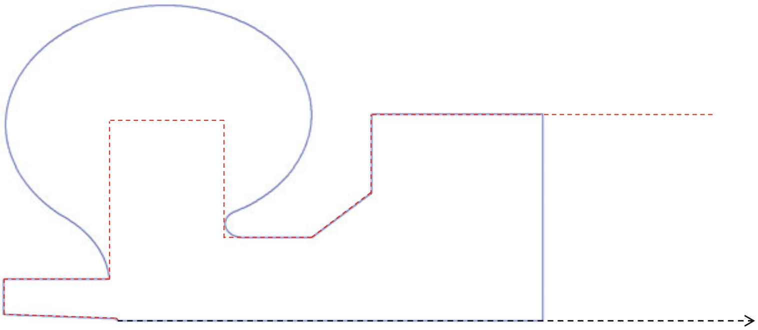

Fig. 3.29 Geometry boundary applied in dynamics simulation. The blue and the red line denote the original rf gun design and the simplified one used in ASTRA, respectively. The black dashed line denotes the z-axis of the beam line in simulation

Electron properties

The time structure of field emission current is determined by localized surface electric field during an rf period as

$$E(t) = E_{\max}\sin(\omega t) = E_{\max}\sin(\vartheta) \tag{3.5}$$

where $E_{\max} = E_{\mathrm{tip}} \times \beta$ is the maximum electric field after involving the field enhancement factor β, $\vartheta = \omega t$ is the emission phase. The amplitude of emission current depends on the emission phase based on the F-N equation, as illustrated in Fig. 3.30. For simplicity, the dependence can be approximated as a Gaussian distribution [22]. With given work function and frequency, the standard deviation of the Gaussian distribution is determined by $E_{\max}$. Its value nearly remains constant with an $E_{\max}$ range of 8–15 GV/m obtained in the study with pin cathodes. Therefore, the Gaussian distribution with a standard deviation of 20° is adopted in ASTRA simulation.

Because of the tunneling effect, the initial kinetic energy of field emission electrons is lower than that of photoemission or thermal emission ones. In ASTRA simulation, it has been set to 100 meV as reported in a previous study [23].

To determine the emission angle from the tip, a local coordinate has been set at the emitter, as shown in Fig. 3.31. The axis z_e is perpendicular to the surface while x_e and y_e are in its tangent plane with x_e pointing to the z-axis of the rf gun.

In the local coordinate, the emission angle is defined by θ and φ as shown in Fig. 3.31. θ denotes the angle between the emission electron momentum and the z_e axis, ranging from −90° to 90° (positive value indicates the projection of the momentum on x_e axis is positive and vice versa). φ denotes the angle between the velocity projection on the tangent plane and the x_e axis, ranging from 0° to 360°.

Figure 3.32 illustrates the capture ratio of electrons by the Faraday cup from a fixed emitter with different emission angles. The maximum variable range is deter-

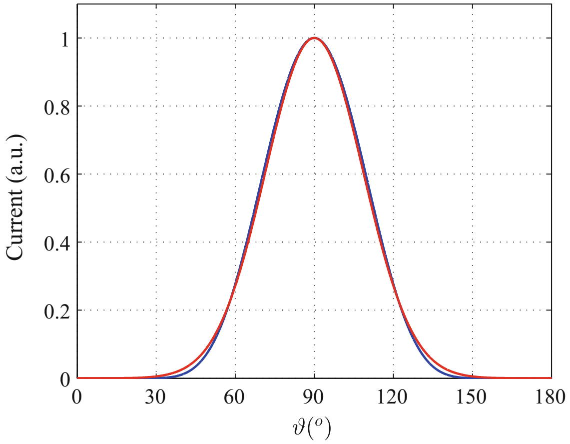

Fig. 3.30 The field emission current amplitude as a function of emission phase. The blue and the red line denote the original F-N equation calculation and the Gaussian fitting, respectively

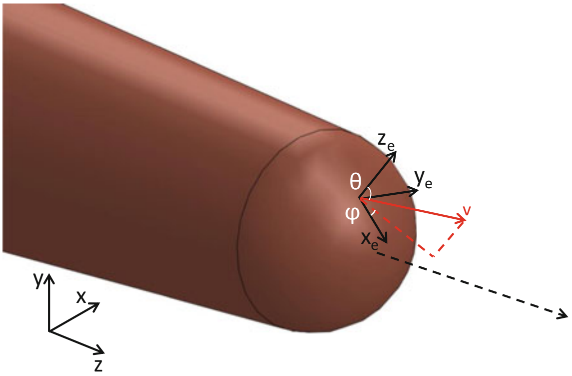

Fig. 3.31 Three-dimensional model of an emitter at the tip and the local coordinate

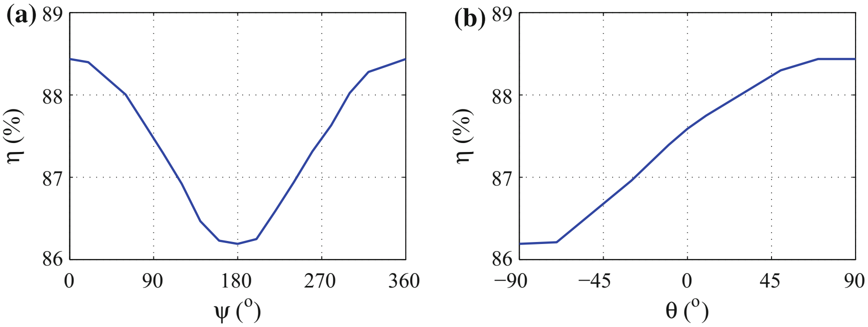

Fig. 3.32 The capture ratio of the Faraday cup as a function of emission angle. **a** Emission along the tangent plane; **b** Emission along the x_e-z_e plane

Fig. 3.33 Two-dimensional model of emitter at the tip and the local coordinate

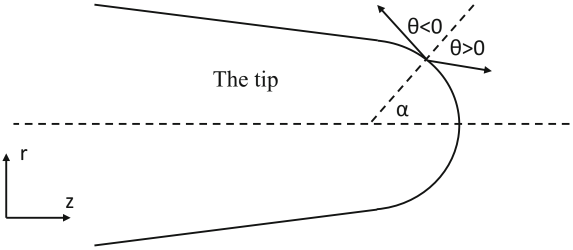

mined when electron is emitted along the tangent or x_e-z_e plane. Therefore, the three-dimensional model can be simplified to a two-dimensional one in z-r plane, as illustrated in Fig. 3.33. The emission position is defined by α (ranging from 0° to 90°) and the angle is defined by θ.

3.3.2.2 Results

Figure 3.34 illustrates a typical capture ratio dependence on emission position with fixed cathode position and focusing solenoid strength. The error bar results from different emission angles. Electrons close to the tip edge with large α could not be detected by the Faraday cup due to the lost on the geometry boundary of the rf gun and its following beam pipe.

Figure 3.35 illustrates the capture ratio dependence on cathode position and focusing solenoid strength. To obtain a simpler and clearer view, dependence of only cathode position No.1 and No.6 as listed in Table 3.1 is compared. From the simulation results, at B_f of 625 Gauss, the capture ratio dependence on emission position is nearly the same for both cathode positions No.1 and No.6, as illustrated in Fig. 3.35(d). With this solenoid strength, the difference of detected current, as illustrated in Fig. 3.28, is only determined by the emission current from the tip. Besides, the capture ratio at cathode position No.1 at $B_\mathrm{f} = 500$ Gauss is higher while at $B_\mathrm{f} = 750$ Gauss is lower than that at position No.6, respectively. Thus, the difference of detected current at these solenoid settings can be used as an error bar when comparing the emission current.

Similar results of the same capture ratio dependence on the emission position have also been found for other cathode positions, as listed in Table. 3.3.

3.3.2.3 Comparison of Field Emission Current

After excluding the influence of capture ratio on the measurement results by comparing the detected current at selected B_f values according to Table. 3.3, the dependence of field emission current on stored energy (cathode position) with the same E_tip is illustrate in Fig. 3.36. An enhancement of the field emission current by a factor of

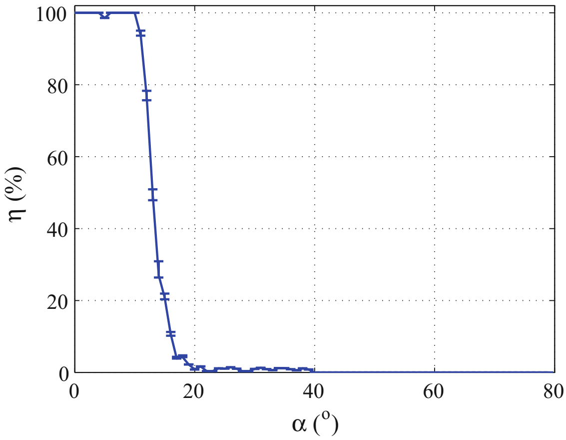

Fig. 3.34 The capture ratio of the Faraday as a function of electron emission position at fixed cathode position and focusing solenoid strength

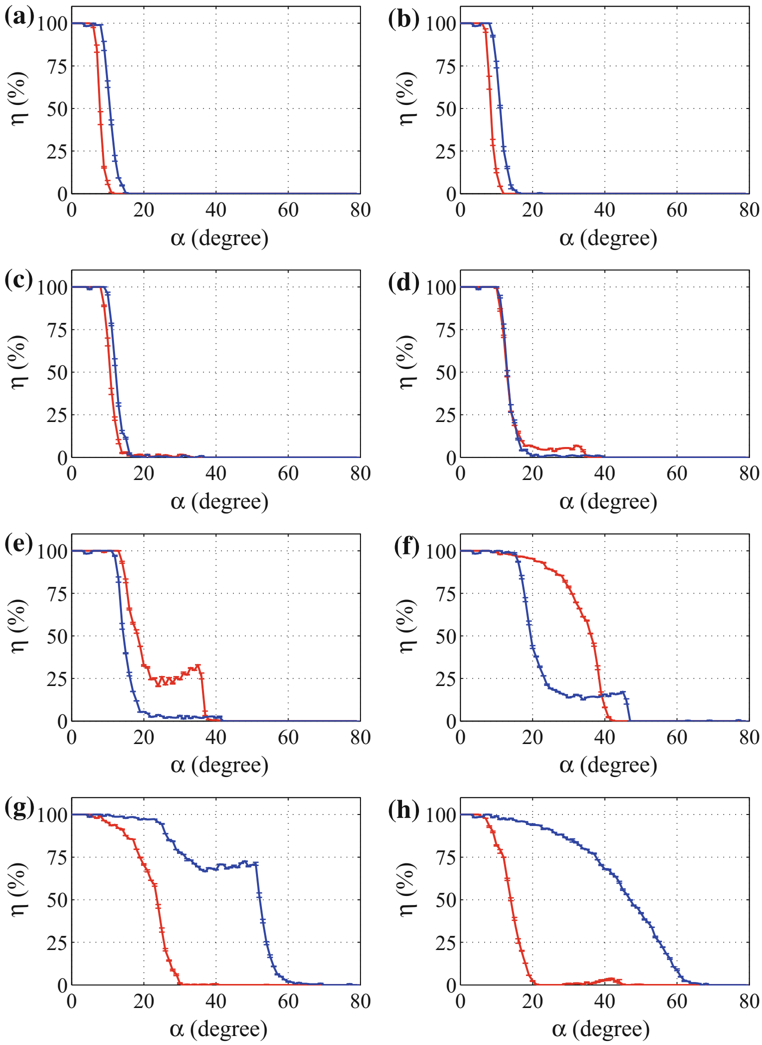

Fig. 3.35 The capture ratio of the Faraday as a function of electron emission position with different cathode positions and focusing solenoid strength. The blue and the red line denote the cathode No.1 and No.6 as listed in Table 3.1, respectively. **a** $B_\mathrm{f} = 0$ Gauss; **b** $B_\mathrm{f} = 250$ Gauss; **c** $B_\mathrm{f} = 500$ Gauss; **d** $B_\mathrm{f} = 625$ Gauss; **e** $B_\mathrm{f} = 750$ Gauss; **f** $B_\mathrm{f} = 1000$ Gauss; **g** $B_\mathrm{f} = 1250$ Gauss; **h** $B_\mathrm{f} = 1500$ Gauss

Table 3.3 Selected B_f values for different cathode positions to be compared with capture ratio dependence on emission position at cathode position No.1

Cathode position	No.2	No.3	No.4	No.5	No.6
$B_{f,equal}$[a] (Gauss)	750	750	750	625	625
$B_{f,errorbar}$[b] (Gauss)	625, 875	625, 875	625, 875	500, 750	500, 750

[a]Focusing solenoid strength for the same capture ratio dependence
[b]Focusing solenoid strength for the error bar

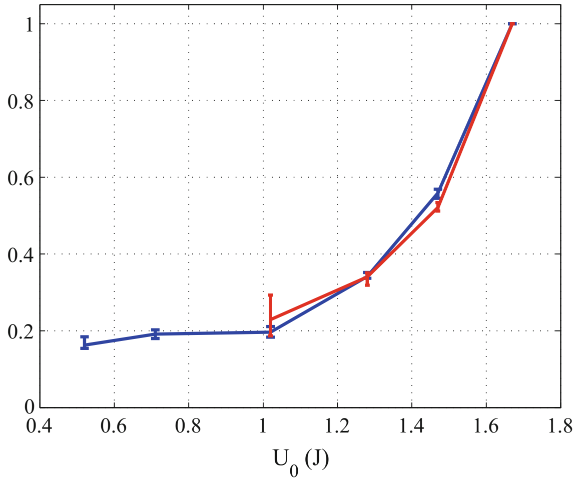

Fig. 3.36 Field emission current as a function of stored energy with the same E_{tip} of 625 MV/m. The current is normalized to that at cathode position No.6. The blue and the red line denote result of the ♯7 and the ♯15 pin cathode, respectively

5 is obtained when the stored energy was increased by threefold. The experimental results of the ♯7 and the ♯15 pin cathodes agree very well with each other.

3.3.3 *Possible Mechanisms*

The strong dependence of field emission on stored energy with the same E_{tip} is in contradiction to the conventional understanding of the F-N equation. This subsection presents research on mechanisms that may influence the observed strong dependence.

3.3.3.1 Field Emission from Other Surfaces

Although E_{tip} was kept constant by changing the cathode position, electric field on other surfaces (defined as background emission in this subsection), such as on the cathode hole edge and the iris, varied with change of the input power and stored energy. The difference between emission current from these surfaces might influence the experiment results.

To examine the background emission current from these surfaces, a flat copper cathode has been applied in the study, as shown in Fig. 3.37(a). The flat cathode was placed ∼3 mm behind the flush position, as illustrated in Fig. 3.37(b).

At this position, the cathode would not influence the electric field on other surfaces, as illustrated in Fig. 3.38. Besides, the electric field on the flat cathode is significantly lower than that on the cathode hole edge or the iris, so field emission current from the cathode itself would be negligible. To further reduce any possible emission current from the flat cathode, it has been carefully polished down to a surface roughness of 10–20 nm prior to the high power test. Therefore, the detected current with the flat cathode should be equal to the background emission with a pin cathode.

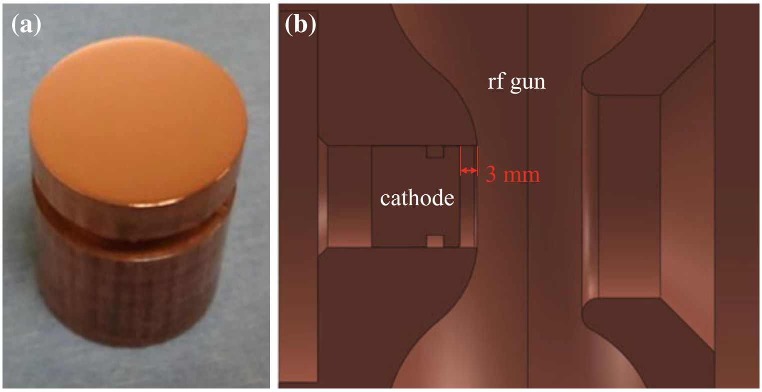

Fig. 3.37 The flat cathode to measure the background field emission current of the L-band high gradient photocathode rf gun. **a** The flat cathode after polishing; **b** The cathode position inside the rf gun

Fig. 3.38 The electric field distribution along the surface of the flat cathode (blue) and the pin cathode (red) at the same stored energy and input power

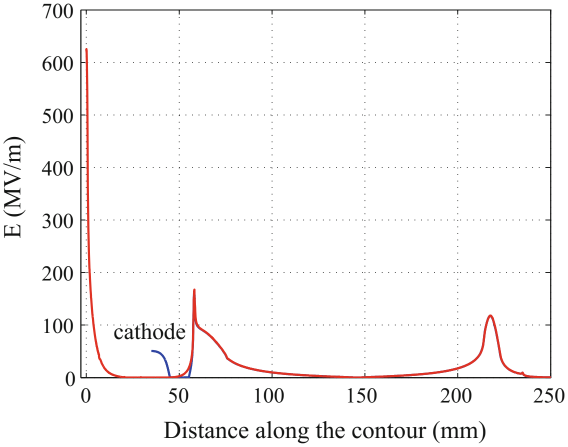

From the YAG screen on the beam line, the rough emission position could be vividly determined, as shown in Fig. 3.39. As expected, when applying the flat cathode, field emission was dominated by the symmetrical cathode hole edge, as shown in Fig. 3.39(a). Contrarily, with a pin cathode, field emission was mainly from the tip, as shown in Fig. 3.39(b).

With the same six stored energies as in the pin cathode case, the detected current from the rf gun with the flat cathode is illustrated in Fig. 3.40.

By comparing Figs. 3.28 and 3.40, the background emission current is lower than 1/5 of the total detected current with a pin cathode. After subtracting the background emission current, there is only ~5% change in the ratio of the field emission dependence on stored energy, as illustrated in Fig. 3.36. Conclusively, the influence of background current is negligible (Fig. 3.41).

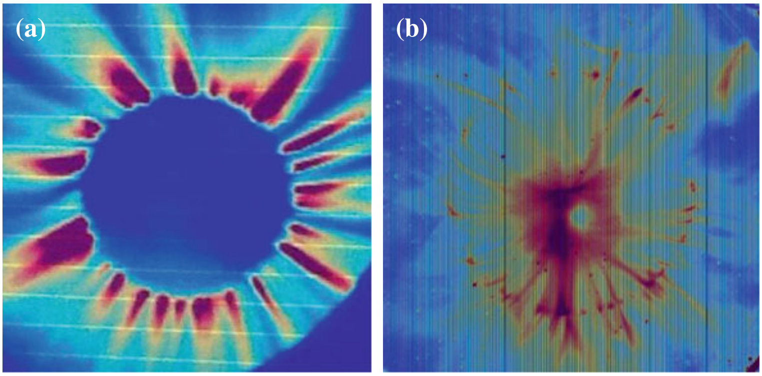

Fig. 3.39 Low resolution field emission images on the last YAG screen of the beam line. The symmetrical ring in both figures indicates the cathode hole edge. **a** The flat cathode; **b** The pin cathode

Fig. 3.40 With the flat cathode, the detected current as a function of B_f and stored energy. The scale of the y-axis is adjusted to be the same as Fig. 3.28 for better comparison

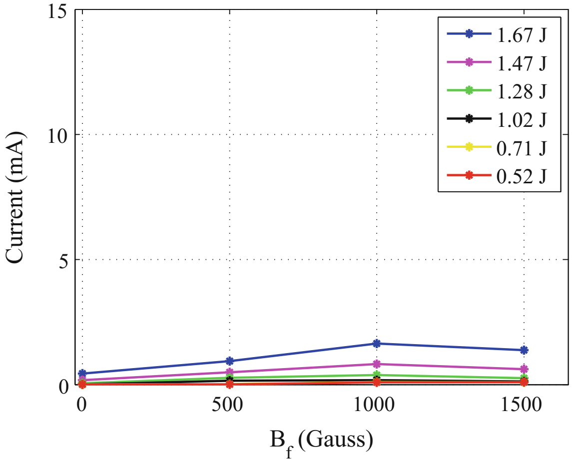

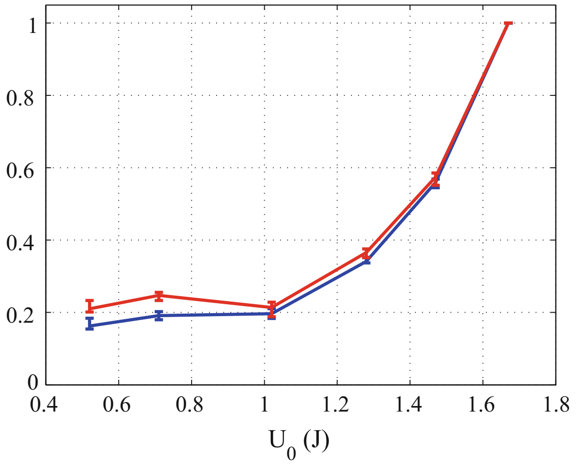

Fig. 3.41 Field emission current as a function of the stored energy with the same $E_{\text{tip}} = 625\,\text{MV/m}$ before (blue) and after (red) subtracting background emission from other surfaces of the rf gun

3.3.3.2 Secondary Electron Emission from the Faraday Cup

When field emission current arrived at the Faraday cup, secondary electrons could yield from the silicon mirror surface which would the reduce the detected emission current [24–26]. In this case, the detected current I_{out} and the incident current I_{in} would follow

$$I_{\text{out}} = I_{\text{in}}(1 - \delta_{\text{s}}) \tag{3.6}$$

where δ_{s} denotes the secondary electron yield.

For certain material, the secondary electron yield depends on the energy and angle of the incident electron as [27]

$$\begin{cases} \delta_{\text{s}} = \dfrac{\delta_{\text{s,max},\theta_{\text{s}}}}{g_{\text{n}}(z_{\text{m}})} g_{\text{n}}(z_{\text{m}} \dfrac{V_{\text{i}}}{V_{\text{max},\theta_{\text{s}}}}) \\ g_{\text{n}}(z) = \dfrac{1 - \exp(-z^{n+1})}{z^n} \\ V_{\text{max},\theta_{\text{s}}} = V_{\text{max},0}(1 + k_{\text{s}}\theta_{\text{s}}^2/\pi) \\ \delta_{\text{s,max},\theta_{\text{s}}} = \delta_{\text{s,max},0}(1 + k_{\text{s}}\theta_{\text{s}}^2/2\pi) \end{cases} \tag{3.7}$$

where $g_{\text{n}}(z)$ is maximized at z_{m}; $\delta_{\text{s,max},0}$ and $\delta_{\text{s,max},\theta_{\text{s}}}$ denote the maximum yield when the incident electron hits the surface perpendicularly or with an angle of θ_{s}; $V_{\text{max},0}$ and $V_{\text{max},\theta_{\text{s}}}$ denote the corresponding incident energy; n and k_{s} are constants which are assigned to be 0.35 and 1.5, respectively. For silicon, $\delta_{\text{s,max},0}$ and $V_{\text{max},0}$ are previously reported to be 2.5 and 500 eV, respectively [28].

For the six cathode positions used in the high power test, the angle and energy of the incident electrons onto the Faraday cup can be simulated by ASTRA code. Accordingly, the secondary electron yield from the surface can be calculated based on Eq. 3.7, as illustrated in Fig. 3.42. When the cathode was at position No.1 and

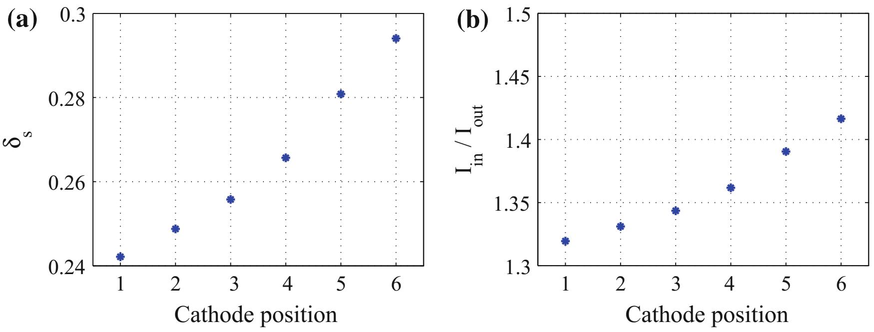

Fig. 3.42 Secondary electron yield of the Faraday cup surface as a function of cathode position with $E_{\text{tip}} = 625\,\text{MV/m}$. **a** δ_s; **b** $I_{\text{in}}/I_{\text{out}}$

Fig. 3.43 The increasing of the detected current as a function of the bias dc voltage. The blue and the red dots denote the results at cathode position No.1 and No.4, respectively

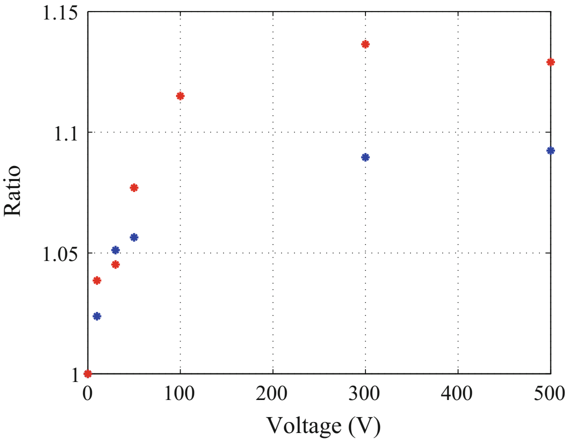

No.6, the ratio of the incident current to the detected one is calculated to be 1.32 and 1.42 with only 7% difference.

To confirm the calculation, a dc bias voltage up to 500 V has been applied to the Faraday cup to capture the secondary emission electrons. Figure 3.43 shows the experimental results of the detected current dependence on the bias voltage tested with the ♯15 pin cathode. The detected current saturated when the bias voltage was higher than 100 V, indicating a complete capture of the secondary emission electrons. A maximum current increase by a factor of ∼1.1 has been obtained, which is lower than the calculation value of 1.3–1.4. This might be caused by the inaccurate $\delta_{s,\max,0}$ and $V_{\max,0}$ applied in calculation. Despite the disagreement of the absolute value of secondary emission yield, the difference of the increasing factor at saturation between cathode position No.1 and No.4 was measured to be only 3%, displaying reasonable agreement with calculation.

Therefore, it can be summarized from both theoretical calculation and high power test findings that the influence of the secondary electron yield on the experiment results illustrated in Fig. 3.36 is negligible.

3.3.3.3 Beam Loading Effect

When a standing-wave structure is fully filled, the input rf power equals to the sum of power dissipated on the wall and absorbed by the beam [29]. The former one determines the surface field, which would be reduced by heavy beam loading. As a result, the field emission current would also be influenced.

The power absorbed by the beam can be expressed as

$$P_{\text{beam}} = \overline{W_{\text{beam}}} \times I_{\text{beam}} \tag{3.8}$$

where $\overline{W_{\text{beam}}}$ and I_{beam} are the average kinetic energy and current of the beam, respectively.

When the cathode is at position No.6 with E_{tip} of 625 MV/m, the maximum emission current is lower than 1 mA, as illustrated in Fig. 3.28(a). The maximum beam energy is simulated to be 0.9 MeV, resulting in a beam power lower than 0.9 kW. This value is significantly less than the 350 kW input power. Thus, the influence of beam loading effect on the experiment results of field emission dependence on stored energy is also negligible.

3.3.3.4 Space Charge Effect

When the emission current is high enough, the space charge effect near the cathode can reduce the following emission current. In the F-N coordinate, such effect would lead to bending of the linear curve at the high field end [30–32]. Such phenomenon has not been observed in the experiment with pin cathodes, which confirms the result of field emission dependence on stored energy is not caused by space charge effect.

3.3.4 Discussion

So far, all known factors have been excluded by the analysis in the previous subsection. The experimental results are proved to be reliable and the effect of global parameters on localized field emission is fundamental.

This discovery indicates the application of the F-N equation in many rf structure studies, including high gradient accelerators, might be incorrect. Under certain circumstances, when calculating the local surface electric field, higher order modes induced by the emission current should be considered together with the fundamental mode. This modification of the F-N equation application might help to solve the long-existing discrepancy between surface properties of the emission area obtained through direct observation using advanced surface analysis tools and those indirectly obtained from fitting the experimental data to the F-N equation as well as other questions surrounding field emission in rf case. Additionally, the findings may also lead to new optimization direction of high gradient rf structures, which is conventionally guided by reducing the electric field, the pulse heating, the modified Poynting vector, etc.

3.4 Summary

This section introduces the study with pin cathode which remarkably enhances the electric field on the tip to control rf breakdown and field emission location.

During rf conditioning, the maximum electric field on the tip has reached 700 MV/m, which is a new record in normal-conducting structures with microsecond pulse length. Field emission parameters, including field enhancement factor β and effective emission area A_e, have been measured during the rf conditioning process. Their evolution confirms continuous changing of the surface during the rf conditioning period. The nearly constant maximum surface field $\beta \cdot E_{\text{tip}}$ supports the hypothesis of breakdown threshold on copper surface. A comparison of the emission area between SEM observation and the F-N equation fitting also suggests that field emission current is not uniformly emitted from potential spots with high aspect ratio.

A strong correlation between the field emission current and the stored energy has been discovered on pin cathodes. This study has excluded mechanisms that may affect the conclusion, such as multipacting in the cavity, background emission from other surfaces, secondary electron emission from the Faraday cup, the beam loading effect, and the space charge limited emission effect. The observation is fundamental but inconsistent with the Fowler-Nordheim equation, which indicates that global parameters like stored energy affects the localized field emission phenomenon. These findings point out a new territory yet to be explored while developing field emission electron sources and high gradient rf structures.

The study of the pin cathode conditioning and field emission parameters evolution has been published in the proceedings of the 16th Advanced Accelerator Concepts Workshop (AAC2014) [33]. The study of field emission dependence on stored energy has been published in Phys. Rev. Lett. 115, 264802 (2015) [34].

References

1. Ho C, Yang T, Hwang J et al (1998) SRRC/ANL high current L-band single cell photocathode rf gun. In Proceedings of EPAC1998, Stockholm, Sweden
2. Billen J, Young L (1996) Poisson Superfish. Technical report LA-UR-96-1834, Los Alamos National Laboratory

3. Ko K, Candel A, Ge L et al (2010) Advances in parallel electromagnetic codes for accelerator science and development. In Proceedings of LINAC2010, Tsukuba, Japan
4. Wang JW, Loew GA (1997) Field emission and rf breakdown in high-gradient room-temperature linac structures. Technical report SLAC-PUB-7684, SLAC
5. Degiovanni A, Wuensch W, Navarro J (2016) Comparison of the conditioning of high gradient accelerating structures. Phys Rev Accel Beams 19:032001
6. Wiener J, Padamsee H (2008) Improvements in field emission: An updated statistical model for electropolished baked cavities. Technical report TESLA 2008-02, DESY
7. Levinsen Y, Descoeudres A, Calatroni S et al (2009) Statistical modeling of dc sparks. In Proceedings of PAC09, Vancouver, Canada
8. Descoeudres A, Levinsen Y, Calatroni S et al (2009) Investigation of the dc vacuum breakdown mechanism. Phys Rev ST Accel Beams 12:092001
9. Descoeudres A, Ramsvik T, Calatroni S et al (2009) dc breakdown conditioning and breakdown rate of metals and metallic alloys under ultrahigh vacuum. Phys Rev ST Accel Beams 12:032001
10. Timko H, Aicheler M, Alknes P et al (2011) Energy dependence of processing and breakdown properties of Cu and Mo. Phys Rev ST Accel Beams 14:101003
11. Dolgashev V (2013) Recent high gradient tests at SLAC. In Proceedings of HG2013, ICTP Trieste, Italy
12. Zha H (2013) Design and experiment of CLIC choke-mode accelerating structure. Ph.D. thesis, Tsinghua University
13. Timko H, Matyash K, Schneider R et al (2011) A one-dimensional particle-in-cell model of plasma build-up in vacuum arcs. Contrib Plasma Phys 51:1
14. Wang F (2015) The macroscopic field emission. In Proceedings of HG2015, Beijing, China
15. Hatch A, Williams H (1958) Multipacting modes of high-frequency gaseous breakdown. Phys Rev 112:681–685
16. Vaughan J, Trans IEEE (1988) Multipactor. Electron Devices 35:1172–1180
17. Gilardini A (1995) Multipacting discharges: Constant-k theory and simulation results. J Appl Phys 78:783–795
18. Han J, Flottmann K, Hartung W (2008) Single-side electron multipacting at the photocathode in rf guns. Phys Rev ST Accel Beams 11:013501
19. Flöttmann K (2014) ASTRAA space charge tracking algorithm, DESY
20. Li X, Li M, Dan L et al (2013) Cold cathode rf guns based study on field emission. Phys Rev ST Accel Beams 16:123401
21. Zheng L, Du Y, Huang W et al (2015) Simulation of dark current and dark current-induced background photons in the Thomson scattering X-ray source. Nucl Instrum Methods Phys Res, Sect A 800:12–17
22. Huang R, Filippetto D, Papadopoulos C et al (2015) Dark current studies on a normal-conducting high-brightness very-high-frequency electron gun operating in continuous wave mode. Phys Rev ST Accel Beams 18:013401
23. Ganter R, Bakker R, Gough C et al (2006) Nanosecond field emitted and photo-field emitted current pulses from ZrC tips. Nucl Instrum Methods Phys Res, Sect A 565:423–429
24. Dionne G (1975) Origin of secondary-electron-emission yield-curve parameters. J Appl Phys 46:3347–3351
25. Pearlman J (1977) Faraday cups for laser plasmas. Rev Sci Instrum 48:1064–1067
26. Furman M, Pivi M (2002) Probabilistic model for the simulation of secondary electron emission. Phys Rev ST Accel Beams 5:124404
27. Vaughan J, Trans IEEE (1989) A new formula for secondary emission yield. Electron Devices 36:1963–1967
28. Joy D (1987) A model for calculating secondary and backscattered electron yields. J Microsc 147:51–64
29. Shao J, Du Y, Zha H et al (2013) Development of a C-band 6 MeV standing-wave linear accelerator. Phys Rev ST Accel Beams 16:090102
30. Barbqur J, Dolan W, Trolan J et al (1953) Space-charge effects in field emission. Phys Rev 92:45–51

31. Forbes R (2008) Exact analysis of surface field reduction due to field-emitted vacuum space charge, in parallel-plane geometry, using simple dimensionless equations. J Appl Phys 104:084303
32. Rokhlenko A, Jensen K, Lebowitz J (2010) Space charge effects in field emission: One dimensional theory. J Appl Phys 107:014904
33. Shao J, Antipov S, Baryshev S et al (2014) Field emission study using an L-band photocathode gun. In Proceedings of AAC2014, San Jose, USA
34. Shao J, Antipov S, Baryshev S et al (2015) Observation of field-emission dependence on stored energy. Phys Rev Lett 115:264802

Chapter 4
In-situ High Resolution Field Emission Imaging

Abstract The previous two chapters introduce the study to control the location of rf breakdown and field emission by means of high intensity laser and pin cathode. To locate uncontrolled field emitters, a novel method called in-situ high resolution field emission imaging has been proposed and successfully demonstrated in this Chapter. With this method, scattered strong emission area with high current have been observed on the cathode with high resolution (∼100 µm). The field enhancement factor β of selected regions on the cathode has been measured. Ex-situ SEM and WLI surface examinations reveal that ∼75% strong emission areas overlap with rf breakdown spots. The theory, simulation, and experiment of the in-situ high resolution field emission imaging will be presented in detail in this chapter.

4.1 Imaging Method

4.1.1 Difficulties

In earlier field emission studies under a dc field, emission mapping with better than 1 µm resolution has been achieved by scanning an anode along the cathode [1–3]. However, to image the emission areas with high resolution while they are emitting under an rf field is extremely challenging due to the complicated dynamics of emission electrons in both the rf structure and the following beam transport system [4–6].

For field emission electron whose space charge effect is negligible and initial kinetic energy is low, its dynamics in an rf structure is mainly determined by the emitting phase. Figure 4.1 shows an ASTRA simulation example of electrons emitted from a zero-size emitter on the flat cathode of the L-band high gradient single-cell photocathode rf gun at AWA. As introduced in Chap. 3, field emission electrons emit from 0° to 180° rf phase with a standard deviation of ∼20° with maximum surface electric field of 8–15 GV/m. Electrons from this wide emission range occupy a finite area in the transverse space which limits the observation resolution.

The electrons are usually transported to diagnostics downstream of a beam line with focusing components such as solenoid and quadrupole whose focusing strength

J. Shao, *Investigations on rf Breakdown Phenomenon in High Gradient Accelerating Structures*, Springer Theses, https://doi.org/10.1007/978-981-10-7926-9_4

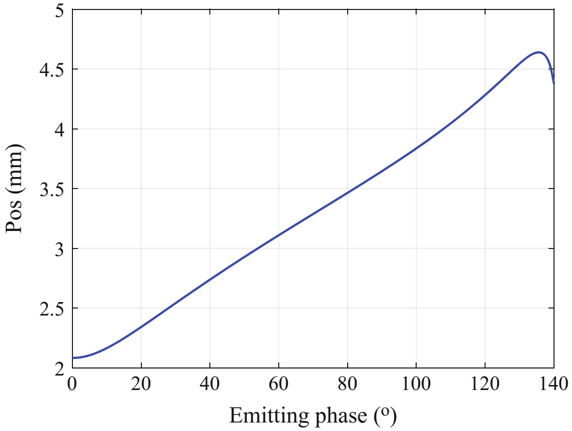

Fig. 4.1 Transverse position in x or y direction at the gun exit of field emission electron as a function of emitting phase. The initial off-axis of the emitter on the cathode is 1 mm in both x and y direction. The macroscopic electric field on the cathode is 100 MV/m with 2 MW input power

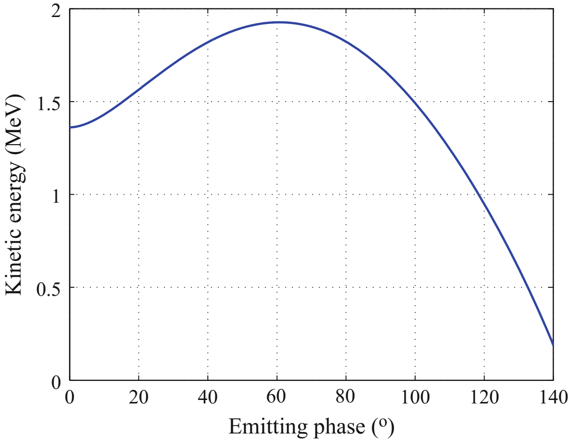

Fig. 4.2 The electron energy at the gun exit as a function of emitting phase in the L-band high gradient single-cell photocathode rf gun

depends on the beam energy. For instance, the focusing length of a solenoid with thin-lens approximation can be expressed as [7]

$$\frac{1}{f} = (\frac{e}{2m_0 c\beta_c\gamma_c})^2 B_0^2 l \tag{4.1}$$

where e and m_0 denote the charge and rest mass of electron, c denotes the speed of light, β_c denotes the speed of electron, γ_c denotes the Lorenz factor, B_0 and l denote the effective magnetic field and length of the solenoid. In rf structures, the energy of field emission electron at the exit also depends on the emitting phase, as illustrated in Fig. 4.2. Thus, focusing components in the beam transport system may further deteriorate the resolution of field emitter observation.

To vividly address the difficulty of high resolution field emitter mapping in rf structures, 12 zero-size emitters have been placed azimuthally on the cathode of the

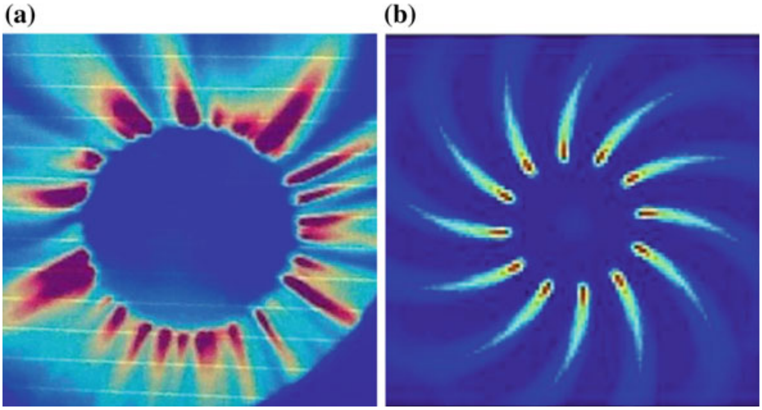

Fig. 4.3 Typical field emission image at downstream of the L-band photocathode rf gun. **a** Experimental results; **b** Simulation results

L-band photocathode rf gun in ASTRA simulation. Figure. 4.3b shows the distribution of electron transverse location at the gun exit with low resolution in which the initial emitters can not be clearly distinguished. The results agree well with the typical blurred field emission image captured in experiment, as shown in Fig. 4.3a.

4.1.2 Solution

In order to obtain high resolution field emitter mapping in rf structures, electrons from certain emitting phases with certain energies need to be discriminated and selected. A novel method using solenoid and collimator has been proposed in this study. As the focusing strength of solenoid depends on the beam energy which is determined by the emitting phase, a collimator with a small aperture is placed after the solenoid so that only electrons with proper energy/emitting phase can pass through it while others are totally blocked.

The method can be interpreted as an optical system in which the cathode and the solenoid denote the object and the lens, respectively. Before the collimator, the setup is equivalent to a lens imaging system. After the collimator, it becomes a pinhole camera, as illustrated in Fig. 4.4.

Figure 4.5 shows an ASTRA simulation example of the high resolution field emission imaging process. Four emitters are located on the flat cathode of the L-band single-cell high gradient photocathode rf gun (Fig. 4.5a). Due to the transverse position dependence on the emitting phase, long tail could be observed in the field emission pattern at the gun exit (Fig. 4.5b). After focusing by the solenoid, the patterns from the four emitters overlap with each other (Fig. 4.5c). On the YAG screen at the imaging position, a blurred image with low resolution in which the four emitters could hardly be distinguished is formed when no collimator is applied (Fig. 4.5d). After applying a collimator with a small aperture, the four emitters could be well

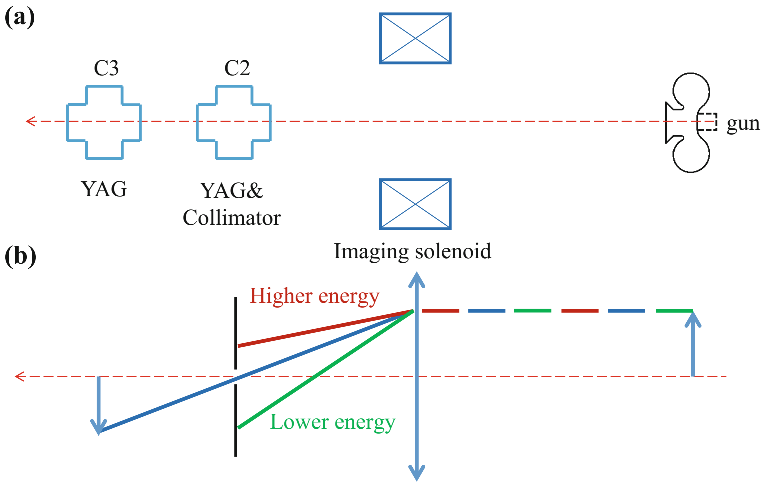

Fig. 4.4 A comparison between the high resolution field emission imaging setup (**a**) and an optical system (**b**)

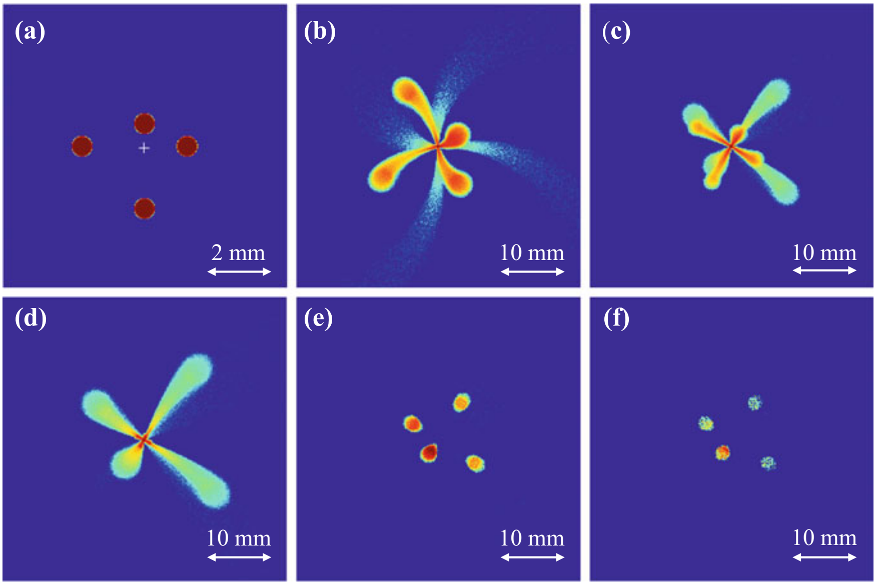

Fig. 4.5 Field emission pattern at different positions. **a** The cathode, the white cross denotes the cathode center; **b** The gun exit; **c** The collimator; **d**–**f** The imaging plane. **d** Without collimator; **e** With Φ1 mm collimator; **f** With Φ0.2 mm collimator

reproduced (Fig. 4.5e) and the resolution improves when as the aperture size reduces (Fig. 4.5f).

4.2 Dynamics Simulation

To study the imaging properties, systematic dynamics simulation with the flat cathode has been preformed using ASTRA code. Space charge has been ignored in the dynamics simulation.

4.2.1 *Imaging Properties*

The imaging properties studied in simulation include brightness (capture ratio of the system), magnification, rotation, resolution, and viewable cathode range.

To study the imaging properties, a coordinate has been established on the cathode and its origin is set at the cathode center, as shown in Fig. 4.6. For an emitter located at (x_0, y_0) in the Cartesian coordinate or (ρ_0, φ_0) in the polar coordinate, the electron emitting angle is defined in the local coordinate (x_L, y_L, z_L) where x_L is along the φ_0 direction and z_L is parallel to z. The emitting momentum $\overline{p} = (p_{x_L}, p_{y_L}, p_{z_L})$ can be expressed as

$$\begin{cases} p_{x_L} = p\cos\theta\cos\phi \\ p_{y_L} = p\cos\theta\sin\phi \\ p_{z_L} = p\sin\theta \end{cases} \tag{4.2}$$

where p denotes the amplitude, $\theta \in [0, 90°]$ and $\phi \in [-180°, 180°]$ denote the angle with respect to the axises, as shown in Fig. 4.6

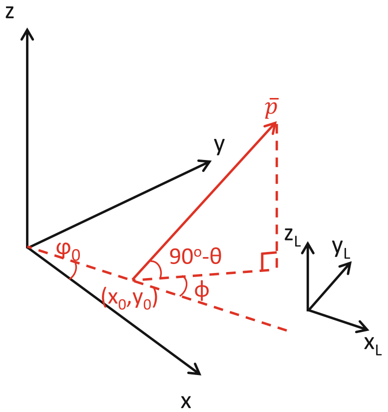

Fig. 4.6 The coordinate of emitter location and emitting angle

Similarly, a polar coordinate has also been established on the YAG at the imaging position as $\rho_{\text{YAG}} - \varphi_{\text{YAG}}$. The origin is set at the YAG center.

Brightness

The brightness of the image is proportional to the number of electrons arriving at the YAG screen N_{YAG}. For a fixed emitting current from an emitter on the cathode, the brightness is equivalent to the capture ratio of the imaging system which is defined as

$$\eta = \frac{N_{\text{YAG}}}{\sum_{\vartheta,\theta,\phi} N(\vartheta, \theta, \phi)} \tag{4.3}$$

Magnification

Because of the finite size of the aperture, multiple electrons from the same emitter can arrive at the YAG screen with different transverse positions ($\rho_{\text{YAG}}(\vartheta, \theta, \phi)$, $\varphi_{\text{YAG}}(\vartheta, \theta, \phi)$). Therefore, the magnification of the imaging system is defined in an average manner as

$$\overline{mag} = \frac{\overline{\rho_{\text{YAG}}(\vartheta, \theta, \phi)}}{\rho_0} \tag{4.4}$$

Rotation

Similarly, the average rotation angle of the imaging system can be defined as

$$\overline{rot} = \overline{\varphi_{\text{YAG}}(\vartheta, \theta, \phi)} - \varphi_0 \tag{4.5}$$

Resolution

All components in the imaging system are axis-symmetric, including the photocathode rf gun, the cathode, the solenoids, and the collimator with aperture. Therefore, the resolution of the imaging system is defined both radially and angularly. The former one determines the capability to distinguish emitters with different ρ_0. While the latter one determines the capability to distinguish emitters with the same ρ_0 but different φ_0. In the dynamics simulation, the electron transverse position on the YAG screen is assumed to follow Gaussian distribution with standard deviation of δ_ρ and δ_φ. For emitters with different positions on the cathode, when $\overline{mag}$ and δ_ρ are constant, the radial and angular resolution can be defined as

$$\begin{cases} R_\rho = 2.35 \times \dfrac{\delta_\rho}{\overline{mag}} & (4.6) \\ R_\varphi = 2.35 \times \delta_\varphi \rho_0 & (4.7) \end{cases}$$

It's notable that these four imaging properties are related to the initial emitter position ρ_0 due to the spherical aberration of components in the setup.

Range

The range of the imaging system is defined as the maximum off-axis of an emitter on the cathode that can be detected by the imaging system. The range is limited by the size of the beam pipe as well as the spherical aberration.

4.2.2 Electron Distribution

For an field emission electron, there are four adjustable parameters in the dynamics simulation, including emission position x_0 and y_0, emission momentum p, and current I.

The dependence of the emission current on the emitting phase can be determined by the F-N equation and has been approximated by a Gaussian distribution, as introduced in Sect. 3.3.2.1.

Two different distributions of the emission momentum have been applied in simulation with fixed emission energy E_k of 100 meV [8]. The first distribution, also the default one in the chapter, is used to study the dependence of imaging properties on selection phase and on beam line parameters such as solenoid strength and rf gun gradient. In this momentum distribution, the initial emittance is set to zero so that all electrons emit perpendicularly to the cathode. The second one is applied to study the influence of initial emittance on imaging properties in which the emission angles θ and ϕ are assumed to distribute uniformly within their maximum ranges. The dimensionless rms transverse moment $\delta_{p_{x,y}}$ can be calculated as

$$\delta_{p_{x,y}} \equiv \frac{\sqrt{\langle p_{x,y}^2 \rangle}}{m_e c^2} = \sqrt{\frac{E_k}{2m_e c^2}} \tag{4.8}$$

The result is larger than the value of $\sqrt{E_k/(3m_e c^2)}$ in the emittance theory [9] due to the simplified θ distribution.

4.2.3 Emission Phase Selection

This subsection introduces the basis of emitting phase selection which is pivotal in the high resolution field emission imaging system.

Figure 4.7 shows the layout of the beam line in the dynamics simulation. The bucking and focusing solenoid is placed 0.12 m from the rf gun symmetrically with opposite current to cancel the magnetic field at the cathode. The imaging solenoid, the collimator, and the YAG screen are located at 0.84, 1.40, and 1.85 m away from

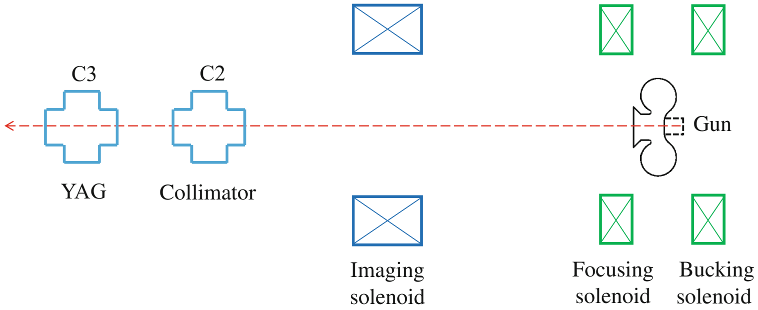

Fig. 4.7 The layout of the high resolution field emission imaging system in ASTRA simulation

Fig. 4.8 The electron offset from the axis at the collimator position as a function of emission phase. The red line denotes the aperture radius

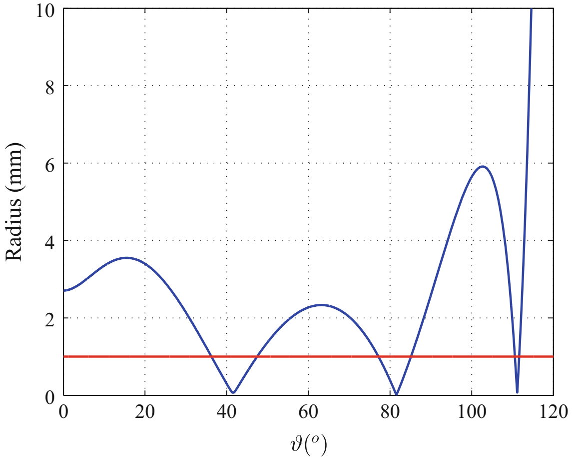

the cathode, respectively. The current direction of the imaging solenoid is opposite to that of the focusing solenoid to obtain higher angular resolution.

For given beam line parameters, the trajectory of emission electron is mainly determined by the emission phase. At the collimator location, the off-axis position of electrons from a fixed zero-size emitter on the cathode as a function of the emission phase is illustrated in Fig. 4.8. Electrons with off-axis smaller than the radius of the aperture can pass through the collimator while others are blocked.

Typically, electrons from three groups of emitting phase can pass through the aperture and arrive at the AG screen, as illustrated in Fig. 4.8. The energy levels in the first two groups of electrons with lower phases are similar, but are remarkably higher than those of the last group, as illustrated in Fig. 4.9. As the focusing strength of the imaging solenoid depends on the beam energy, electrons in the first two groups have similar dynamics after the rf gun, which can also be confirmed by their trajectories along the beam line, as illustrated in Fig. 4.10. On the other hand, electrons with

Fig. 4.9 The electron kinetic energy at the photocathode rf gun exit as a function of emission phase. The three red parts denote the electrons through the collimator

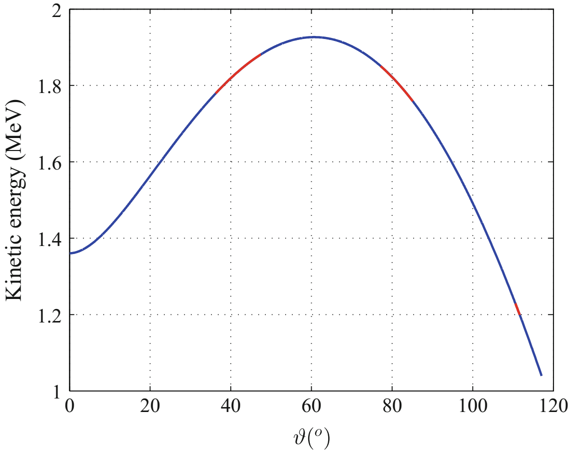

Fig. 4.10 Field emission electron trajectory along the beam line. The blue, the red, and the black line denote exemplary electrons from the three groups respectively

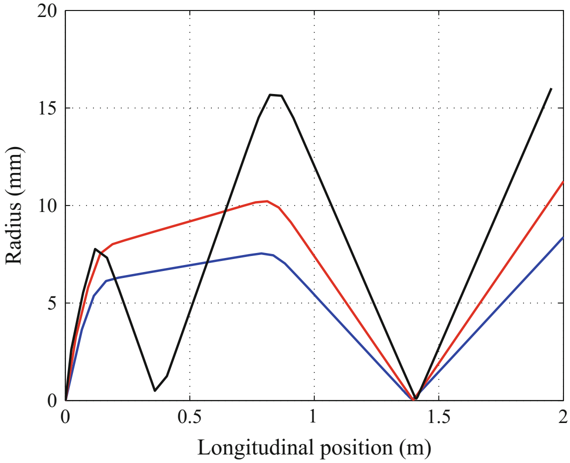

lower energy in the third group has been over-focused by the focusing solenoid before entering the imaging solenoid.

After considering the field emission current distribution within one rf period as illustrated in Fig. 3.30, the number of electrons in the second group is two orders of magnitude more than the other two groups. Therefore, only the second group is taken into consideration in the following analysis for simplicity.

4.2.4 Beam Line Optimization

This subsection introduces the beam line optimization for the imaging properties, aiming to obtain high capture ratio, high magnification, high resolutions, and large imaging range. Four beam line parameters have been adjusted and optimized in the simulation, including the radius of the collimator aperture r_{ap}, the maximum on-axis magnetic field of the focusing and imaging solenoid B_{f} and B_{i}, and the macroscopic electric field on the cathode E_{c} without field enhancement factor. The effect of initial emittance on imaging properties has also been studied in this subsection.

4.2.4.1 Aperture Size

Figure 4.11 illustrates an example of the dependence of imaging properties on the collimator aperture size. In the simulation, electrons emit from a zero-size emitter placed at position ($x_0 = 1\,\mathrm{mm}$, $y_0 = 0\,\mathrm{mm}$) on the cathode. E_{c} and B_{f} are set to be 100 MV/m and 1500 Gauss, respectively. B_{i} is adjusted to select electrons with the highest energy (emitting phase near $\sim 62^\circ$). With larger aperture size, electrons from a wider emission phase range can pass through the collimator, leading

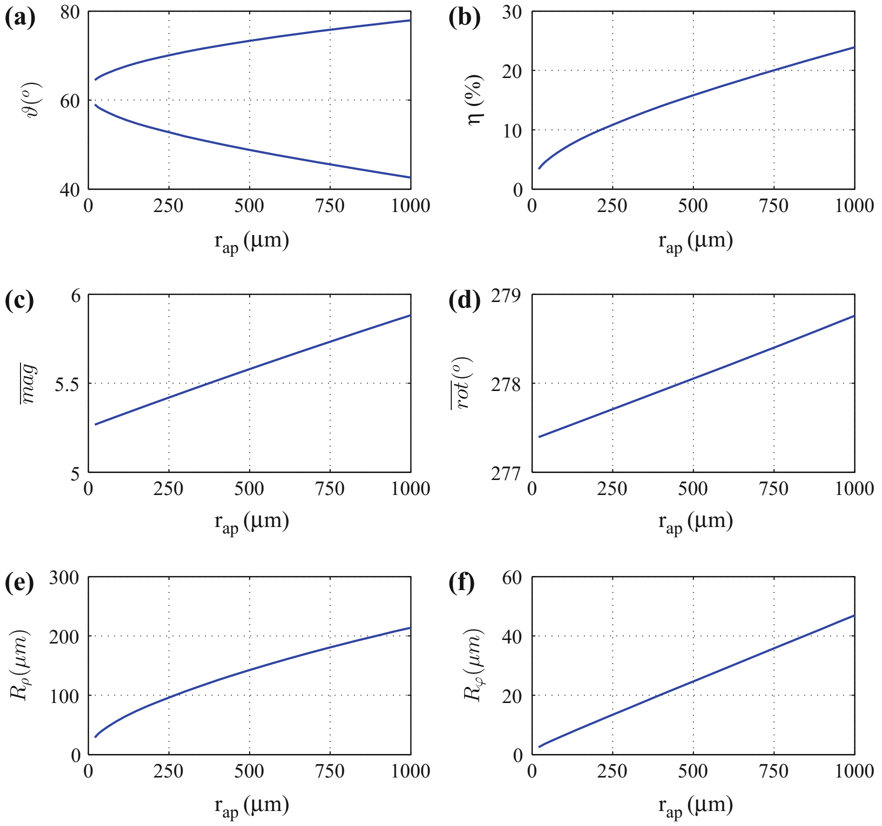

Fig. 4.11 Imaging parameters as a function of the aperture size. a Phase selection range; **b** Capture ratio; **c** Average magnification; **d** Average rotation; **e** Radial resolution; **f** Angular resolution

to higher capture ratio but worse resolutions. Meanwhile, the average magnification and rotation remain nearly constant when the aperture size varies.

In experiment, the aperture size needs to be chosen to compromise between the capture ratio and the resolutions.

4.2.4.2 Imaging Solenoid Strength

Because of the focusing strength dependence on beam energy, the average emission phase of collimator selected electrons can be adjusted by the the imaging solenoid, as illustrated in Fig. 4.12. The average selection phase becomes closer to 62° (corresponding to the maximum energy at the gun exit) when the imaging solenoid strength increases.

Apart from the strength, the current direction of the imaging solenoid is also a key factor in the high resolution field emission imaging system. By setting the direction opposite to that of the focusing solenoid, it has been found that the angular resolution is significantly improved, as illustrated in Fig. 4.13. Except the average rotation, other imaging properties are not influenced by the solenoid current direction. Therefore, the direction opposite to that of the focusing solenoid has been applied to the imaging solenoid in following dynamics simulation as well as the high power test.

Figure 4.14 illustrates an example of the dependence of imaging properties on the imaging solenoid strength/average selection phase. In the simulation, electrons emit from a zero-size emitter placed at position ($x_0 = 1$ mm, $y_0 = 0$ mm) on the cathode. E_c, B_f, and r_{ap} are set to be 100 MV/m, 1500 Gauss, and 100 μm, respectively. With lower imaging solenoid strength or higher average selection phase, capture ratio and average magnification decrease while imaging resolutions improve.

With the same setting of E_c, B_f, B_i, and r_{ap}, Fig. 4.15 illustrates the imaging properties of different emitters on the cathode when the average selection phase is

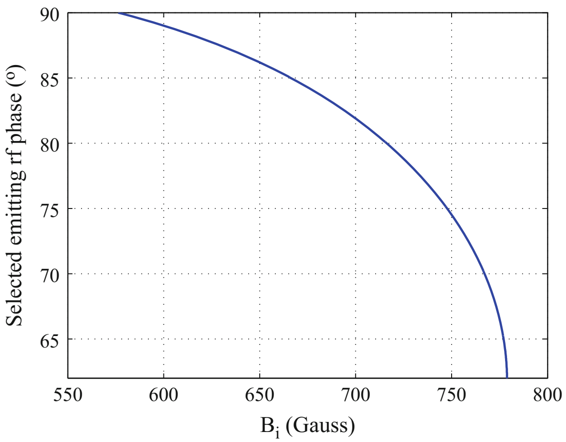

Fig. 4.12 The average selection emission phase as a function of the imaging solenoid strength

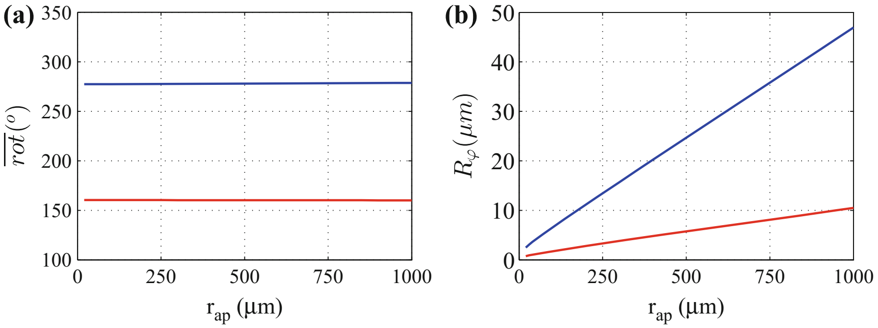

Fig. 4.13 Imaging properties with the same (blue) and opposite (red) current direction of the focusing and the imaging solenoids. **a** Average rotation; **b** Angular resolution

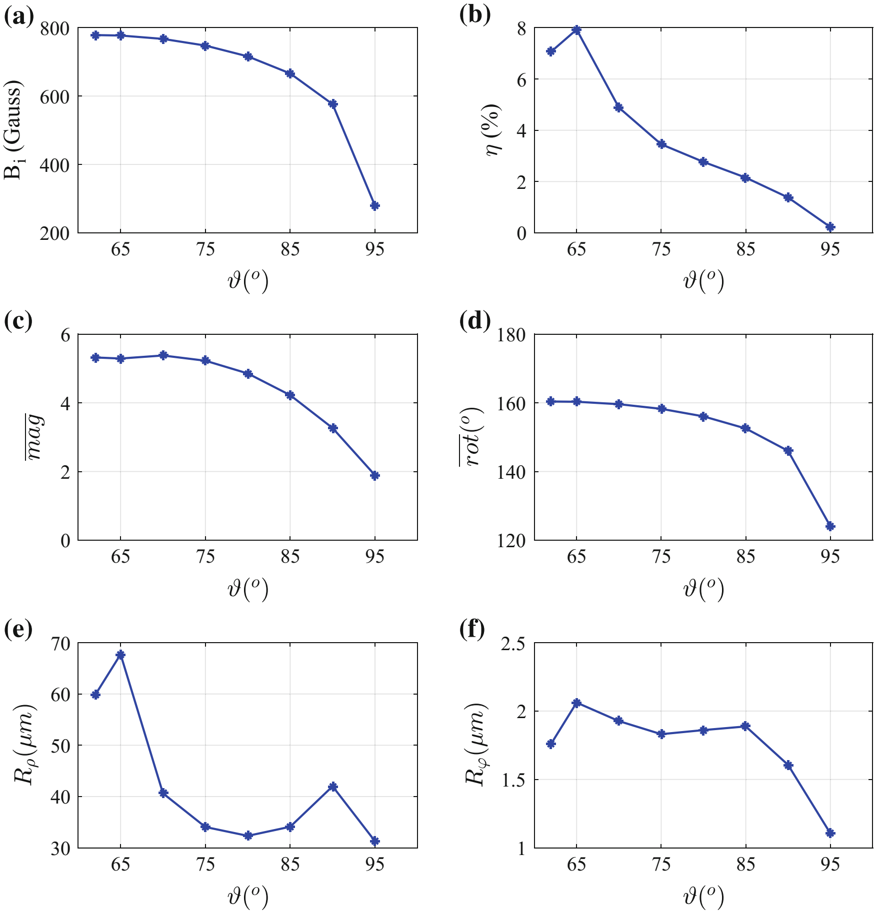

Fig. 4.14 Imaging parameters as a function of average selection phase. **a** B_i; **b** Capture ratio; **c** Average magnification; **d** Average rotation; **e** Radial resolution; **f** Angular resolution

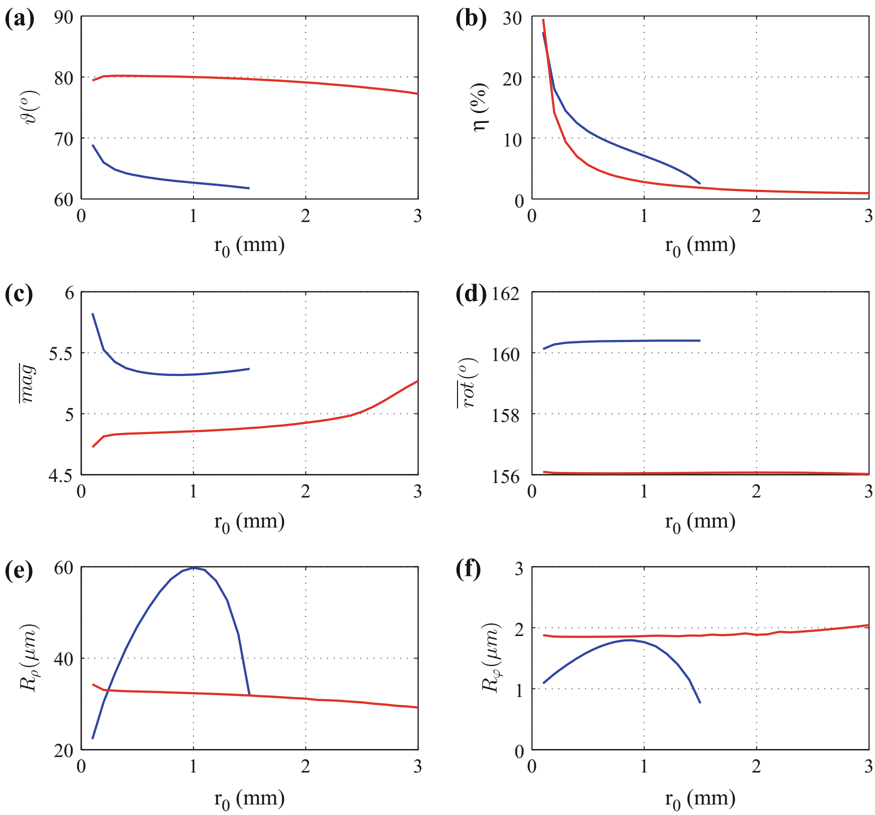

Fig. 4.15 Imaging properties as a function of emitter position on the cathode. The blue and the red line denote the average selection phase of 62° and 80°, respectively. **a** Average selection phase; **b** Capture ratio; **c** Average magnification; **d** Average rotation; **e** Radial resolution; **f** Angular resolution

62° or 80°. Along the imaging solenoid, electrons emit from outer emitter on the cathode experience stronger magnetic field due to the spherical aberration. As B_i is set to select electron with highest energy from an emitter located at ($x_0 = 1$ mm, $y_0 = 0$ mm), electrons from an outer emitter are over-focused before reaching the collimator and therefore blocked. As a result, the imaging range is more limited than the case when the imaging solenoid strength is low and average selection phase is high. Additionally, the variation of the radial resolution is more significant when the imaging solenoid strength is set to select electrons with the highest energy from inner emitters, which violates the radial resolution definition. Thus, high average selection phases are desired in the imaging system even with low capture ratio and magnification.

4.2.4.3 Focusing Solenoid Strength

Figure 4.16 illustrates an example of the dependence of imaging properties on the focusing solenoid strength. In the simulation, electrons emit from a zero-size emitter placed at position ($x_0 = 1$ mm, $y_0 = 0$ mm) on the cathode. E_c and r_{ap} are set to be 100 MV/m and 100 μm, respectively. B_i is adjusted for average selection phase of 70°, 80°, and 90°. The results show higher capture ratio but lower average magnification and radial resolution when B_f increases.

Figure 4.17 illustrates the imaging range with the same setting of E_c, B_f, B_i, and r_{ap}. Larger imaging range can be obtained by increasing B_f. Therefore, there is no single setting of B_f can reach the best result and compromise between capture ratio, magnification, resolutions, and imaging range is necessary.

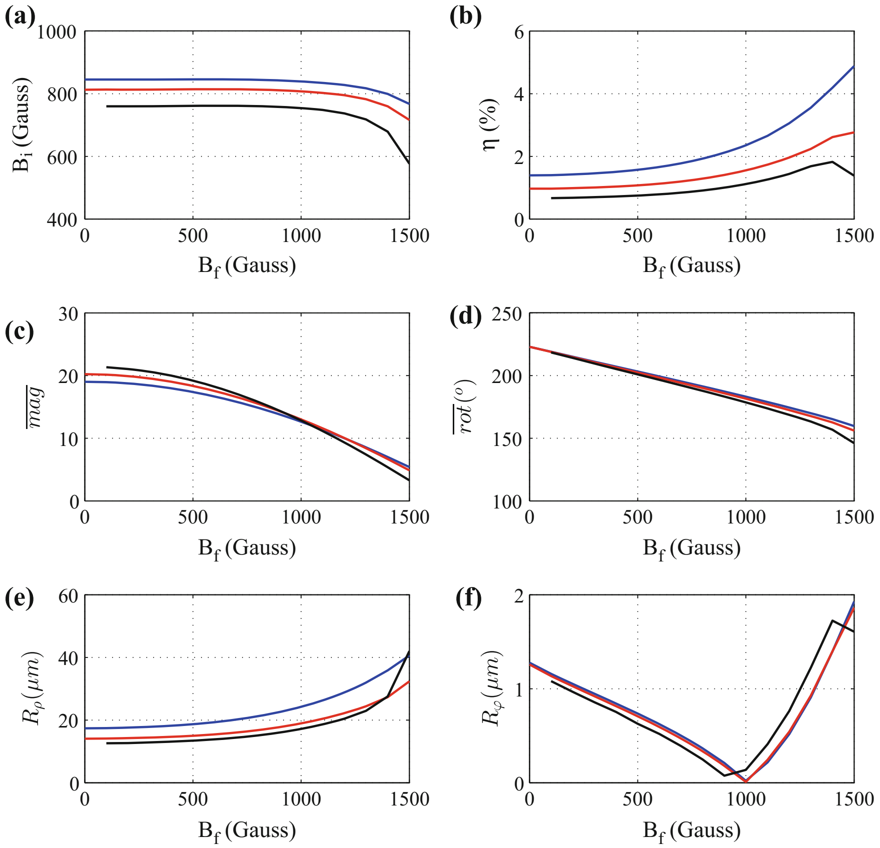

Fig. 4.16 Imaging properties as a function of the focusing solenoid strength. The blue, the red, and the black line denote the average selection phase of 70°, 80°, and 90°, respectively. **a** B_i; **b** Capture ratio; **c** Average magnification; **d** Average rotation; **e** Radial resolution; **f** Angular resolution

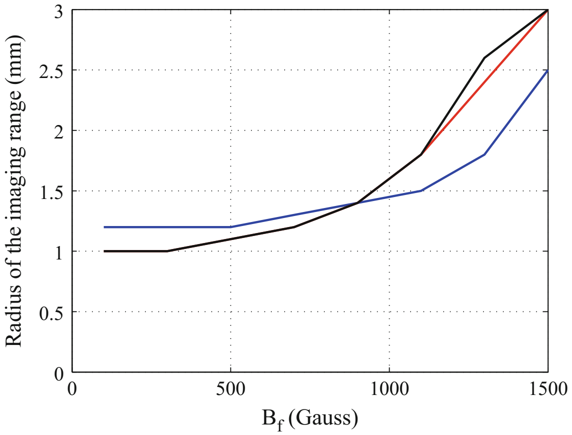

Fig. 4.17 The imaging range as a function of the focusing solenoid strength. The blue, the red, and the black line denote the average selection phase of 70°, 80°, and 90°, respectively

4.2.4.4 Macroscopic Electric Field

Figure 4.18 illustrates an example of the dependence of imaging properties on the macroscopic electric field. In the simulation, electrons emit from a zero-size emitter placed at position ($x_0 = 1$ mm, $y_0 = 0$ mm) on the cathode. B_{f} and r_{ap} are set to be 1500 Gauss and 100 μm, respectively. B_{i} is adjusted for average selection phase of 70° and 90°. The results indicate high E_{c} is desired for the imaging system in terms of high magnification and high resolutions. Additionally, the brightness of field emission images increases exponentially with E_{c} up regulation according to the F-N equation.

4.2.4.5 Initial Emittance

In previous simulation, the initial emittance has been set to zero with all electrons emit perpendicularly to the cathode for simplicity. When the emitting angles are uniformly distributed within their maximum range, the initial emittance will be $\sqrt{E_k/(2m_ec^2)}$. Figure 4.19 illustrates an example of the influence of the initial emittance on the resolutions. In the simulation, electrons emit from a zero-size emitter placed at position ($x_0 = 1$ mm, $y_0 = 0$ mm) on the cathode. E_{c} and B_{f} are set to be 100 MV/m and 1500 Gauss, respectively. B_{i} is adjusted for average selection phase of 80°. The capture ratio, the average magnification, and the average rotation are not effected by the initial emittance.

4.2.4.6 Chosen Parameters

As a summary of the simulation results, the beam line parameters need to compromise with different imaging properties. For the first demonstration experiment performed

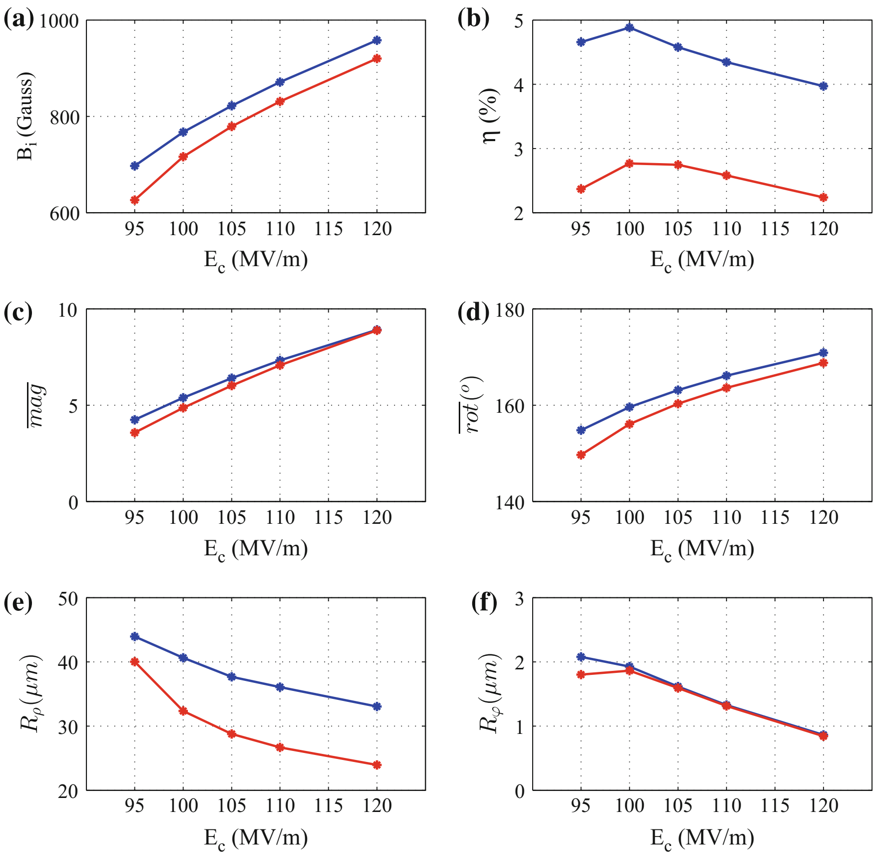

Fig. 4.18 Imaging properties as a function of the macroscopic electric field. The blue and the red line denote the average selection phase of 70° and 80°, respectively. **a** B_i; **b** Capture ratio; **c** Average magnification; **d** Average rotation; **e** Radial resolution; **f** Angular resolution

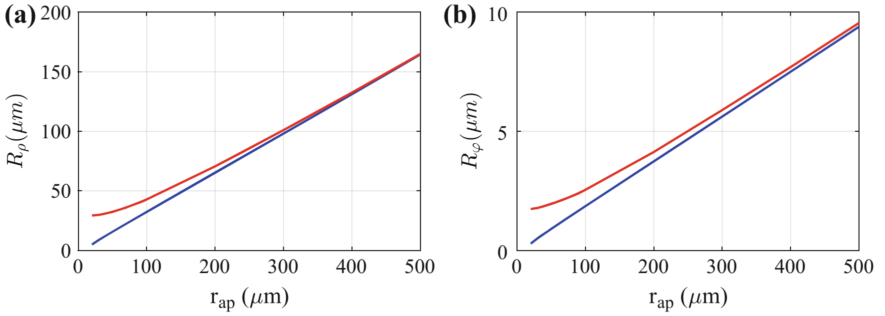

Fig. 4.19 Imaging resolutions as a function of the aperture size with emittance of zero (blue) and $\sqrt{E_k/(2m_ec^2)}$ (red). **a** Radial resolution; **b** Angular resolution

at AWA, the minimal aperture radius was 100 µm, B_f was fixed at 1500 Gauss, and high average selection phase near 80° was chosen. With these parameters, the average magnification, the radial resolution, the angular resolution, and the imaging range would be ∼5, <50 µm, <5 µm, ∼3 mm, respectively.

4.3 Experiment Preparation

4.3.1 New Cathode

From the dynamics simulation, high surface electric field benefits the high resolution field emission imaging system in terms of brightness, average magnification, and resolutions. A new shaped cathode with a small flat top and large rounding has been designed for the high power test, as shown in Fig. 4.20. Compared with the conventional flat cathode, the electric field at the cathode center is 10% higher, as illustrated in Fig. 4.21. Besides, the electric field of the cathode pipe edge is reduced by 5% which could help to reduce rf breakdown rate of the photocathode rf gun.

The new shaped cathode is made of oxygen-free copper with high precision single diamond tuning at the Accelerator Laboratory of Tsinghua University. During machining, off-axis tuning has been applied to remove the small protrusion at the cathode center [10]. The surface roughness has been measured to be ∼10 nm.

By using covering masks, 100 nm thick magnesium and gold layers have been sputtered onto the cathode prior to the high power test, as shown in Fig. 4.22. The four R0.3 mm magnesium spots are located at the x and y axis of the cathode. Their distance to the cathode center is 0.5, 1, 1.5, and 1.5 mm, respectively.

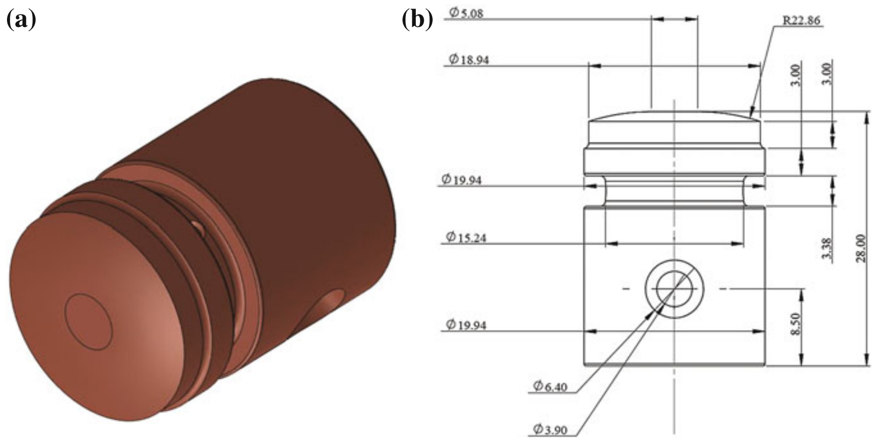

Fig. 4.20 New shaped flat cathode. **a** Three-dimensional model; **b** Two-dimensional drawing

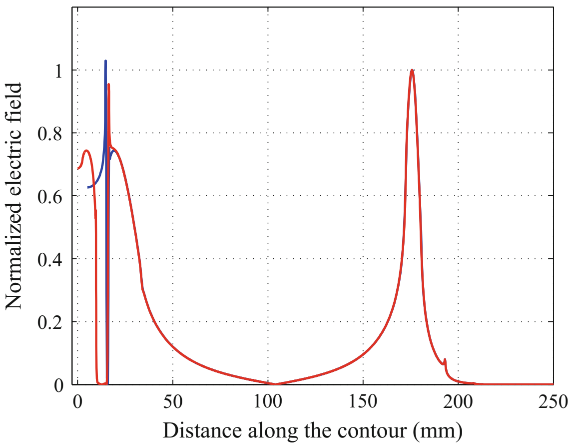

Fig. 4.21 The electric field distribution along the surface of the conventional flat cathode (blue) and the new shaped one (red) with the same input power and stored energy

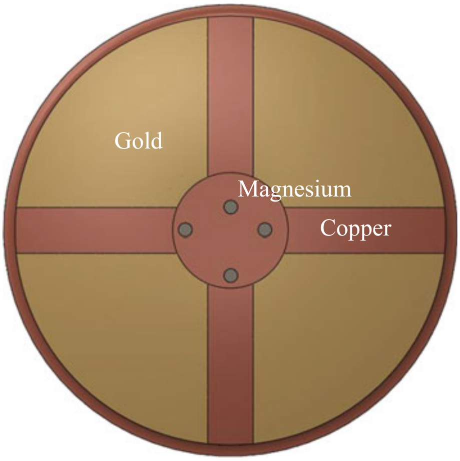

Fig. 4.22 Top view of the Copper cathode with Magnesium and Gold pattern

Due to its lower work function (3.7 eV) compared with copper, magnesium was expected to emit stronger current based on the F-N equation, as illustrated in Fig. 4.23. Therefore, the four spots could be viewed as references in the high power test which could help to determine the location of other emitters on the cathode. On the other hand, with a higher work function (5.0 eV), gold was supposed to suppress field emission from other areas on the cathode.

4.3.2 Beam Line Upgrading

The imaging system has been attached to the L-band high gradient photocathode rf gun test stand at AWA, as shown in Fig. 4.24.

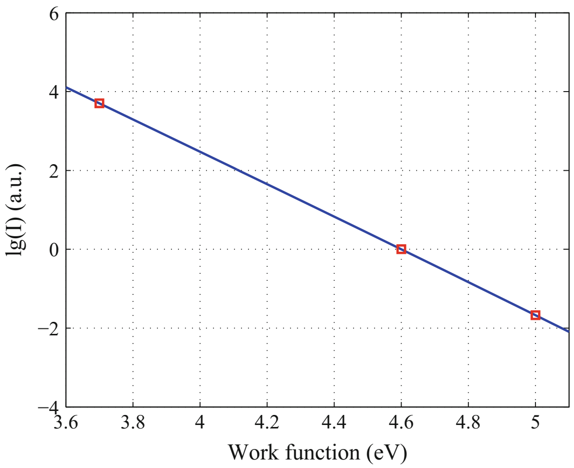

Fig. 4.23 Field emission current as a function of work function under 10 GV/m electric field on the surface. From left to right, the red squares denote magnesium, copper, and gold, respectively

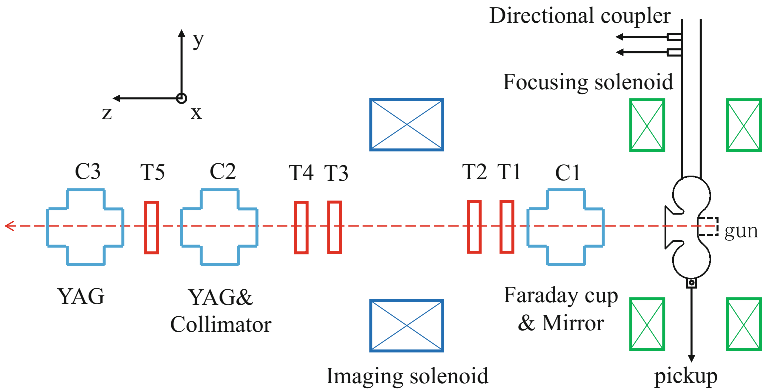

Fig. 4.24 Layout of the L-band high gradient photocathode rf gun test stand after integrated the high resolution field emission imaging system (T: trim magnet to align the beam)

Before the upgrade, the second cross was originally equipped with a YAG screen attached to an air actuator moving in the x-direction to approximately locate field emitters on the cathode. During the upgrade, a 1 mm thick stainless-steel plate attached to a motorized actuator moving in the y-direction has been added in the same cross to hold collimators, as shown in Fig. 4.25. Up to four collimators separated by a 30 mm interval could be installed on the plate. In the high power test, three laser-drilled tungsten collimators with 60 µm thickness and aperture radius of 100, 250, and 500 µm were applied. However, one of the R4 mm hole was deliberately left empty to roughly tune the beam.

Fig. 4.25 The stainless-steel plate with tungsten collimators. The R50 µm collimator was not installed in the high power test

Fig. 4.26 The YAG screen and attached mirror used in the imaging experiment

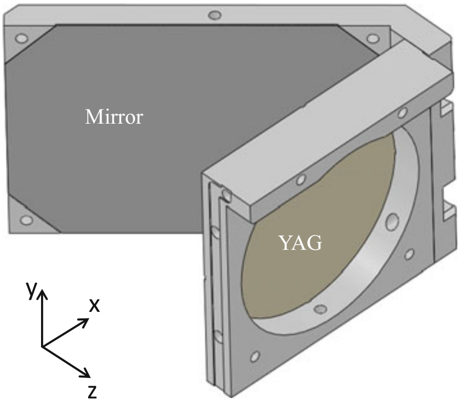

The design of YAG screen in the second and the third cross are shown in Fig. 4.26. The screens are placed at 45° to the beam line and a mirror is used to reflect the light from the screen to the outside-vacuum camera. The available diameter of the YAG screens is 44 mm. The brightness of the YAG screen is proportional to the deposited beam energy.

Several trim magnets (T1–T5) have been installed along the beam line, as illustrated in Fig. 4.24. T1 and T2 are used to guide the beam through the center of the imaging solenoid. T3 and T4 are used to guide the beam through the collimator. T5 is used to deliberately bend the beam to obtain larger imaging range.

In the L-band high gradient photocathode rf gun at AWA, the field emission current previous measured was at the order of milliampere which is significantly lower than the photoemission current. Besides, the simulated capture ratio of the imaging system is lower than 5% with the 100 µm aperture which may lead to undetectable brightness on the last YAG screen. To solve this problem, an intensified charge-coupled device camera (ICCD, modle PI-MAX from Princeton Instruments, 1024 × 1024 pixels [11]) was applied to observe the last YAG screen in the high

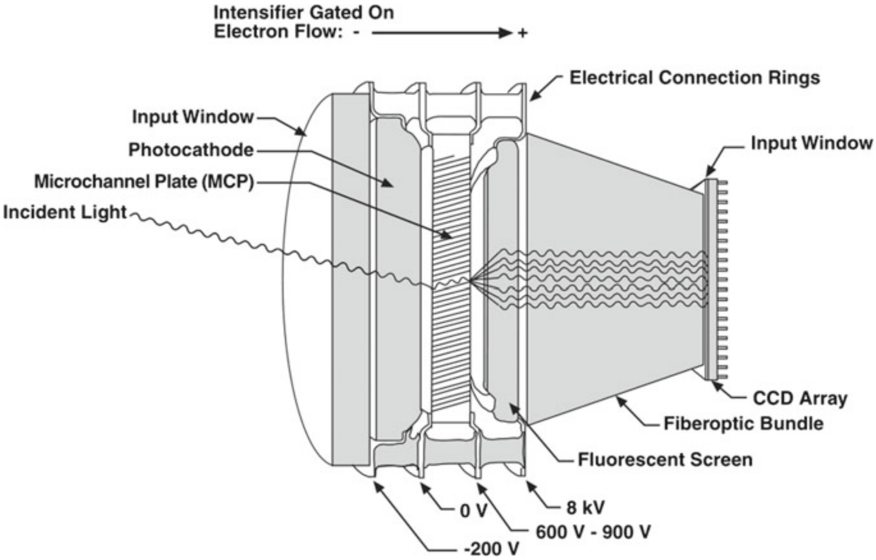

Fig. 4.27 The principle of the PI-MAX ICCD [11]

power test. The principle of the ICCD is illustrated in Fig. 4.27. The incident light first interacts with the cathode to generate photoemission electrons. Then the electron current is amplified by the microchannel plate and will illuminate the fluorescent screen downstream. The enhanced light signal is finally detected by the CCD array. This ICCD is capable of detecting single incident photon. In experiment, the exposure time was gated down to 2 μs to improve signal-to-noise ratio. The accumulation mode was also applied to further increase the brightness of field emission images.

4.4 High Resolution Field Emission Imaging Experiment

In the high power test, the new shaped cathode was rf conditioned to achieve high surface field prior to the high resolution field emission imaging experiment. In the rf conditioning period, the pulse length was 6.5 μs and the repetition rate was 5 Hz. The rf breakdown rate was manually controlled to be $10^{-4}\sim10^{-3}$/pulse. After $\sim$150000 pulses, the maximum input power achieved 2.5 MW and the corresponding electric field at the cathode center E_c reached 120 MW/m. During this period, by observing the accompanying flash, rf breakdowns have been detected to be located at the cathode as well as the cathode hole edge [12].

After rf conditioning, the input power was reduced to obtain E_c of 105 MV/m to prevent further rf breakdowns in the imaging experiment.

4.4.1 In-situ High Resolution Field Emitter Observation

Fig. 4.28 shows a typical field emission image on the last YAG screen without applying collimator. Features with long tails could be observed and emitters could not be distinguished from the low resolution image.

The Φ 8 mm collimator has been applied to roughly tune the beam. With different imaging solenoid strength, the field emission images are illustrated in Fig. 4.29. As expected by ASTRA simulation, higher average magnification was obtained by increasing the solenoid strength. The image of all emitters either moved towards or away from one single point when adjusting B_i. Therefore, this point, as pointed by the white arrow in Fig. 4.29a, is considered as the cathode center.

In Figs. 4.28 and 4.29, other than field emission electrons through the aperture, the brightness on the YAG screen can be affected by background luminance originating from X-rays generated by energetic electrons, secondary electrons, light reflection along the beamline, etc. To quantify background luminance, images were taken with a blank stainless steel plate. Then the background luminance was subtracted from the image taken with the aperture present, in order to ensure that brightness was only caused by the field emission current through the aperture. After background subtraction, the contrast and the ratio of signal to noise were remarkably improved, as shown in Fig. 4.30.

To achieve high resolution field emission imaging, smaller apertures were adopted in experiment with B_i fixed at 656 Gauss. Figure 4.31 shows the observed field emission pattern after background subtraction. The imaging quality improves with smaller apertures, which validates the high-resolution field emission imaging method in rf structures of selecting emitting phase and energy. Several strong and separated emission areas can be clearly seen with the Φ 200 μm aperture. In the following analysis, most of these strong emission areas can trace back to rf breakdown spots on the copper and gold surface. Strong field emission from the four magnesium spots

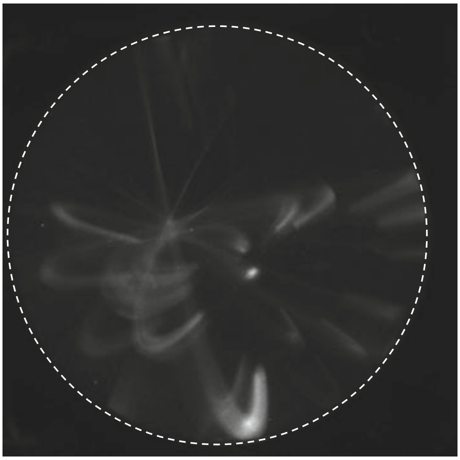

Fig. 4.28 Typical field emission image without collimator (accumulation of 20 frames). The white dashed circle indicates the boundary of the YAG screen which is 44 mm in diameter. The size of each pixel is 47 μm × 47 μm in this image

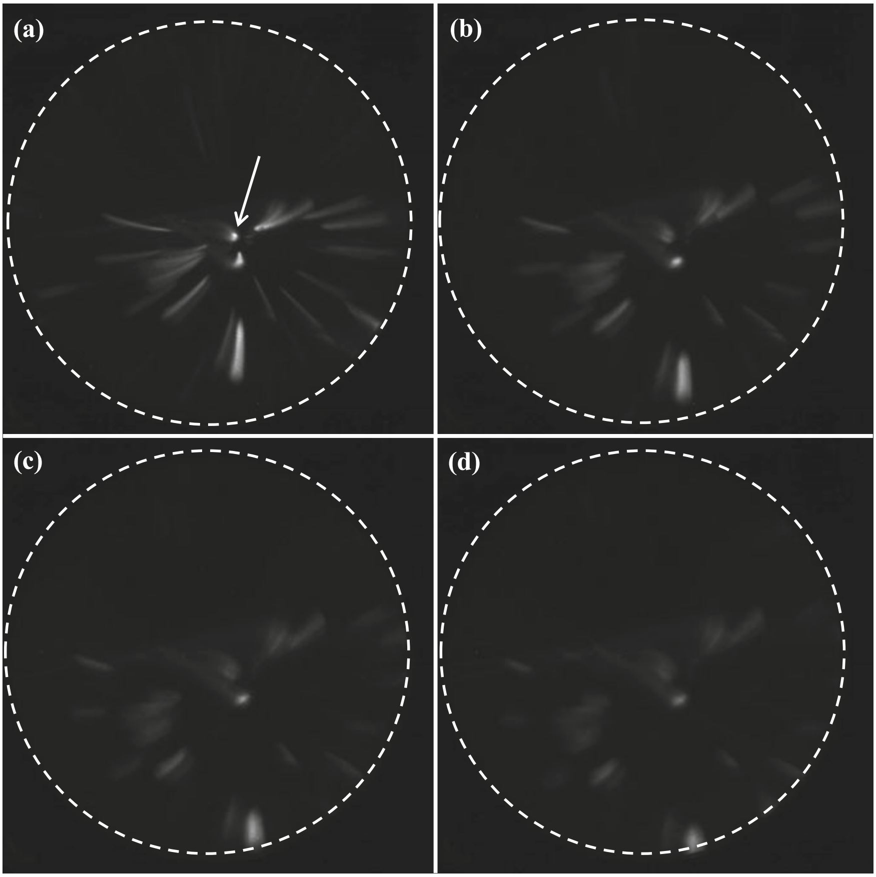

Fig. 4.29 Typical field emission images with the $\Phi 8\,\text{mm}$ collimator (accumulation of 20 frames). The white dashed circle indicates the boundary of the YAG screen. The white arrow in (a) points to an emitter at the cathode center. **a** $B_\text{i} = 656\text{Gauss}$; **b** $B_\text{i} = 708\text{Gauss}$; **c** $B_\text{i} = 734\text{Gauss}$; **d** $B_\text{i} = 751\text{Gauss}$

as shown in Fig. 4.22 was not observed. Oxidization of the magnesium layer during cathode installation which could raise its work function may be accountable [13].

The beam line parameters used to obtain Fig. 4.31 ($r_\text{ap} = 100\,\mu\text{m}$, $E_\text{c} = 105\,\text{MV/m}$, $B_\text{f} = 1500\,\text{Gauss}$, and $B_\text{i} = 656\,\text{Gauss}$) have been taken into the ASTRA simulation. Average selection phase, average magnification, average rotation, radial resolution, and angular resolution are simulated to be 88°, 5.0, 155°, $<60\,\mu\text{m}$, $<5\,\mu\text{m}$, respectively.

Within an emission area, tiny micro-structures (defined as emitters) that can not be distinguished by the system may exist and they contribute to the luminance. For simplicity, these emitters are assumed to be identical and located uniformly within an emission area whose size is $(d\rho,\ d\varphi)$. Electrons from each emitter follow the

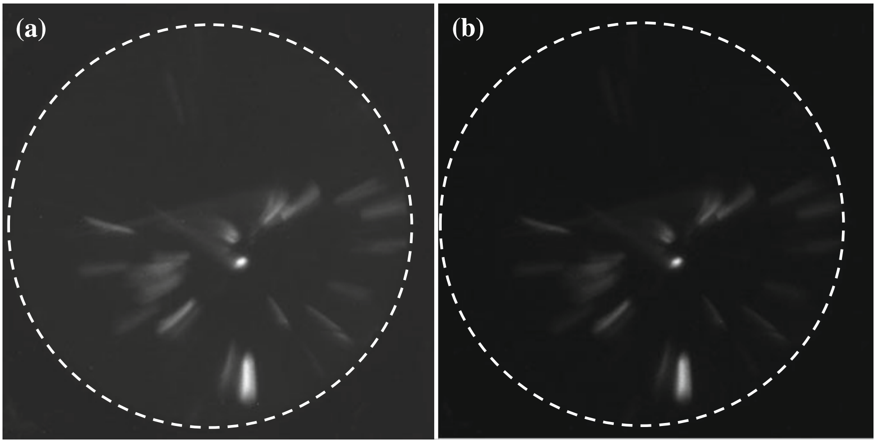

Fig. 4.30 The field emission images before (left) and after (right) background subtraction. The white dashed circle indicates the boundary of the YAG screen

Gaussian distribution of δ_ρ and δ_φ on the last YAG screen. Then the root-mean-square (rms) size of the bright spot on the imaging YAG screen can be calculated as

$$\begin{cases} \rho_{rms} = \sqrt{\delta_\rho^2 + \overline{mag}^2 d\rho^2/12} > \delta_\rho \\ \varphi_{rms} = \sqrt{\delta_\varphi^2 + d\varphi^2/12} > \delta_\varphi \end{cases} \tag{4.9}$$

Thus, taking the size of a small bright spot as marked in Fig. 4.22d, the upper limits of the axial and angular system resolution are calculated to be 147 and 107 µm, respectively. The results agree with the ASTRA simulation.

4.4.2 Field Enhancement Factor Measurement

The F-N equation is so far the most commonly used convention to quantitatively describe field emission, in which four determinants of the emission current are taken into account: the applied electric field strength, the emission area size A_e, the material work function ϕ, and the field enhancement factor β. In previous studies of rf structures, β is usually measured as an average value of a large surface [12, 14–16]. With the imaging system, β can be further measured in localized regions by quantifying their variation in luminous intensity with the rf field.

The brightness of the field emission image is proportional to the energy deposited on the YAG screen (luminance of the YAG screen has a linear response to the deposited energy). Assuming the portion of energy deposited is constant for electrons in this measurement, the luminance of the YAG screen is also proportional to

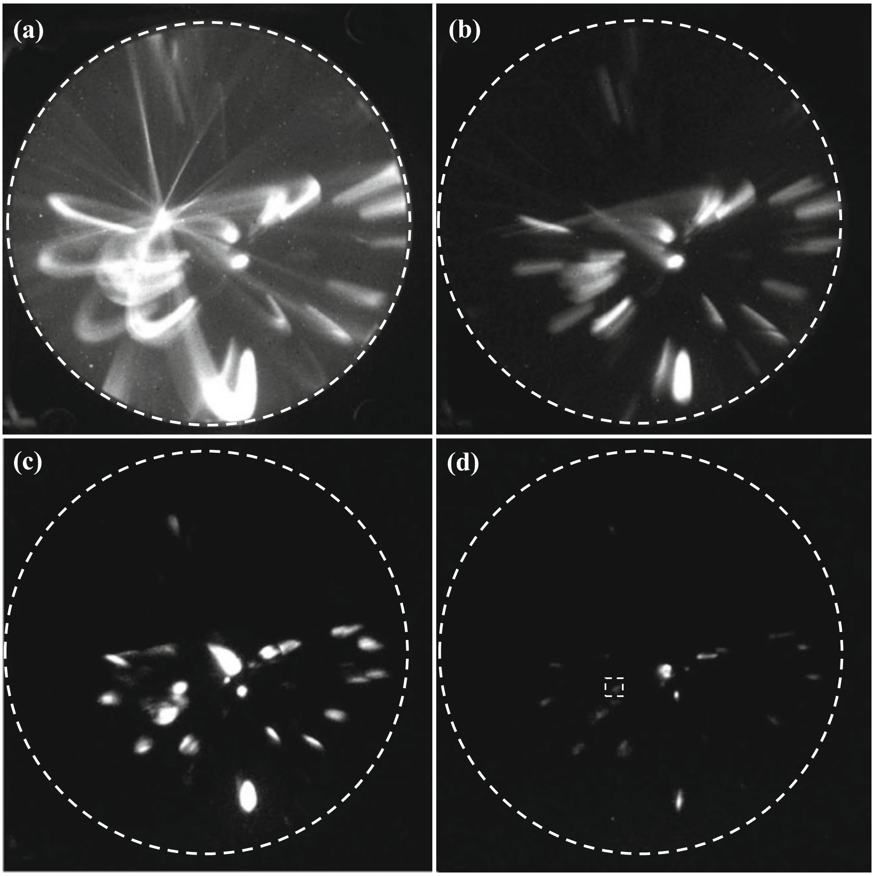

Fig. 4.31 Field emission images on the last YAG screen. The white dashed circle indicates the boundary of the YAG screen. The white dashed square in (**d**) indicates the emission area for the resolution calculation. **a** Without collimator. **b**–**d** With collimator. The aperture diameters are 8 mm, 1 mm, and 0.2 mm, respectively. **a**–**b** Accumulation of 20 frames. **c**–**d** Accumulation of 100 frames

the beam current. Therefore, the field enhancement factor β of selected areas can be obtained by fitting with the F-N equation along with other known parameters. During the measurement, E_c varied from 105 to 70 MV/m and the solenoid current was adjusted accordingly to maintain the same emitting positions on the last YAG screen, as illustrated in Fig. 4.32. In order to minimize the dependence of the capture ratio on $E_{\rm c}$, the biggest aperture (8 mm in diameter) was applied in this measurement. Although the resolutions are reduced to $\sim$1 mm, separated strong emission areas can still be distinguished. The background caused by other sources was measured and subtracted at each field level.

β for the entire imaged area is 76 which falls into the typical range in previous studies [14, 17]. Small regions which covers strong emission areas are chosen for

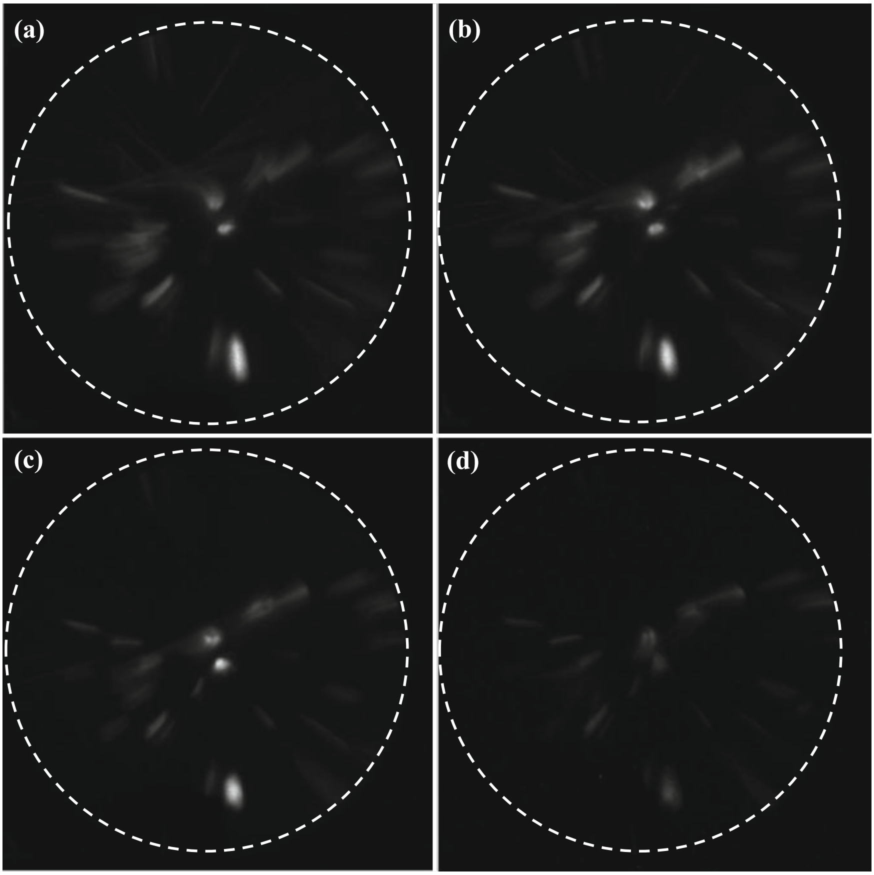

Fig. 4.32 Field emission images with different macroscopic electric field on cathode E_c (accumulation of 20 frames). The white dashed circle indicates the boundary of the YAG screen. **a** $E_c = 105\,\text{MV/m}$; **b** $E_c = 102\,\text{MV/m}$; **c** $E_c = 92\,\text{MV/m}$; **d** $E_c = 80\,\text{MV/m}$

localized β measurement. As a comparison, regions of the same size are also selected on the dark part inside and outside of the YAG screen (illustrated in Fig. 4.33a) to measure β in weak emission area and background, respectively. The measurement results are shown in Fig. 4.33b. The low value and non-linear dependence of data for the background confirms that the brightness from other sources has been subtracted correctly. β of the strong and weak emission areas is similar. In fact, β of other bright spots and dark areas as shown in Fig. 4.33a varies from 70 to 90 which is insignificant compared with the variation in brightness.

In order to achieve a quantitative explanation, a simple model for the strong and weak emission areas has been adopted as shown in Fig. 4.34.

In this model, a weak emission area is assumed to contain N weak emitters which have the same emission size $A_{e,0}$ and field enhancement factor β_0. According to the

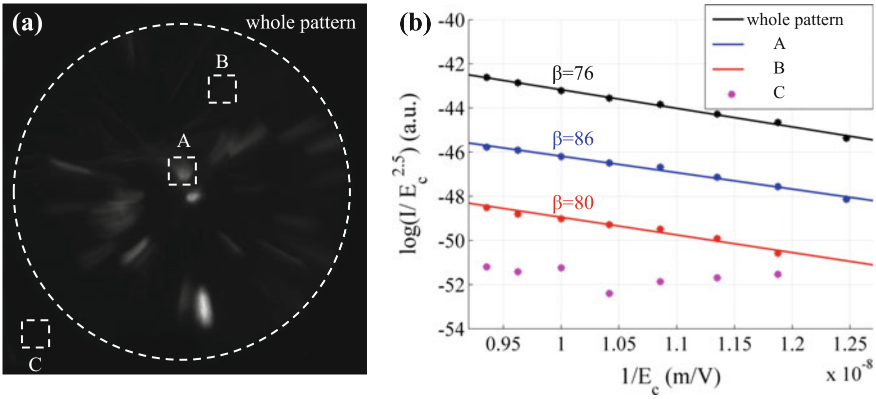

Fig. 4.33 Field enhancement factor measurement by the field emission imaging system. The white dashed circle indicates the boundary of the YAG screen. **a** Dark current image with the biggest aperture. White dashed squares (610 µm × 610 µm on the cathode) indicate selected regions for measurement as shown in (b). A: strong emission area, B: weak emission area, and C: background. A and B both locate on the copper surface by SEM examination. **b** Fowler-Nordheim plot. Spots and lines are the measured data and linear fitting, respectively

Fig. 4.34 A model for strong and weak emission areas on the cathode

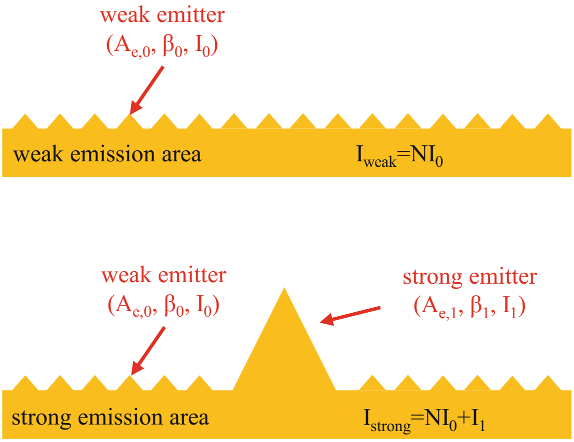

F-N equation (Eq. 1.12), the field emission current from a weak emitter and a weak emission area can be expressed as

$$\begin{cases} I_0 = CA_0(\beta_0 E_c)^{2.5}\exp(-\dfrac{D}{\beta_0 E_c}) \\ I_{weak} = NI_0 \end{cases} \tag{4.10}$$

where C and D are constants only depending on work function.

Fig. 4.35 α of the strong emitter (blue) and β_{strong} (red) as a function of β_1

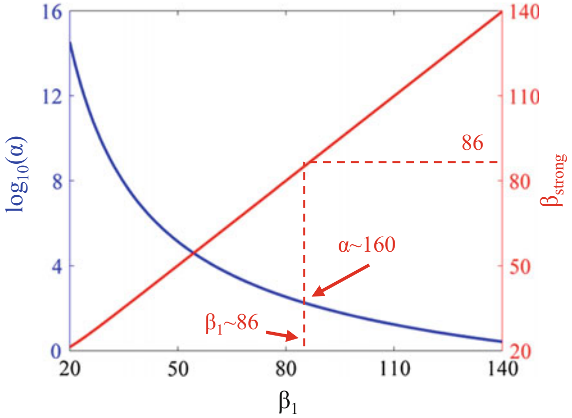

In a strong emission area, it's assumed to contain at least one strong emitter with $A_{e,1} = \alpha N A_{e,0}$ and β_1 in addition to N weak emitters. Therefore, the field emission current from a strong emitter and a strong emission area can be expressed as

$$\begin{cases} I_1 = C A_1 (\beta_1 E_c)^{2.5} \exp(-\dfrac{D}{\beta_1 E_c}) \\ I_{strong} = N I_0 + I_1 \end{cases} \tag{4.11}$$

By fitting the F-N equation, the field enhancement factor of the weak emission area β_{weak} equals to β_0. Meanwhile, the field enhancement factor of the strong emission area β_{strong} is weighted by β_0, β_1, and α. For the measured β_0 of 81 and I_{strong}/I_{weak} of $\sim$300, the dependence of α on β_1 is plotted as the blue line in Fig. 4.35. With each calculated (α, β_1) pair, β_{strong} is plotted as the red line in Fig. 4.35. As $I_{strong} \gg I_{weak}$, $I_1 \gg N I_0$ and β_{strong} is nearly equal to β_1. With β_{strong} measured to be 86, β_1 and α obtained from the plots in Fig. 4.35 are $\sim$86 and $\sim$160, respectively. The high α also indicates the remarkable difference in brightness between the weak and strong emission areas is caused by A_e when β is similar and ϕ is the same.

4.4.3 Surface Analysis

After the imaging experiment, the cathode was examined by SEM and WLI as illustrated in Fig. 4.36a–e. The major part of the surface remains intact and the roughness is 10$\sim$20 nm. $\sim$40 breakdown spots have been observed within the maximum imaging area, as marked by the red circles in Fig. 4.36a. Micro-structures such as melting craters and droplets are clearly indications of breakdown spots, which are likely to cause large A_e. To study the relationship between the strong emission areas and the breakdown spots, the field emission image obtained with the smallest aperture has

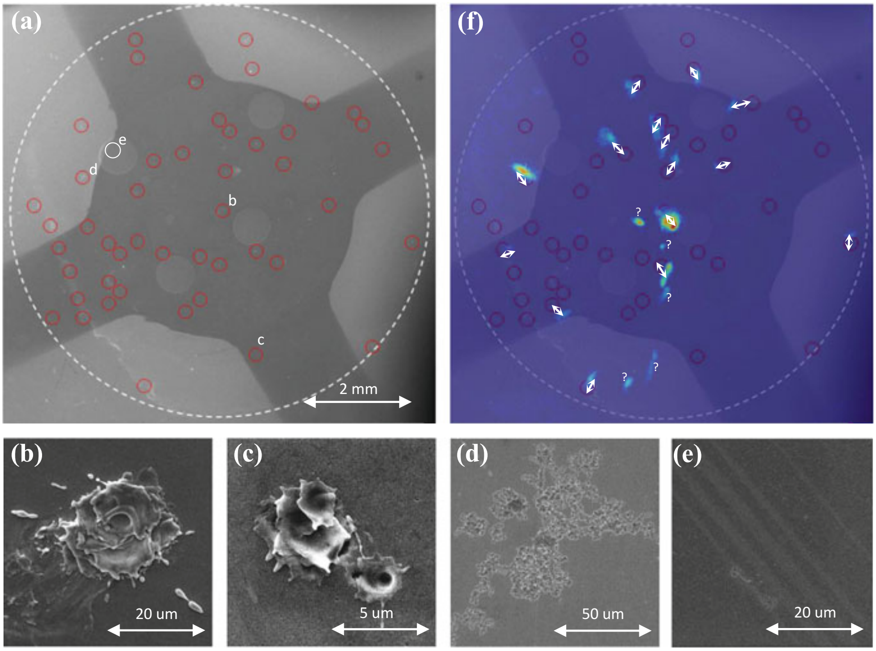

Fig. 4.36 Overlap of field current emission areas and breakdown spots. **a** Overview of breakdown spots on the cathode. The red circles indicate the areas which contain breakdown spots. The white dash circle indicates the maximum visible range by the in-situ field emission imaging system.break **b**–**e** Zoom-in view of circles marked in (**a**). **b**, **c** Breakdown spot on Cu which overlaps and does not overlap with a strong field emission area, respectively. **d** Breakdown spot on Au which overlaps with a strong field emission area. **e** Smooth undamaged surface on Mg. **f** Overlap of the strong field emission areas and the breakdown spots. The field emission imaging is in false color for better display. The overlapped strong emission areas and breakdown spots are marked by arrows. The strong emission areas with unknown origin are marked by the question mark

been resized and rotated based on the average magnification and rotation in dynamics simulation. The results show that ∼75% of the strong emission areas overlap with the breakdown spots, as illustrated in Fig. 4.36f. The origin of the remaining ∼25% strong emission areas remains unknown, which may be attributed to microscopic surface features such as grain boundaries or defects that have not been detected by the examination tools used. The results also reveal that half of the breakdown spots do not emit current at a level high enough to be detected by the imaging system.

In previous study, a significant increase of dark current has been observed after rf breakdowns which implies that strong field emission may result from rf breakdowns in high gradient rf cavities [12]. The overlap of strong field emission areas and breakdown spots supports this conventional understanding. Field emission is generally considered to be a trigger of rf breakdown. However, the observation that no further breakdowns occurred at the strong field emission areas in the imaging system indicates that a steady field emission alone may not be sufficient to trigger an rf breakdown.

4.5 Summary

In summary, an in-situ high-resolution field emission imaging method has been proposed by using solenoids and collimator to select electrons emitted from certain rf phase. The imaging properties have been systemically studied with the ASTRA simulation. Accordingly, the L-band high gradient photocathode rf gun test stand has been upgraded and the imaging setup has been installed.

In high power test, separated strong emission areas have been observed with ∼100 μm resolution. The localized field enhancement factor has been measured. The results have been analyzed with a new model of emitter distribution which indicates that strong field emission observed in the experiment is a result of large emission area rather than high field enhancement factor. Post surface analysis by SEM and WLI reveals that ∼75% of the strong field emission areas overlap with rf breakdown spots. This work greatly expands the understanding of field emission which will in turn facilitate research into electron sources, particle accelerators, and high gradient rf devices in general.

The study of high resolution field emission imaging has been published in Phys Rev Lett 117, 084801 (2016) [18].

References

1. Noer R, Niedermann P, Sankarraman N et al (1986) Electron field emission from intentionally introduced particles on extended niobium surfaces. J Appl Phys 59:3851–3860
2. Lysenkov D, Müller G (2005) Field emission measurement techniques for the optimisation of carbon nanotube cathodes. Int J Nanotechnol 2:3
3. Pandey A, Müller G, Reschke D et al (2009) Field emission from crystalline niobium. Phys Rev ST Accel Beams 12:023501
4. Han J, Bähr J, Grabosch H et al (2005) Dark current and multipacting in the photocathode rf guns at PITZ. In: Proceedings of PAC2005. Knoxville, USA
5. Dowell D, Jongewaard E, Limborg C et al (2007) Measurement and analysis of field emission electrons in the LCLS gun. In: Proceedings of PAC2007. Albuquerque, USA
6. Xiang R, Arnold A, Kamps T et al (2014) Experimental studies of dark current in a superconducting rf photoinjector. Phys Rev ST Accel Beams 17:043401
7. Fursey G (2008) Theory and design of charged particle beams. WILEY-VCH Verlag GmbH Co, KGaA, Weinheim
8. Ganter R, Bakker R, Gough C et al (2006) Nanosecond field emitted and photo-field emitted current pulses from ZrC tips. Nucl Instrum Methods Phys Res Sect A 565:423–429
9. Dowell D, Schmerge J (2009) Quantum efficiency and thermal emittance of metal photocathodes. Phys Rev ST Accel Beams 12:074201
10. Qian H (2012) Research on the emittance issues of photocathode RF Gun. Ph.D. thesis, Tsinghua University

11. Princeton Instruments (2004) PI-MAX/PI-MAX2 System
12. Wang JW, Loew GA (1997) Field emission and rf breakdown in high-gradient room-temperature linac structures. Technical report SLAC-PUB-7684, SLAC
13. Lim J, Oh J, Ko B et al (2003) Work function of MgO single crystals from ion-induced secondary electron emission coefficient. J Appl Phys 94:764
14. Chen H, Du Y, Gai W et al (2012) Surface-emission studies in a high-field rf gun based on measurements of field emission and Schottky-enabled photoemission. Phys Rev Lett 109:204802
15. Baryshev S, Antipov S, Shao J et al (2014) Planar ultrananocrystalline diamond field emitter in accelerator radio frequency electron injector: Performance metrics. Appl Phys Lett 105:203505
16. Shao J, Antipov S, Baryshev S et al (2015) Observation of field-emission dependence on stored energy. Phys Rev Lett 115:264802
17. Grudiev A, Calatroni S, Wuensch W (2009) New local field quantity describing the high gradient limit of accelerating structures. Phys Rev ST Accel Beams 12:102001
18. Shao J, Shi J, Antipov S et al (2016) In situ observation of dark current emission in a high gradient rf photocathode gun. Phys Rev Lett 117:084801

Chapter 5
Summary and Future Study

The accelerating gradient is an key parameter to evaluate the performance of an rf linear accelerating structure. High gradient accelerating structures are highly desired in board applications from high energy machines such as TeV electron-positron collider and compact X-ray FEL, to medium energy facilities for scientific R&D, and to low energy accelerators for industrial and medical purposes. For instance, the gradient of the CLIC project is aimed to reach 100 MV/m, nearly threefold higher than that obtained with state-of-art technology. Its realization is mainly limited by rf breakdown which is generally considered to be triggered by field emission from surface exposed to high electric field.

Although intensive researches have been performed to study rf breakdown and to minimize the rf breakdown rate in high gradient accelerating structures for decades, there is not a single theory well-established to match all dependence observed in experiment and to precisely predict the structure limitation. In practice, the highest achievable accelerating gradient in X-band multi-cell structures is limited to $\sim$120 MV/m for prototypes with extensive effort. The difficulty lies in the extreme complexity of rf breakdown, and the fact that many physical parameters, such as the electric field, the pulse heating, and the modified Poynting vector, are usually coupled with each other in conventional rf structures.

Apart from the conventional statistical method which requires hundreds of thousands of hours in high power tests, more controllable means are necessary to be developed to understand the physics of the rf breakdown phenomenon. Driven by this requirement, the thesis has proposed and applied several novel methods, including controlling the location with high intensity laser and pin-shaped cathode, and locating field emitters with in-situ high resolution imaging.

The rf breakdown study with high intensity laser has been performed in an S-band 1.6 cell photocathode rf gun at the Accelerator Laboratory of Tsinghua University. It is demonstrated that rf breakdown in the photocathode rf gun can be triggered by an intense laser pulse at predictable locations and moments. The time evolution of electron emission at the nanosecond scale after the onset of breakdown has been observed and analyzed. Comparison between rf breakdowns with and without laser

J. Shao, *Investigations on rf Breakdown Phenomenon in High Gradient Accelerating Structures*, Springer Theses, https://doi.org/10.1007/978-981-10-7926-9_5

triggering indicates that the laser trigger can serve as a more controllable and flexible method in breakdown study. The experiment together with the equivalent circuit model analysis reveal that multiple-breakdown can be triggered by the power flow between cells after the initial EEE, which implies standing-wave structures with separated cells may be more favorable for high gradient accelerators.

The field emission and rf breakdown study with pin cathode has been performed with an L-band high gradient single cell photocathode rf gun at AWA. During rf conditioning, the maximum electric field on the tip has reached 700 MV/m, which is a new record in normal-conducting structures with microsecond pulse length. Field emission parameters, including the field enhancement factor β and effective emission area A_e, have been measured during the rf conditioning process. Their evolution confirms a continuous change of the surface during the rf conditioning period. The nearly constant maximum surface field $\beta \cdot E_{\text{tip}}$ supports the hypothesis of breakdown threshold on copper surface. A comparison of the emission area between the SEM observation and the F-N equation fitting also suggests field emission current is not uniformly emitted from potential spots with high aspect ratio. In addition, a strong correlation between the field emission current and the stored energy has been observed on pin cathodes. This study has excluded mechanisms that may affect the conclusion, such as multipacting in the cavity, background emission from other surfaces, secondary electron emission from the Faraday cup, the beam loading effect, and the space charge limited emission effect. The dependence is fundamental while inconsistent with the F-N equation, which indicates that global parameters like stored energy affects the localized field emission phenomenon. The findings suggest a new territory to be explored while developing field emission electron sources and high gradient rf structures.

With the same test stand at AWA, an in-situ high-resolution field emission imaging method has been developed by using solenoids and collimator to select electrons emitted from certain rf phase. The imaging properties have been systemically studied with ASTRA dynamics simulation and the beam line parameters have been optimized. In high power test, separated strong emission areas have been observed with $\sim$100 μm resolution. The localized field enhancement factor has been measured. The results have been analyzed with a new model of emitter distribution and indicate that strong field emission observed in the experiment is a result of large emission area rather than high field enhancement factor. Post surface analysis by SEM and WLI reveals that $\sim$75% of the strong field emission areas overlap with the rf breakdown spots. This work greatly expands the understanding of field emission which will in turn benefit research into electron sources, particle accelerators, and high gradient rf devices in general.

Based on the current research, more studies are to be conducted in the future.

1. Continue the laser-triggered rf breakdown study inside photocathode rf guns by guiding incident laser to high magnetic field and high power flow region. This study will decouple the effect of various physical parameters on rf breakdown and study them in a more controllable manner.

2. Design multi-cell standing-wave structure with separate feeding and zero coupling. Demonstrate its high gradient performance in high power test.
3. Perform theoretical and simulation research on the field emission dependence on stored energy in the L-band single-cell gun. Accordingly, optimize accelerating structure to suppress field emission.
4. Design pin cathode with even higher geometry field enhancement factor to observe the evolution of field emission parameters in a wider range.
5. Observe the field emission evolution during rf conditioning with the in-situ high resolution field emission imaging system to understand the nature of rf conditioning and propose new methods to expedite the procedure.
6. Improve resolutions of the field emission imaging system to a micrometer scale by applying smaller apertures. Test cathodes with different surface conditions and analyze the origin of emitters systemically in order to develop new method to eliminate strong field emitters on the surface.

Appendix A
Calculating the Electric Field on the Pin Cathode

The precise amplitude of electric field on the pin cathode is critical in the study of field emission dependence on stored energy. Due to the weak coupling of the rf pickup installed on the rf gun, direct electric field measurement is difficult. Therefore, an equivalent circuit model has been developed to indirectly calculate the electric field on the pin cathode from the input power.

Similar to the method introduced in Chap. 2, the single-cell photocathode rf gun can be viewed as a parallel RLC circuit coupled to the power source (represented by a current source and a resistor), as shown in Fig. A.1.

The equation of the circuit can be expressed as

$$\frac{d^2V}{\omega_0^2 dt^2} + \frac{1}{\omega_0 Q_0}\frac{dV_0}{dt} + V_1 = \frac{R/Q_0}{\omega_0}\frac{d}{dt}\left(I_g - \frac{V_0}{R_g}\right) \tag{A.1}$$

where V denotes the gun voltage, ω_0 and Q_0 denote the frequency and the unloaded quality factor of the cell, respectively.

To solve Eq. A.1 numerically, V and I_g are further expressed in the complex format as

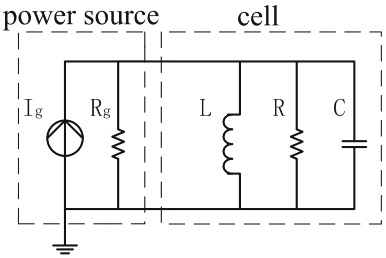

Fig. A.1 Equivalent circuit model of the L-band single-cell photocathode rf gun

J. Shao, *Investigations on rf Breakdown Phenomenon in High Gradient Accelerating Structures*, Springer Theses, https://doi.org/10.1007/978-981-10-7926-9

$$
\begin{cases}
V = (V_r + jV_i)e^{j\omega t} & \text{(A.2)} \\
I_g = (I_{g,r} + jI_{g,i})e^{j\omega t} & \text{(A.3)}
\end{cases}
$$

where ω denotes the operation frequency.

Therefore, the differential equation set to be solved for the L-band single-cell photocathode rf gun is

$$
\begin{cases}
\dot{V}_r = \frac{\omega_0^2}{2\omega}[-(\frac{\omega}{\omega_0 Q_0} + \frac{(R/Q_0)\omega}{\omega_0 R_g})V_r + (\frac{\omega^2}{\omega_0^2} - 1)V_i \\
\qquad -(\frac{1}{\omega_0 Q_0} + \frac{(R/Q_0)}{\omega_0 R_g})\dot{V}_i + \frac{(R/Q_0)}{\omega_0}(\dot{I}_{g,i} + \omega I_{g,r})] \\
\dot{V}_i = -\frac{\omega_0^2}{2\omega}[(\frac{\omega^2}{\omega_0^2} - 1)V_r + (\frac{\omega}{\omega_0 Q_0} + \frac{(R/Q_0)\omega}{\omega_0 R_g})V_i \\
\qquad -(\frac{1}{\omega_0 Q_0} + \frac{(R/Q_0)}{\omega_0 R_g})\dot{V}_r + \frac{(R/Q_0)}{\omega_0}(\dot{I}_{g,r} - \omega I_{g,i})]
\end{cases}
\tag{A.4}
$$

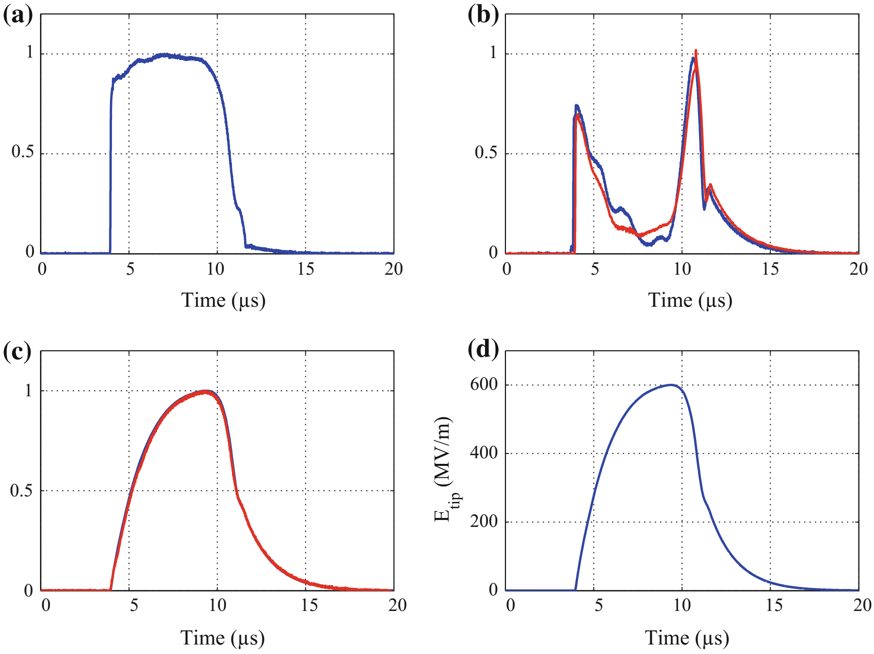

Fig. A.2 Calculation of the electric field on the tip with the equivalent circuit model. **a** Normalized input wave in the experiment; **b** Normalized reflected wave; **c** Normalized gun voltage; **d** Calculated electric field on the tip. In **b**, **c**, the blue and the red line indicate the experiment and the simulation results, respectively

The method to calculate parameters in the equation is the same as introduced in Chap. 2. Cell frequency ω_0 is the only adjustable parameter in the model, which might be detuned up to 20 kHz due to the temperature control accuracy of the rf gun chiller.

With the recorded signal of the input rf power shown in Fig. A.2(a), ω_0 has been adjusted in the model to best match the reflection in the experiment, as illustrated in Fig. A.2(b). With such ω_0 setting, the simulated rf pickup signal is in perfect accordance with the experiment result, as illustrated in Fig. A.2(c), which validates the accuracy of the equivalent circuit model and its parameters.

The ratio of the electric field on the tip and the gun voltage has been simulated by two-dimensional code Superfish and three-dimensional code Omega3P. Accordingly, the electric field on the tip during experiment can be precisely calculated, as illustrated in Fig. A.2(d).